2014

Parity-time and supersymmetry in optics

Mohammad Ali Miri
University of Central Florida

PARITY-TIME AND SUPERSYMMETRY IN OPTICS

by

MOHAMMAD-ALI MIRI

B.S. Shiraz University, 2008
M.S. Sharif University of Technology, 2010
M.S. University of Central Florida, 2013
M.S. University of Central Florida, 2014

A dissertation submitted in partial fulfillment of the requirements
for the degree of Doctor of Philosophy
in CREOL/The College of Optics & Photonics
at the University of Central Florida
Orlando, Florida

Fall Term
2014

Major Professor: Demetrios N. Christodoulides

ABSTRACT

Symmetry plays a crucial role in exploring the laws of nature. By exploiting some of the underlying analogies between the mathematical formalism of quantum mechanics and that of electrodynamics, in this dissertation we show that optics can provide a fertile ground for studying, observing, and utilizing some of the peculiar symmetries that are currently out of reach in other areas of physics. In particular, in this work, we investigate two important classes of symmetries, parity-time symmetry (PT) and supersymmetry (SUSY), within the context of classical optics.

The presence of PT symmetry can lead to entirely real spectra in non-Hermitian systems. In optics, PT-symmetric structures involving balanced regions of gain and loss exhibit intriguing properties which are otherwise unattainable in traditional Hermitian systems. We show that selective PT symmetry breaking offers a new method for achieving single mode operation in laser cavities. Other interesting phenomena also arise in connection with PT periodic structures. Along these lines, we introduce a new class of optical lattices, the so called mesh lattices. Such arrays provide an ideal platform for observing a range of PT-related phenomena. We show that defect sates and solitons exist in such periodic environments exhibiting unusual behavior. We also investigate the scattering properties of PT-symmetric particles and we show that such structures can deflect light in a controllable manner.

In the second part of this dissertation, we introduce the concept of supersymmetric optics. In this regard, we show that any optical structure can be paired with a superpartner

with similar guided wave and scattering properties. As a result, the guided mode spectra of these optical waveguide systems can be judiciously engineered so as to realize new families of mode filters and mode division multiplexers and demultiplexers. We also present the first experimental demonstration of light dynamics in SUSY ladders of photonic lattices. In addition a new type of transformation optics based on supersymmetry is also explored. Finally, using the SUSY formalism in non-Hermitian settings, we identify more general families of complex optical potentials with real spectra.

To Armaghan

ACKNOWLEDGMENTS

I would like to thank my advisor, Professor Demetrios Christodoulides, for everything he taught me. It has been an honor for me to work under his direct supervision for these fruitful years since he is one of the greatest scientists in the field. Working with Professor Christodoulides has not only advanced me academically but has also taught me how to be a better person. In this regard, I believe that the professor-advisor relation in our group has been completely different than other research groups, and instead I felt like I was a family member. I would also like to mention that Professor Christodoulides greatly supported me when I had to leave this country for family reasons, which meant everything to me. I would like to express my utmost gratitude for everything he has done for me.

There is no doubt that any scientific achievement is made possible only through courteous collaboration between individuals. In this regard, I would like to thank Professors Peschel, Khajavikhan, LiKamWa, Xiao and their group members Alois and Martin with whom I had the chance to have a respectful and productive collaboration. I would also like to thank friends and team members Matt, Armando, Matthias, Nick, Amin and Absar who have helped creating a nice and friendly environment in our research group.

At the end, I would also like to thank my wife and my parents for being patient and supportive during this period of my life.

TABLE OF CONTENTS

LIST OF FIGURES

LIST OF TABLES

CHAPTER ONE: INTRODUCTION

Within the last two decades, the design of artificial materials with desired optical properties and functionalities has been one of the major fields of research in optics. In this regard, by engineering constitutive parameters of materials, photonic crystals and optical metamaterials have been proposed [1-4]. Due to the high degree of fabrication complexities, however, the practicability of such structures is still a matter of debate. Of interest would be to develop new type of synthetic materials as well as new design techniques to achieve a desired functionality in optical devices.

In this work we study a new class of artificial optical materials which incorporate gain and loss. Such non-Hermitian optical structures has recently attracted a considerable amount of attention due to the recently developed notions of PT-symmetric optics. We investigate such symmetry in both discrete and continuous optical arrangements.

In addition we utilize supersymmetry (SUSY) as a strong mathematical tool for engineering guided wave and scattering properties of dielectric structures. We show that for any one-dimensional optical structure, a superpartner can obtained that share the exact same eigenvalue spectra. Also, each one-dimensional optical structure belongs to a one parameter family of structures which again share the exact same bound sate and scattering properties. Such structures can be obtained via SUSY transformations which are originally inspired from quantum mechanics.

This dissertation is divided in two major parts. In the first part, including Chapters 2-6, we investigate PT-symmetric optical systems. In the second part, which includes Chapters 7-9, we introduce the concept of supersymmetry in the context of optics. Finally in Chapter 10 we draw a line between these two different symmetries and explore the mathematical formalism of supersymmetry in the context of non-Hermitian PT-symmetric optical structures.

In Chapter 2 we review the basic concepts of PT symmetry. We first present the mathematical formalism and show how the presence of such symmetry leads to real-valued eigenvalues. PT-symmetry-breaking and other related phenomena are then explained through the PT-symmetric coupler which is one of the simplest examples of PT systems. Afterwards we find the necessary conditions of PT symmetry for various scenarios of optical structures. This ranges from the low contrast structures that can be explained through scalar paraxial wave approximation to general materials that need to be analyzed through full-wave Maxwell's equations.

Chapter 3 is devoted to PT-symmetric lasers. In general in multimode PT system, different modes exhibit different critical point for symmetry breaking. We show that this same principle can be utilized to achieve single mode lasing in PT lasers. We first demonstrate this effect through examples of single transverse mode lasing in semiconductor and fiber laser amplifiers. Afterwards we show that this approach can be applied to micro-ring resonator laser systems to filter either transverse or longitudinal modes. The experimental results of single mode lasing in micro-ring resonator laser systems are also presented in this chapter.

In the 4th the scattering properties of PT-symmetric structures are investigated. In this chapter, first by considering the symmetries of the governing equations, we restate the optical theorem and the reciprocity theorem for PT-symmetric objects. In addition, a general formalism for treating two-dimensional scattering problems in complex dielectric settings is also presented. In particular, we calculate the scattering pattern of a PT dielectric cylinder, where half of the cylinder involves gain and the other half the same amount of loss. We show that such structure can deflect light through a certain angle that depends on the gain/loss contrast.

In Chapter 5 we investigate PT symmetry in a new class of optical lattices, the so called mesh lattices. Mesh lattices were first proposed as a new platform for observing a range of PT-related phenomena in a periodic environment. Such lattices while offering flexibility in the real and imaginary parts of their associated potentials are designed cleverly to bypass undesired mismatches typically caused by Kramers-Kronig relations. In this chapter we first analyze both Hemitian and PT-symmetric versions of mesh lattices through their corresponding band structure and Bloch wave solutions. Afterwards the unconventional properties of defect states in such lattices are explored. We show that mesh lattices, in the nonlinear regime can also support soliton solutions. At the end experimental results of time domain mesh lattices are also presented.

Chapter 6 of this dissertation targets integrability in two nonlinear PT systems. The first system is a PT-symmetric grating, in the presence of Kerr nonlinearity. We show that stable Bragg soliton solutions can be found for such structures. In addition we consider a

Schrödinger-like equation with PT-symmetric nonlinearity and we show such system is fully integrible.

In Chapter 7 we introduce the basics of supersymmetry in the context of optics. We first present the general mathematical formalism of supersymmetry and show that two superpartner operators can share the exact same eigenvalue spectra while the only exception can be the eigenvalue associated with the fundamental state depending on whether supersymmetry is in unbroken or broken regime. This idea is then applied to one-dimensional optical structures in the paraxial and non-paraxial regimes. In addition we show that by starting from a given optical potentials one can construct a one-parameter family of iso-spectral potentials. Such potentials all share the exact same eigenvalue spectra.

It is then shown in Chapter 8 that SUSY formalism can be applied to a wide range of optical waveguides. In this manner a superpartner can be obtained for a given optical waveguide with an arbitrary refractive index profile. We show that SUSY formalism becomes much simpler in the framework of the tight-binding approximation where the differential operators are replaced with matrix operators. This approach is then applied to establish SUSY partnership in photonic lattices. The results of the first experimental demonstration of supersymmetric behavior in such photonic lattices are then presented. In this chapter, we also show that the formalism of supersymmetry can be applied to optical fibers with circularly symmetric cross sections. Finally we show how these ideas can be used for mode filtering, and mode multiplexing applications.

In Chapter 9 we investigate scattering properties of supersymmetric structures. We show that two superpartner scatterers can have similar reflection and transmission coefficients for all angles of incidence. In fact, while the intensities of the reflected and transmitted waves are the same, the corresponding phases are in general different and this depends also on whether supersymmetry is in unbroken or broken regime. On the other hand for all members of iso-spectral potentials the scattering coefficients are exactly the same in both intensity and phase. Based on these three different scenarios we introduce a new class of transformation optics in one-dimensional settings and propose possible applications.

In Chapter 10, SUSY transformations are applied to non-Hermitian systems. While for a real potential the unbroken superpartner is generally obtained by removing the ground state's eigenvalue, we show that any arbitrary higher order state can be removed from the spectrum of a PT-symmetric potential. Interestingly the parametric family of potentials which are all iso-spectral with a given PT potential no longer preserve the PT symmetry. In addition we show that a more general class of non-Hermitian and non-PT-symmetric Hamiltonians can exhibit entirely real spectra. This is because such Hamiltonians exhibit a Hermitian superpartner.

Finally in Chapter 11 we summarize our results and present an outlook for future works.

1.1. Assumptions and conventions

In this dissertation, we use the terminology of optical potential or potential for the spatial dependent permittivity or refractive index distribution. This term is used in analogy with the quantum mechanical potential function as appearing in Schrödinger equation. When treating time harmonic fields, in this entire work, we use $\exp(-i\omega t)$ as the convention of time dependency.

1.2. References

1. J. D. Joannopoulos, P. R. Villeneuve and S. Fan, "Photonic crystals: putting a new twist on light," Nature (London) **386**, 143 (1997).

2. J. C. Knight, J. Broeng, T. A. Birks, P. St. T Russell, "Photonic band gap guidance in optical fibers," Science **282**, 1476 (1998).

3. W. L. Barnes, A. Dereux, and T. W. Ebbesen, "Surface plasmon subwavelength optics," Nature (London) **424**, 824 (2003).

4. D. R. Smith, J. B. Pendry, and M. C. K. Wiltshire, "Metamaterials and negative refractive index," Science, **305**, 788 (2004).

CHAPTER TWO: PT SYMMETRY IN OPTICS

It took more than seventy years to realize that Hermiticity of quantum Hamiltonians depends on the choice of the inner product in the physical Hilbert space of states. This latter was first pointed out by Bender and Boettcher [1]. They showed that a wide class of Hamiltonians that respect PT symmetry can exhibit entirely real spectra. Since then PT symmetry has been a subject of intense interest in the field of quantum mechanics [1-15]. Later it was shown by Mostafazadeh that PT-symmetric Hamiltonians are only specific class of the general families of pseudo-Hermitian operators [9-12]. We will further discuss this concept in the Chapter 10 of this dissertation where we investigate supersymmetry in non-Hermitian operators.

Unfortunately however, quantum mechanics is by nature a Hermitian theory and thus any evidence of PT symmetry in such systems has remained out of reach. On the other hand, due to the presence of gain and loss, optics provides a fertile ground for observation of PT symmetry. Based on this fact, in 2008, it was suggested that notions from PT symmetry can be directly introduced in the optical domain [16-18]. Afterwards it was shown in several studies that PT-symmetric structures can exhibit unusual properties that does not have a counterpart in traditional Hermitian structures what so ever [19-29].

In this chapter we first review the mathematical formalism of PT-symmetric Hamiltonians. We show how the presence of PT symmetry leads to real-valued eigenvalues. Then we show how this concept can be utilized in the context of optics. First we discuss a

PT symmetric coupler that is perhaps the simplest model that exhibits this symmetry. Through this example some of the peculiar properties of PT-symmetric systems including PT symmetry breaking and non-orthogonality of modes are explained. Afterwards we consider the eigenmode equation of one-dimensional optical waveguides in paraxial and non-paraxial regimes and we show how PT symmetry can be imposed in optical waveguides due to similarity of the governing equations with that of quantum mechanics. Finally the necessary condition of PT symmetry is investigated for general optical waveguides and other electromagnetic media.

2.1. PT symmetry and real spectra

Consider the following general eigenvalue problem:

$$\mathcal{H}\psi(x) = \lambda\psi(x) \tag{2.1}$$

where $\mathcal{H}$ represents a Hamiltonian operator that is assumed to be PT-symmetric, i.e., it should commute with the parity-time ($\mathcal{PT}$) operator:

$$[\mathcal{H}, \mathcal{PT}] = 0 \tag{2.2}$$

Here the parity $\mathcal{P}$ and time $\mathcal{T}$ operators enforce a spatial reflection with respect to the center of x coordinate and a complex conjugation respectively:

$$\mathcal{P}\psi(x) = \psi(-x) \tag{2.3.a}$$

$$\mathcal{T}\psi(x) = \psi^*(x) \tag{2.3.b}$$

Since $\mathcal{H}$ and $\mathcal{PT}$ commute, they share the same set of eigenvectors ϕ_m with in general different eigenvalues:

$$\mathcal{H}\phi_m(x) = \lambda_m\phi_m(x) \tag{2.4.a}$$

$$\mathcal{PT}\phi_m(x) = \Omega_m\phi_m(x) \tag{2.4.b}$$

Note, however, that successive operations of the $\mathcal{PT}$ operator leads to the identity operator ($\mathcal{PTPT} = 1$) therefore $|\Omega_m|^2 = 1$ and this means that all the eigenvalues of the $\mathcal{PT}$ operator reside on the unit circle: $\Omega_m = e^{i\omega_m}$. As a result one can always renormalize the eigenvectors as $\phi_m(x) \to e^{-i\omega_m/2}\phi_m(x)$ to make all the eigenvalues of the $\mathcal{PT}$ operator unity. In this case:

$$\mathcal{PT}\phi_m(x) = \phi_m^*(-x) = \phi_m(x) \tag{2.5}$$

Let us now consider again the eigenvalue equation (2.4.a). After multiplying both sides with $\mathcal{PT}\phi_m(x)$ and integrating over the entire x axis one reaches at $\int_{-\infty}^{+\infty}\mathcal{PT}\phi_m(x)\mathcal{H}\phi_m(x)dx = \lambda\int_{-\infty}^{+\infty}\mathcal{PT}\phi_m(x)\phi_m(x)dx$ which in turn leads to

$$\lambda_m = \frac{\int_{-\infty}^{+\infty}\phi_m^*(-x)\mathcal{H}\phi_m(x)}{\int_{-\infty}^{+\infty}\phi_m(x)\phi_m^*(-x)} \tag{2.6}$$

On the other hand, by first applying the $\mathcal{PT}$ operator on both sides of Equation (2.4.a) and then multiplying by $\phi_m(x)$ and integrating again, we reach at $\int_{-\infty}^{+\infty}\phi_m(x)\mathcal{HPT}\phi_m(x) = \lambda_m^*\int_{-\infty}^{+\infty}\phi_m(x)\mathcal{PT}\phi_m(x)$, which leads to

$$\lambda_m^* = \frac{\int_{-\infty}^{+\infty} \phi_m(x)\mathcal{H}\phi_m^*(-x)}{\int_{-\infty}^{+\infty} \phi_m(x)\phi_m^*(-x)} \tag{2.7}$$

Given the fact that $\phi_m^*(-x) = \phi_m(x)$, a comparison between Equations (2.6) and (2.7) directly follows that all the eigenvalues are real since $\lambda_m = \lambda_m^*$.

Note that, based on Equations (2.6) and (2.7), one can define a new inner product in the Hilbert space spanned by the eigenstates of the PT-symmetric operator $\mathcal{H}$:

$$\langle \phi_n, \phi_m \rangle = \int_{-\infty}^{+\infty} \phi_m(x)\mathcal{P}\mathcal{T}\phi_n(x)dx = \int_{-\infty}^{+\infty} \phi_m(x){\phi_n}^*(-x)dx. \tag{2.8}$$

This definition contain all the conditions of an inner product. In fact, assuming f, g and h being three eigenfunctions of $\mathcal{H}$, the following properties directly follows; (a) conjugate symmetry $\langle g, f \rangle = \langle f, g \rangle^*$, (b) $\langle h, f + g \rangle = \langle h, f \rangle + \langle h, g \rangle$, (c) $\langle g, af \rangle = a\langle g, f \rangle$, and (d) $\langle f, f \rangle \geq 0$ while the equality holds if and only if $f(x) = 0$. It is then easy to show that the orthogonality relation between the basis functions ϕ_m can be represented in terms of this new inner product as:

$$\langle \phi_n, \phi_m \rangle = (-1)^m \delta_{mn} \tag{2.9}$$

In addition it has been shown that the eigenfunctions of the PT-symmetric operator $\mathcal{H}$ form a complete set [7]:

$$\sum_m (-1)^m \phi_m(x)\phi_m(x') = \delta(x - x') \tag{2.10}$$

As a result an arbitrary function can then be written as a sum of all the eigenfunctions of $\mathcal{H}$ as:

$$\Phi(x) = \sum_m a_m \phi_m(x) \tag{2.11}$$

where the coefficients a_m are obtained from the projections:

$$a_m = (-1)^m \langle \phi_m, \Phi \rangle \tag{2.12}$$

After this general overview, let us turn our attention to the Hamiltonian operator associated with the time-dependent Schrödinger equation $\mathcal{H} = -\frac{\hbar^2}{2m}\frac{d^2}{dx^2} + V(x)$ where the quantum mechanical potential is in general a complex function: $V(x) = V_R(x) + iV_I(x)$. One can simply show that this Hamiltonian commutes with the $\mathcal{PT}$ operator if the following condition is satisfies:

$$V^*(-x) = V(x). \tag{2.13}$$

This in turn means that the real and imaginary parts of this potential should be real and odd functions of position respectively.

2.2. PT symmetry breaking

It should be emphasized however that the commuting with the $\mathcal{PT}$ does not necessarily warrant that all the eigenvalues of a Hamiltonian $\mathcal{H}$ are real. In fact, there are scenarios where the Hamiltonian operator $\mathcal{H}$ commutes with the $\mathcal{PT}$ operator but the eigenvalue spectrum is partially or totally complex. In such cases, the two operators $\mathcal{H}$ and $\mathcal{PT}$ do not share the same set of eigenstates (therefore equations (2.4) to (2.7) are no longer valid) in

spite of the fact that they commute. Under these conditions the PT symmetry is said to be spontaneously broken. As a result, for a Hamiltonian that commutes with the $\mathcal{PT}$ operator, two regimes are distinguished; (a) exact PT phase regime, where the eigenvalues are entirely real, and (b) broken PT regime, where the eigenvalues are partially or entirely complex.

As mentioned before, PT operators are also discussed in the context of pseudo-Hermitian operators. In this regard it can be shown that a PT Hamiltonian in the exact PT phase regime can always be transformed to a Hermitian one [9]. On the other hand, under the same transformation this Hamiltonian is converted to a non-Hermitian Hamiltonian.

In the following section we show that PT-symmetric Hamiltonians can be realized in the optical domain.

2.3. PT-symmetric optical coupler

Perhaps one of the simplest arrangements of PT-symmetric structures in optics is that of a PT coupler [30]. As shown in Figure 2.1 this can be achieved by having two coupled waveguides or cavities. Let us assume first these two elements have different propagation constants and different amounts of gain or loss. We assume that these two elements are weakly coupled, and in addition we assume that the gain/loss values are small perturbations so that the Hermitian coupled mode theory gives a valid approximation.

Under these conditions, the evolution of the modal amplitudes in such system is governed by the following equation:

$$-i\frac{d}{d\xi}\begin{pmatrix}a\\b\end{pmatrix}=\begin{pmatrix}\delta_1+i\gamma_1 & \kappa\\ \kappa & \delta_1+i\gamma_1\end{pmatrix}\begin{pmatrix}a\\b\end{pmatrix}, \tag{2.14}$$

where δ_1, δ_2 denotes the propagation constant (resonance frequency) of the first and second waveguide (resonator) when being isolate and and γ_1, γ_2 represents the distributed gain or loss constant (depending on their sign) of each element. Finally, κ shows the coupling between the two elements. The evolution parameter ξ represents the longitudinal coordinate z in the case of optical waveguides or time t in the case of optical cavities. By assuming supermodes of the form $(a, b) = (A, B)e^{i\Omega\xi}$, Eq. (1) reduces to the following eigenvalue equation:

$$\begin{pmatrix}\delta_1+i\gamma_1 & \kappa\\ \kappa & \delta_1+i\gamma_2\end{pmatrix}\begin{pmatrix}A\\B\end{pmatrix}=\Omega\begin{pmatrix}A\\B\end{pmatrix}. \tag{2.15}$$

The corresponding Hamiltonian can be defied as the following 2×2 matrix:

$$\mathcal{H}=\begin{pmatrix}\delta+i\gamma & \kappa\\ \kappa & \delta-i\gamma\end{pmatrix}, \tag{2.16}$$

Obviously this is not a Hermitian operator (matrix) since in general $\mathcal{H}^\dagger \neq \mathcal{H}$. On the other hand, of our interest is to find appropriate parameters that makes $\mathcal{H}$ a PT-symmetric operator. For this reason, by assuming an arbitrary vector in two-dimensional vector space $\psi = (A\,, B)^T$ with arbitrary complex numbers A and B, we define the parity ($\mathcal{P}$) and time ($\mathcal{T}$) operators as follows:

$$\mathcal{P}\begin{pmatrix}A\\B\end{pmatrix}=\begin{pmatrix}B\\A\end{pmatrix}, \tag{2.17.a}$$

$$\mathcal{T}\begin{pmatrix}A\\B\end{pmatrix}=\begin{pmatrix}A^*\\B^*\end{pmatrix}. \tag{2.17.b}$$

Under this conditions it is straightforward to show that $\mathcal{H}$ satisfies the necessary condition of PT symmetry, i.e., $[\mathcal{PT},\mathcal{H}]=\mathcal{PTH}-\mathcal{HPT}=0$ if:

$$\delta_1=\delta_2=\delta \tag{2.18.a}$$

$$\gamma_1=-\gamma_2=\gamma \tag{2.18.b}$$

This simply means that the two elements should be identical in every aspect except for their gain/loss. While one elements exhibits certain amount of gain $+\gamma$, the other element should have the same amount of loss $-\gamma$. As a result, one expects real eigenvalues for the non-Hermitian operator $\mathcal{H}$, as long as PT symmetry is not broken. This can be shown by directly calculating the eigenvalues of Equation (2.15). Interestingly the eigenvalues can be distinguished in two different regimes. If the coupling constant is stronger than the gain loss contrast ($\kappa>\gamma$):

$$\Omega_{1,2}=\delta\pm\sqrt{\kappa^2-\gamma^2}, \tag{2.19.a}$$

$$\begin{pmatrix}A_{1,2}\\B_{1,2}\end{pmatrix}=\begin{pmatrix}1\\-i\,\gamma/\kappa\pm\sqrt{1-(\gamma/\kappa)^2}\end{pmatrix}. \tag{2.19.b}$$

Note that in this case both supermodes are symmetrically distributed between the two channels, i.e., $\left|A_{1,2}\right|^2=\left|B_{1,2}\right|^2$.

If on the other hand the gain/loss contrast exceeds the coupling strength ($\kappa < \gamma$), PT symmetry is said to be spontaneously broken. In this regime the eigenvalues are no longer real and instead they appear in the form of complex conjugate numbers:

$$\Omega_{1,2} = \delta \pm i\sqrt{\gamma^2 - \kappa^2}, \tag{2.20.a}$$

$$\begin{pmatrix} A_{1,2} \\ B_{1,2} \end{pmatrix} = \begin{pmatrix} 1 \\ -i\,\gamma/\kappa \pm i\sqrt{1-(\gamma/\kappa)^2} \end{pmatrix}. \tag{2.20.b}$$

Note that in this case the broken PT-symmetry regime, even the symmetry of the supermodes is lost since $|A_{1,2}|^2 \neq |B_{1,2}|^2$. Finally the behavior of this Hamiltonians becomes even more interesting at the PT-symmetry-breaking threshold that is the exact point where the transition between unbroken and broken symmetry regimes occurs ($\kappa = \gamma$). At this point both the eigenvalues are the same:

$$\Omega_{1,2} = \delta, \tag{2.21.a}$$

$$\begin{pmatrix} A_{1,2} \\ B_{1,2} \end{pmatrix} = \begin{pmatrix} 1 \\ i \end{pmatrix}. \tag{2.21.b}$$

Note that at this symmetry breaking threshold, not only the eigenvalues but also the eigenvectors are the same. In fact, the PT-symmetry breaking point shows all the characteristics of an exceptional point singularity. In general, exceptional points appear as singularities of non-Hermitian eigenvalue problems and can be compared with degeneracies in Hermitain operators. In contrast to the degeneracies, at an exceptional point both the eigenvalues and eigenvectors coalesce [31].

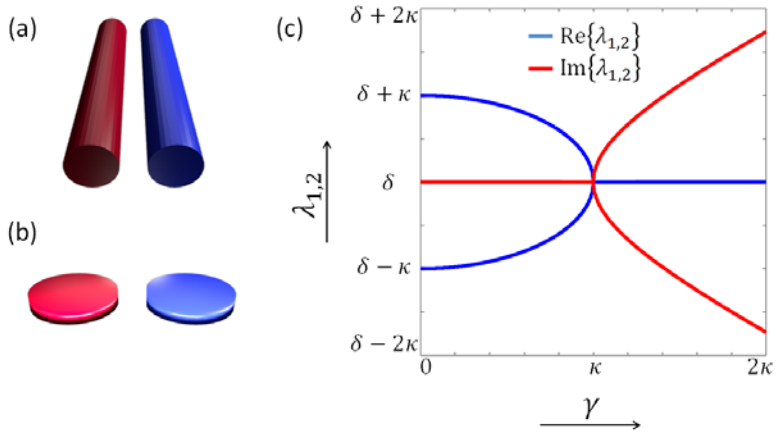

Figure 2.1. PT-symmetric arrangement of (a) coupled waveguides and (b) coupled microcavities. (c) Eigenvalues of the PT-symmetric coupler as a function of the gain/loss coefficient γ.

Here, it is worth noting that in general, as in other non-Hermitian system, in PT arrangements power is not conserved. As an example, in the PT coupler which is fully integrible one can simply show that in general $P = |a|^2 + |b|^2$ is not conserved during evolution in ξ. On the other hand it is straightforward to show that the quasi-power $Q = a^*b + b^*a$ is always conserved for any initial condition. This again has to do with the inner product in PT systems and will be discussed later in more complicated PT systems.

2.4. PT-symmetric wavguides: 1D

Consider now a dielectric waveguide which is described by a one-dimensional distribution of the relative permittivity along the x axis; $\epsilon(x) = n^2(x)$. In that case by considering time-harmonic waves propagating in the xy plane, the electric field component of the TE-polarized light satisfies the following equation:

$$\frac{\partial^2 E_z}{\partial x^2} + \frac{\partial^2 E_z}{\partial y^2} + k_0^2 \epsilon(x) E_z = 0. \tag{2.22}$$

By assuming eigenfunctions of the form $E_z(x, y) = \psi(x) \exp(i\beta z)$, Equation (2.22) reduces to

$$\frac{d^2\psi}{dx^2} + k_0^2 \epsilon(x)\psi(x) = \beta^2 \psi(x), \tag{2.23}$$

which is very similar to the Schrödinger equation where the Hamiltonian is defined as $\mathcal{H} = \frac{d^2}{dx^2} + k_0^2 \epsilon(x)$. In such a continuous system the parity and time operators are again defined as spatial reversal and complex conjugation as $\mathcal{P}\psi(x) = \psi(-x), \mathcal{T}\psi(x) = \psi^*(x)$. In this case the necessary condition of PT symmetry, i.e., $[\mathcal{PT}, \mathcal{H}] = 0$, demands that $\epsilon(x) = \epsilon^*(-x)$ which by assuming $\epsilon = \epsilon_R(x) + i\epsilon_I(x)$ leads to:

$$\epsilon_R(-x) = +\epsilon_R(x), \tag{2.24.a}$$

$$\epsilon_I(-x) = -\epsilon_I(x). \tag{2.24.b}$$

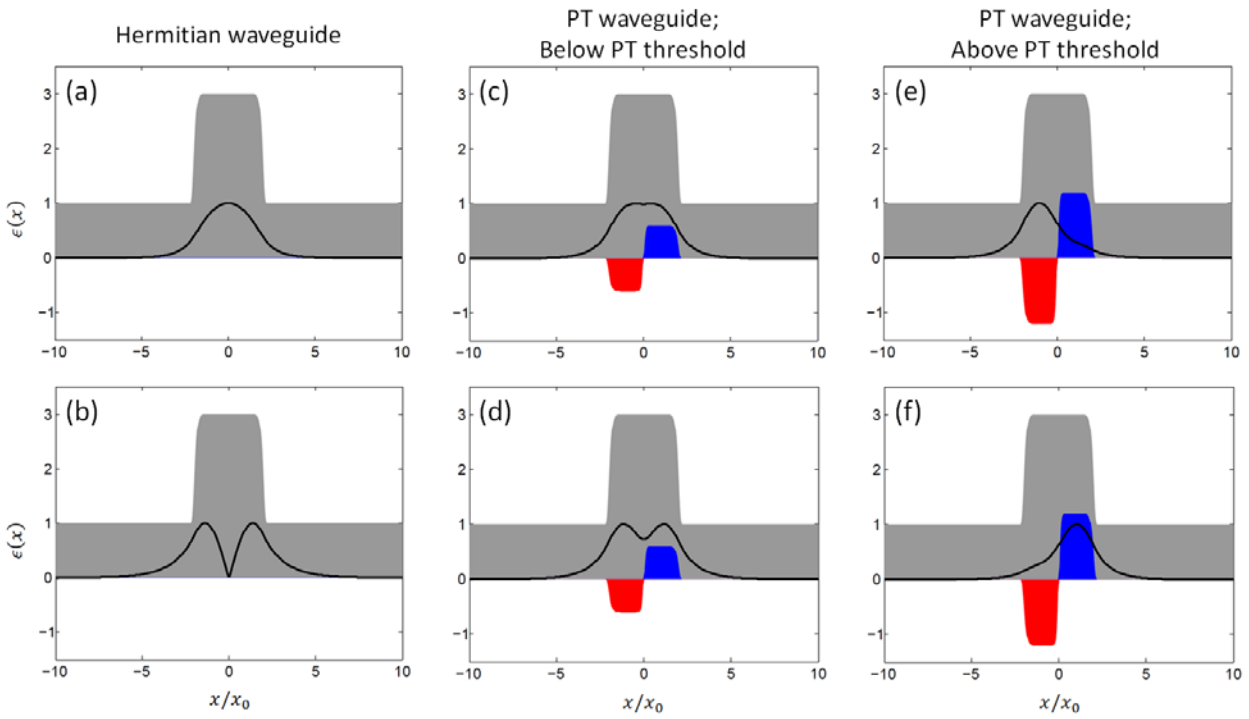

Figure 2.2. PT-symmetric waveguide with the following distribution of the relative permittivity: $\epsilon(x) = 1 + (2 + i\gamma \tanh(x/0.1)) \exp(-(x/2)^{20})$ where $\gamma = 0$ for (a,b), $\gamma = 0.6$ for (c,d) and $\gamma = 1.2$ in (e,f). Here the grey shows area the real part of the relative permittivity while the blue and red represent its imaginary part. In each case, absolute values of the two guided modes are shown by the solid black curve.

Figure 2.2 depicts an exemplary PT-symmetric slab waveguide when half of the waveguide involves gain (red) and the other half an equivalent amount of loss (blue). As shown in the figure by increasing the gain/loss contrast the symmetry of the guided mode breaks and one of the two modes lives mostly in the gain side while the other remains on the lossy

region. Similar results are obtained for a PT-symmetric arrangement of coupled waveguides as illustrated in Figure 2.3.

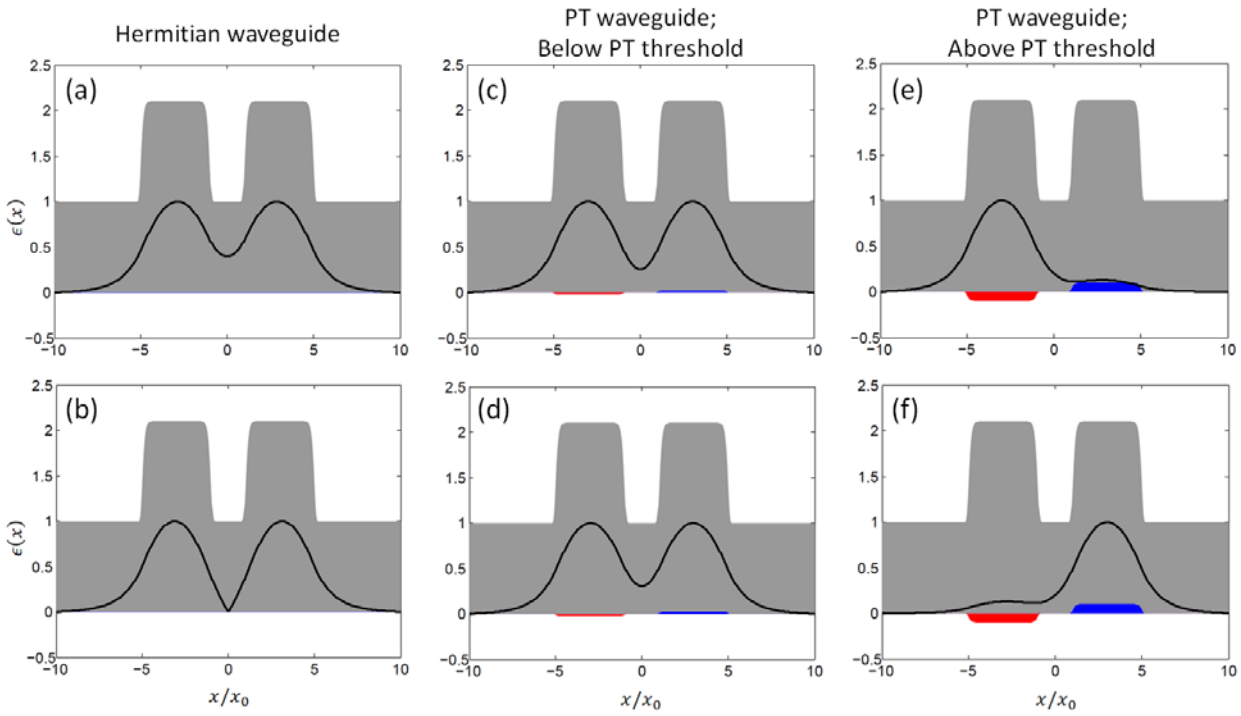

Figure 2.3. The same as Figure 2.2 when this time gain and loss regions are embedded into two different waveguides.

2.5. PT-symmetric waveguides: 2D

In previous section, the necessary condition of PT symmetry was found for a 1D waveguide. Here we extend this concept to general waveguides with arbitrary cross sections. Assume a

waveguide with a 2D cross section in the xy plane and uniform along the propagation direction z the electric and magnetic fields for the eigenmodes can be considered as:

$$\boldsymbol{E}(x,y,z) = \big(\boldsymbol{E}_t(x,y) + \boldsymbol{E}_z(x,y)\big)e^{i\beta z} \tag{2.25.a}$$

$$\boldsymbol{H}(x,y,z) = \big(\boldsymbol{E}_t(x,y) + \boldsymbol{E}_z(x,y)\big)e^{i\beta z} \tag{2.25.b}$$

where $\boldsymbol{E}_t, \boldsymbol{H}_t$ and $\boldsymbol{E}_z, \boldsymbol{H}_z$ represent the transverse and longitudinal components of the electric/magnetic fields respectively. Since the structure is uniform along the propagation direction z, after assuming the gradient operator as $\nabla = \nabla_t + \hat{z}\frac{\partial}{\partial z}$, the eignmode equations can be separated as transverse and longitudinal parts. The transverse electric and magnetic fields are governed by [32]:

$$\mathcal{L}_{E_t}\boldsymbol{E}_t = \beta^2\boldsymbol{E}_t \tag{2.26.a}$$

$$\mathcal{L}_{H_t}\boldsymbol{H}_t = \beta^2\boldsymbol{H}_t \tag{2.26.b}$$

where:

$$\mathcal{L}_{E_t} = \nabla_t^2 + \nabla_t\big((\nabla_{\mathrm{t}} \ln\epsilon)\cdot(\cdot)\big) + k_0^2\epsilon(x,y) \tag{2.27.a}$$

$$\mathcal{L}_{H_t} = \nabla_t^2 + (\nabla_t \ln\epsilon)\times\big(\nabla_{\mathrm{t}}\times(\cdot)\big) + k_0^2\epsilon(x,y) \tag{2.27.b}$$

In this again one can simply show that both of these operators can commute with the $\mathcal{PT}$ operators as long as:

$$\epsilon^*(-x,-y) = \epsilon(x,y) \tag{2.28}$$

2.6. PT-symmetry in a general electromagnetic media

PT symmetry can also be investigated in three-dimensional (3D) settings which are in general governed by the full-wave Maxwell's equations:

$$\nabla \times \boldsymbol{E} = i\omega\mu_0 \boldsymbol{H} \tag{2.29.a}$$

$$\nabla \times \boldsymbol{H} = -i\omega\epsilon_0 \epsilon(\boldsymbol{r})\boldsymbol{E} \tag{2.29.b}$$

$$\nabla \cdot \boldsymbol{D} = 0 \tag{2.29.c}$$

$$\nabla \cdot \boldsymbol{B} = 0 \tag{2.29.d}$$

where the relative permittivity $\epsilon(\boldsymbol{r})$ is a complex function of position for a linear, anisotropic and non-magnetic material. The curl equations can be combined to get the following equation [33]:

$$\nabla \times \left(\frac{1}{\epsilon(\boldsymbol{r})}\nabla \times \boldsymbol{H}\right) = \frac{\omega^2}{c^2}\boldsymbol{H} \tag{2.30}$$

which can be written as an eigenvalue problem $\mathcal{L}\boldsymbol{H} = \Omega\boldsymbol{H}$ where $\mathcal{L} = \nabla \times \left(\frac{1}{\epsilon(\boldsymbol{r})}\nabla \times (\cdot)\right)$ and $\Omega = \omega^2/c^2$. For a real valued permittivity, it is straightforward to show that the operator $\mathcal{L}$ is formally self-adjoint, meaning that for two arbitrary vector field $\boldsymbol{A}$ and $\boldsymbol{B}$

$$\int \boldsymbol{A}^* \cdot \mathcal{L}\boldsymbol{B}\, d^3\boldsymbol{r} = \int B \cdot \mathcal{L}\boldsymbol{A}^*\, d^3\boldsymbol{r} \tag{2.31}$$

where the integration is taken over the entire 3D space. Note that formally self-adjoint operators do not necessarily admit real-valued eigenvalues. In fact, in the context of

differential operators, being Hermitian demands additional conditions on the boundary conditions [34]. For example such conditions are not satisfied by the Sommerfeld's boundary condition at the infinity, as a result a dielectric sphere in the free space does not support any bound states. On the other such structure supports infinitely many *meta-stable states* all exhibiting complex eigenfrequencies where the imaginary parts represent the finite life-time of such states. Here it is worth noting that that Maxwell's Equations (2.29) can also be formulated in terms of the electric field as an eigenvalue problem $\frac{1}{\epsilon(\boldsymbol{r})}\nabla\times\nabla\times\boldsymbol{E}=\frac{\omega^2}{c^2}\boldsymbol{E}$. However, it can be easily shown that such equation is not even formally-self adjoint. Therefore we use the magnetic field formulation of Equation (2.30).

Now that we found out Equation (2.30) is formally self-adjoint for real-valued permittivities, of interest would be to find necessary condition for the complex permittivity so that operator $\mathcal{L}$ still remains formally self-adjoint. To show this, note that Equation (2.30) should still be valid for complex permittivities. It is straightforward to show that this equation is satisfied if

$$\epsilon^*(-\boldsymbol{r})=\epsilon(\boldsymbol{r}) \tag{2.32}$$

Finally, more general cases where the magnetic materials and anisotropy are also considered is discussed in reference [35].

2.7. References

1. C. M. Bender, and S. Boettcher, "Real spectra in non-Hermitian Hamiltonians having PT symmetry," Phys. Rev. Lett. **80**, 5243 (1998).

2. E. Delabaere, and F. Pham, "Eigenvalues of complex Hamiltonians with PT-symmetry. I," Phys. Lett. A **250**, 25 (1998).

3. C. M. Bender, S. Boettcher, and P. N. Meisinger, "PT-symmetric quantum mechanics," J. Math. Phys. **40**, 2201 (1999).

4. G. Levai and M. Znojil, "Systematic search for PT-symmetric potentials with real energy spectra," J. Phys. A: Math. Gen. 33, 7165-7180 (2000).

5. Z. Ahmed, "Real and complex discrete eigenvalues in an exactly solvable one-dimensional complex PT-invariant potential," Phys. Lett. A. **282**, 343 (2001).

6. C. M. Bender, M. V. Berry, P.M. Meisinger, V. M. Savage and M. Simsek, "Complex WKB analysis of energy-level degeneracies of non-Hermitian Hamiltonians," J.Phys.A. **34,** 31 (2001).

7. C. M. Bender, D. C. Brody, and H. F. Jones, "Complex extension of quantum mechanics," Phys. Rev. Lett. **89**, 270401 (2002).

8. C. M. Bender, M. V. Berry, A. Mandilara, "Generalized PT symmetry and real spectra," J. Phys. A. **35**, 467 (2002).

9. A. Mostafazadeh, "Pseudo-Hermiticity versus PT symmetry: The necessary condition for the reality of the spectrum of a non-Hermitian Hamiltonian," J. Math. Phys. (N.Y.) **43**, 205 (2002).

10. A. Mostafazadeh, "Pseudo-Hermiticity versus PT-symmetry. II. A complete characterization of non-Hermitian Hamiltonians with a real spectrum," J. Math. Phys. (N.Y.) **43**, 2814 (2002).

11. A. Mostafazadeh, "Pseudo-Hermiticity versus PT-symmetry III: Equivalence of pseudo-Hermiticity and the presence of antilinear symmetries," J. Math. Phys. (N.Y.) **43**, 3944 (2002).

12. Mostafazadeh, "Exact PT-symmetry is equivalent to Hermiticity," J. Phys. A: Math. Gen. **36**, 7081 (2003).

13. M. Bender, D. C. Brody, and H. F. Jones "Must a Hamiltonian be Hermitian?," Am. J. Phys. **71**, 1095 (2003).

14. M. Bender, D.C. Brody, H. F. Jones, and B. K. Meister, "Faster than Hermitian Quantum Mechanics," Phys. Rev. Lett. **98**, 040403 (2007).

15. M. Bender, "Making sense of non-Hermitian Hamiltonians," Rep. Prog. Phys. **70**, 947 (2007).

16. R. El-Ganainy, K. G. Makris, D. N. Christodoulides, and Z. H. Musslimani, "Theory of coupled optical PT-symmetric structures," Opt. Lett. **32**, 2632 (2007).

17. K. G. Makris, R. El-Ganainy, D. N. Christodoulides, and Z. H. Musslimani, "Beam Dynamics in PT Symmetric Optical Lattices," Phys. Rev. Lett. **100**, 103904 (2008).

18. Z. H. Musslimani, K. G. Makris, R. El-Ganainy, and D. N. Christodoulides, "Optical solitons in PT periodic potentials," Phys. Rev. Lett. **100**, 030402 (2008).

19. A. Guo, G. J. Salamo, D. Duchesne, R. Morandotti, M. Volatier-Ravat, V. Aimez, G. A. Siviloglou, and D. N. Christodoulides, "Observation of PT-symmetry breaking in complex optical potentials," Phys. Rev. Lett. **103**, 093902 (2009).

20. S. Longhi, "Bloch oscillations in complex crystals with PT symmetry," Phys. Rev. Lett. **103**, 123601 (2009).

21. K. G. Makris, R. El-Ganainy, D. N. Christodoulides, and Z. H. Musslimani, "PT-symmetric optical lattices," Phys. Rev. A **81**, 063807 (2010).

22. C. E. Rüter, K. G. Makris, R. El-Ganainy, D. N. Christodoulides, M. Segev, and D. Kip, "Observation of parity-time symmetry in optics," Nat. Phys. **6**, 192 (2010).

23. Z. Lin, H. Ramezani, T. Eichelkraut, T. Kottos, H. Cao, and D. N. Christodoulides, "Unidirectional invisibility induced by P T-symmetric periodic structures," Phys. Rev. Lett. **106**, 213901 (2011).

24. Y. D. Chong, L. Ge, and A. D. Stone, "PT-symmetry breaking and laser-absorber modes in optical scattering systems," Phys. Rev. Lett. **106**, 093902 (2011).

25. M.-A. Miri, A. Regensburger, U. Peschel, and D. N. Christodoulides, "Optical mesh lattices with PT symmetry," Phys. Rev. A **86**, 023807 (2012).

26. M.-A. Miri, P. LiKamWa, D. N. Christodoulides, "Large area single-mode parity-time-symmetric laser amplifiers," Opt. Lett. **37**, 764 (2012).

27. A. Regensburger, C. Bersch, M.-A. Miri, G. Onishchukov, D. N. Christodoulides, and U. Peschel, "Parity-time synthetic photonic lattices," Nature (London) **488**, 167 (2012).

28. L. Feng, Y. L. Xu, W. S. Fegadolli, M. H. Lu, J. E. Oliveira, V. R. Almeida, Y. F. Chen, and A. Scherer, "Experimental demonstration of a unidirectional reflectionless parity-time metamaterial at optical frequencies," Nat. Mater. **12**, 108 (2012).

29. A. Regensburger, M.-A. Miri, C. Bersch, J. Nager, G. Onishchukov, D. N. Christodoulides, and U. Peschel, "Observation of defect states in PT-symmetric optical lattices," Phys. Rev. Lett. **110**, 223902 (2013).

30. D. N. Christodoulides, M.-A. Miri, "PT symmetry in optics and photonics," SPIE Optics+Photonics, Active Photonic Materials VI, 9162-59, San Diego, CA (2014).

31. W. D. Heiss, "Repulsion of resonance states and exceptional points", Phys. Rev. E **61**, 929 (2000).

32. T. Tamir, "*Guided-Wave Optoelectronics*," Springler-Verlag, New York, 1988.

33. J. D. Joannopoulos, S. G. Johnson, J. N. Winn, and R. D. Meade, "*Photonic crystals: molding the flow of light*," Princeton University Press, Princeton (2008).

34. D. G. Dudley, "*Mathematical foundations for electromagnetic theory*," IEEE press, New York (1994).

35. G. Castaldi, S. Savoia, V. Galdi, A. Alù, and N. Engheta, "PT Metamaterials via Complex-Coordinate Transformation Optics," Phys. Rev. Lett. **110**, 173901 (2013).

CHAPTER THREE: MODE SELECTION IN PT-SYMMETRIC LASERS

High-power laser amplifiers nowadays play a crucial role in optics. Their applications range from cutting and welding to optically pumping other laser systems. In all occasions, extreme care is taken to avoid unwanted side effects arising from the delivery of such high power levels. These include, among others, nonlinear processes such as stimulated Raman and Brillouin scattering effects. Scaling up the cross section of the gain medium provides a natural way to achieve this goal. Not only does it lead to higher output powers, but it also provides a solution in reducing the impact of nonlinear effects. Unfortunately however, such an increase in size comes at a price: it makes the structure multimoded. This in turn has a detrimental effect on the output beam quality and the temporal stability of the laser itself.

In order to force these large area optical amplifiers to only lase in their fundamental mode, several strategies have been suggested. For broad area semiconductor laser amplifiers, the majority of these methods relies on spatial filtering. Modal reflectors [1], external cavities [2,3], and distributed feedback gratings [4] have been used as a means to increase the loss associated with higher order modes. Another approach is based on using tapers to gradually increase the width of the device while exciting only the fundamental mode [5]. For fiber laser amplifiers, on the other hand, several other approaches have also been proposed to address this problem. One way is to use large area endlessly single- mode photonic crystal fibers [6] or leakage channels structures [7]. Other schemes utilize the

distributed loss offered by coiled fibers to filter out higher order modes [8]. Selective excitation of the fundamental mode using ultrashort pulses was demonstrated in multimode fibers [9], while spatial doping has been used to achieve gain filtering among different modes [10]. Gain guiding with index antiguiding provides yet another technique for single- mode large area lasers [11]. Given that none of the aforementioned methods can single-handedly address all the underlying problems in this area, of interest will be to explore alternative routes to achieve this goal for both one- and two-dimensional structures in different geometries.

Here, we propose a novel avenue in order to encourage single-mode operation of large area optical amplifiers. This is done by exploiting recently developed notions in parity–time (PT) symmetric optics. As we will see, what distinguishes this new class of systems from the previously mentioned schemes is that only the fundamental mode experiences gain while all the higher order modes undergo oscillations and hence remain neutral.

3.1. PT symmetry breaking and transverse mode selection in laser cavities

In this section we show that the concept of PT-symmetry can be utilized for filtering higher order transverse modes in a large area laser cavity. For this reason, let us consider a structure composed of two identical multimode waveguides coupled to each other (Figure .1).

Figure 3.1. A pair of coupled PT-symmetric multimode waveguides

In this case, PT symmetry around the central axis demands that one of the waveguides exhibits gain while the other an equal amount of loss. By considering only coupling effects between identical modes, the evolution of the modal amplitudes a_m and b_m of the $m'th$ modes in these two guides is described through the coupled mode equations:

$$\frac{da_m}{dz} = i\beta_m a_m + i\kappa_m b_m + g_m a_m \tag{3.1.a}$$

$$\frac{db_m}{dz} = i\beta_m b_m + i\kappa_m a_m - g_m b_m \tag{3.1.b}$$

where, β_m is their respective propagation constant, κ_m is coupling coefficient among these modes and $\pm g_m$ stands for the modal gain or loss in the $m'th$ mode.

The solution of these coupled wave equations, can be obtained through their respective supermodes. For convenience we introduce the dimensionless quantity $\rho_m = g_m/\kappa_m$. Two regimes are identified. If the system is kept below threshold ($\rho_m < 1$) the two supermodes are:

$$\binom{a_m}{b_m} = \binom{1}{\pm\exp(\pm i\theta_m)} \exp(\pm i\kappa \cos(\theta_m)\, z) \exp(i\beta_m z) \tag{3.2}$$

where $\sin(\theta_m) = \rho_m$. Note that in this case none of the modes experiences gain-instead they both remain neutral and therefore oscillate during propagation. If on the other hand $\rho_m > 1$ then:

$$\binom{a_m}{b_m} = \binom{1}{i\exp(\pm\theta_m)} \exp(\mp\kappa \sinh(\theta_m)\, z) \exp(i\beta_m z) \tag{3.3}$$

where $\cosh(\theta_m) = \rho_m$. In this case, the PT-symmetry is "spontaneously broken" and hence one of the two supermodes enjoys amplification while the other decays exponentially with distance. The limit $\rho_m = 1$ designates this transition point.

To understand how the proposed arrangement works, one has to bear in mind that the coupling coefficient between higher-order modes is typically higher than that for lower ones like the fundamental. Hence for a given gain level, ρ_m is expected to be higher for lower-order modes. If the system is appropriately designed, then only the fundamental mode will exhibit a ratio, $\rho_1 > 1$ while the rest are kept below unity. As a result, only the fundamental mode will experience PT-symmetry breaking and thus will be amplified. On the hand, the rest of the modes will be neutral and therefore remain bounded in amplitude (as in Equation (3.2)), exhibiting oscillations.

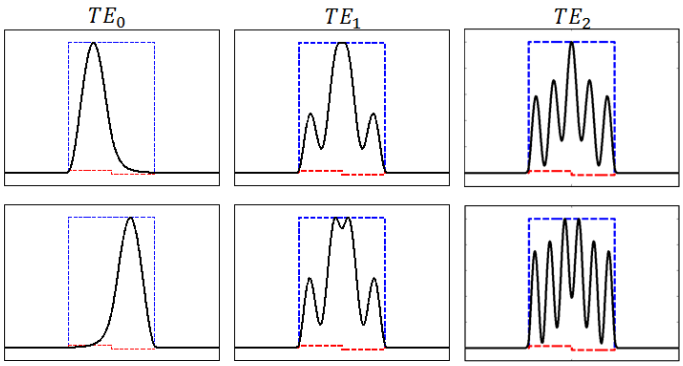

Figure 3.2. Field intensity profile of the first six TE modes.

In what follows we provide pertinent examples to elucidate this possibility. First we consider a semiconductor amplifier waveguide system consisting of two identical PT-symmetric ridge guides in contact to each other. The index in this region is throughout the same while one guide experiences gain and the other an equal amount of loss. Each waveguide is taken here to be 30μm thick and the operating wavelength is assumed to be 1μm. The substrate has a refractive index of 3.5 while the core has a relatively high index contrast of 0.003 compared to the substrate so as to discourage any beam filamentation effects arising from spatial hole burning. A bulk gain/loss of $\pm 5.906\ \mathrm{cm}^{-1}$ is assumed in these two regions of this waveguide. Table.1. provides the effective index of the first six TE modes while the intensity profile of the first six is depicted in Figures 3.2(a-f). Evidently only the first pair of super modes (corresponding to the fundamental TE_0 in each region) is in the broken phase regime while the rest of the modes lie below threshold and hence they are neutral. Figure 3.2 illustrates the main difference between broken phase modes and ordinary modes in this PT-symmetric structure. For modes kept below threshold the

optical intensity is symmetric while for those with broken symmetry is asymmetric. Note that one of these latter modes mostly lies in the gain region and is hence amplified while the other one occupies the loss region and is attenuated.

Table 3.1. Complex effective indices of the first TE modes of a large area semiconductor laser

Mode number	Complex effective index	Gain/Loss (cm^{-1})
TE_0	$3.502973 + i0.00003976$	-5
TE_0	$3.502973 - i0.00003976$	$+5$
TE_1	3.502891	0
TE_1	3.502877	0
TE_2	3.502765	0
TE_2	3.502674	0

We also analyze a two dimensional PT fiber based system. In such arrangements higher-order modes may not necessarily have the highest coupling. In fact the coupling in this case depends on the nature of the mode itself [12]. As an example we consider two circular cores each having a diameter of 60μm-in contact with each other. Such double-core arrangements may be feasible by appropriately structuring the fiber preform [13]. The refractive index of the core and cladding regions is assumed to be 1.535 and 1.534 respectively, corresponding to a numerical aperture of 0.055. A differential gain/loss of

$\pm 0.5\ \mathrm{cm}^{-1}$ is assumed that is typical of phosphate glass laser amplifiers [14]. The operating wavelength is 1.54 μm.

According to finite element simulations the fundamental LP_{01} is not the first mode to experience symmetry breaking. Instead two degenerate pairs (one for each polarization) of the LP_{11} supermodes are the first to break the PT symmetry in this example, experiencing a gain/loss of $\pm 0.4541\ \mathrm{cm}^{-1}$. This result can be explained through Figure 3.3 which shows the intensity profile for the x-polarized LP modes of this structure. As this figure indicates, a specific set of LP_{11} modes has very small overlap, and thus their coupling coefficient is lower than that of the fundamental LP_{01}. As a result they are the first to break the PT symmetry.

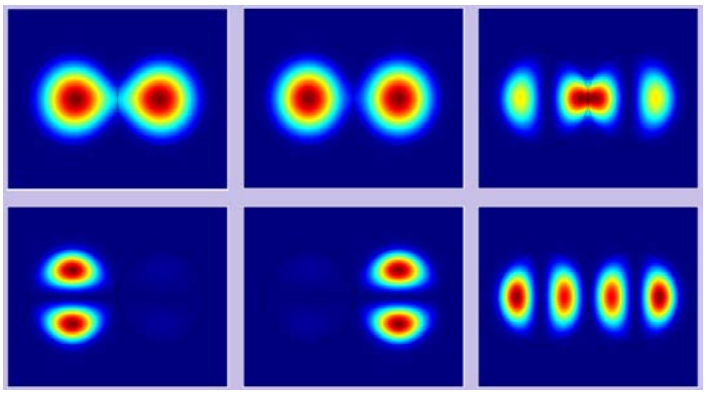

Figure 3.3. Intensity profile of the first few modes in the PT fiber laser.

To overcome this problem, we confine the gain/loss process in two cocentric cylindrical regions of 20μm in diameter, as shown in Figure 3.4 In this case the two cores are also further separated by 6.8μm to decrease the coupling constants. Figure 3.4 shows the

intensity profile of the first few x-polarized modes of this new structure. In this case the fundamental LP_{01} mode is the first to break the symmetry and its modal gain/loss is approximately $\pm 0.1\ \mathrm{cm}^{-1}$. Thus this coupled multimode PT-symmetric structure is expected to lase only in the fundamental mode (of the gain region) while all higher-order modes will remain neutral.

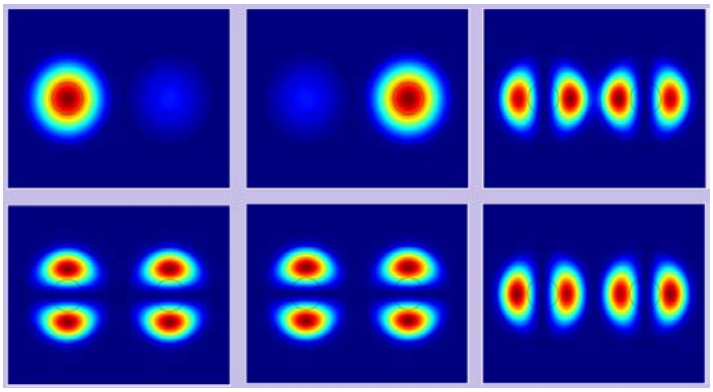

Figure 3.4. Intensity profile of the first few modes in a PT-symmetric multi-moded coupled system. Gain/loss is provided within the dashed area.

Finally it is important to note that many of these features associated with PT-symmetry can actually persist in spite of imperfections and perturbations, like for example bending, thermal and saturation effects that may spoil the assumed symmetry. In principle, appreciable losses can be introduced to the system by scattering regions so as to avoid any unnecessary thermal effects because of absorption. However, on many occasions this perfect symmetry may not be absolutely essential in exploiting these effects. For example, let us consider a perturbed PT system where the m'th mode in the first waveguide

experience a modal gain of $+g_m^{(1)}$ while this same mode in the second one experiences a loss of $-g_m^{(2)}$. In this case, if we define a common gain/loss factor of $\pm g_m = \pm\left(g_m^{(1)} + g_m^{(2)}\right)/2$, it is straightforward to show that Equations (3.2) and (3.3) still hold under these same conditions provided that a net gain(or loss depending on the sign) of $\left(g_m^{(1)} - g_m^{(2)}\right)/2$ is added to all modes. Thus, some of the higher-order modes may no longer be neutral. Yet, even in the presence of such imperfections, single-mode operation can be restored by appropriately shifting the overall zero gain/loss line of the structure. Essentially, perturbations in the spectrum tend to increase linearly with the strength of such asymmetries.

3.2. PT-symmetric micro-ring lasers

Micro-ring resonators due to their high confinement and high quality factor of their whispering gallery modes serve as ideal cavities for many applications. In fact, as shown in Appendix A, in coupled micro-ring resonator systems, PT-symmetry-breaking can occur at lower gain values. This is due to the fact that in such systems, coupling occurs in a small frction of the rings while gain or loss mechanism take place in the entire ring. This makes micro-ring resonator systems ideal platform for observation of PT-symmetry-breaking. Several recent studies have demonstrated PT related phenomena in micro-ring resonator

arrangements [15-17]. Here we show that PT-based single mode lasing can be observed in micro-ring resonators.

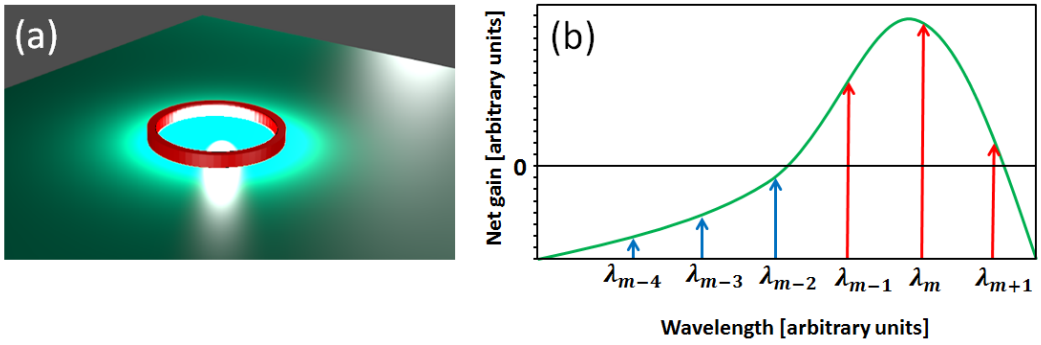

Figure 3.5. A micro-ring laser with an exemplary gain spectrum.

Consider first a single micro-ring resonator (Figure 3.5(a)) with an exemplary gain bandwidth as depicted in Figure 3.5(b). The lasing frequencies or the resonances of the corresponding passive micro-ring should in general be obtained through a full-wave solution of Maxwell's equation. In a first order approximation however, the micro-ring can be considered as a curved waveguide that closes to itself. Therefore the resonance condition can be interpreted as a condition for constructive interference of a waveguide mode that travels in the ring. Therefore, assuming an effective propagation index of $n_{\mathrm{e}}(\lambda)$ for the straight waveguide, the resonance condition of the micro-ring resonator turns to be $k_0 n_{\mathrm{e}} l_{\mathrm{ring}} = 2\pi m$ which directly leads to:

$$\frac{2\pi R}{\lambda_m} n_{\mathrm{e}}(\lambda_m) = m, \tag{3.4}$$

where R represents the effective radius of the micro-ring resonator. Based on this relation, the free spectral range (FSR) can be easily calculated as $\mathrm{FSR} = \lambda_m - \lambda_{m+1} \approx \frac{\lambda_m^2}{2\pi R\, n_\mathrm{g}(\lambda_m)}$ where $n_\mathrm{g}(\lambda) = n_\mathrm{e}(\lambda) - \lambda \frac{\partial n_\mathrm{e}}{\partial \lambda}$ represents the effective group index of the corresponding waveguide. Typically, the free-spectral range of micro-ring resonators is much less than the gain bandwidth as a result, several resonances of a single micro-ring resonator may fall within the gain bandwidth and therefore all can lase at the same time. This situation becomes even worse when the corresponding waveguide supports more than one transverse modes. In this case, several longitudinal variations of each transverse mode can fall into the gain spectrum and therefore the resulting laser becomes highly multi-moded.

As we will show in the next sections, the concept of PT symmetry can be utilized to filter out both longitudinal and transverse modes in micro-ring resonator systems. The experimental results, which completely support our theoretical predictions, are also presented in these sections.

3.3. Longitudinal mode filtering

Consider the micro-ring laser of Figure 3.6 when being accompanied with another micro-ring resonator which is any aspect identical with the original ring except that is involves loss instead of gain. In this case again the temporal evolution of the m^{th} mode pairs of this coupled system can be described via the temporal coupled mode equations:

$$\frac{da_m}{dt} = -i\omega_m a_m + i\mu_m b_m + \gamma_{a_m} a_m, \tag{3.5.a}$$

$$\frac{db_m}{dt} = -i\omega_m b_m + i\mu_m a_m + \gamma_{b_m} b_m, \tag{3.5.b}$$

where μ_m represents the coupling coefficient between the m^{th} modes of the two resonators and $\gamma_{a_m}, \gamma_{b_m}$ model the net gain/loss (depending on its sign) of the two resonators which include all the losses due to absorption, radiation and scattering as well as the gain due to the quantum wells. It is worth noting that here we use μ and γ for the coupling and gain/loss coefficient of the microring resonators in the time-domain coupled mode equations as opposed to the κ and g which we use for the coupling and gain coefficients of the corresponding waveguides in the space-domain coupled mode equations. The relation between these parameters is calculated in Appendix A. By assuming eigenmodes of the form:

$$\begin{pmatrix} a_m(t) \\ b_m(t) \end{pmatrix} = \begin{pmatrix} A_m \\ B_m \end{pmatrix} e^{-i\omega_m t} \tag{3.6}$$

The eigenfrequencies are obtained to be:

$$\omega_m^{(1,2)} = \omega_m + i\frac{\gamma_{a_m}+\gamma_{b_m}}{2} \pm \sqrt{\mu_m^2 - \left(\gamma_{a_m}/2 - \gamma_{b_m}/2\right)^2} \tag{3.7}$$

Obviously these eigenfrequencies are in general complex. Depending on the sign of each eigenfrequcy the corresponding mode will be either lasing or attenuating. Therefore, in order to have a single mode laser, all the eigenfrequnecies should have a negative

imaginary part except for one mode. This last equation can be understood under perfect PT-symmetric conditions where $\gamma_{a_m} = -\gamma_{b_m} = \gamma_m$. In this case, equation (3.7) reduces to:

$$\omega_m^{(1,2)} = \omega_m \pm \sqrt{\mu_m^2 - \gamma_m^2}. \tag{3.8}$$

According to this relation, to have a single mode laser, the coupling level should be adjusted so that only a pair of modes can break their PT symmetry while the rest of the modes remain neutral. As illustrated in Figure 3.6, this can be achieved as long as $\gamma_{sc} < \mu < \gamma_{max}$ where γ_{max} represents the net gain of the dominant lasing mode and γ_{sc} that of the strongest competing mode.

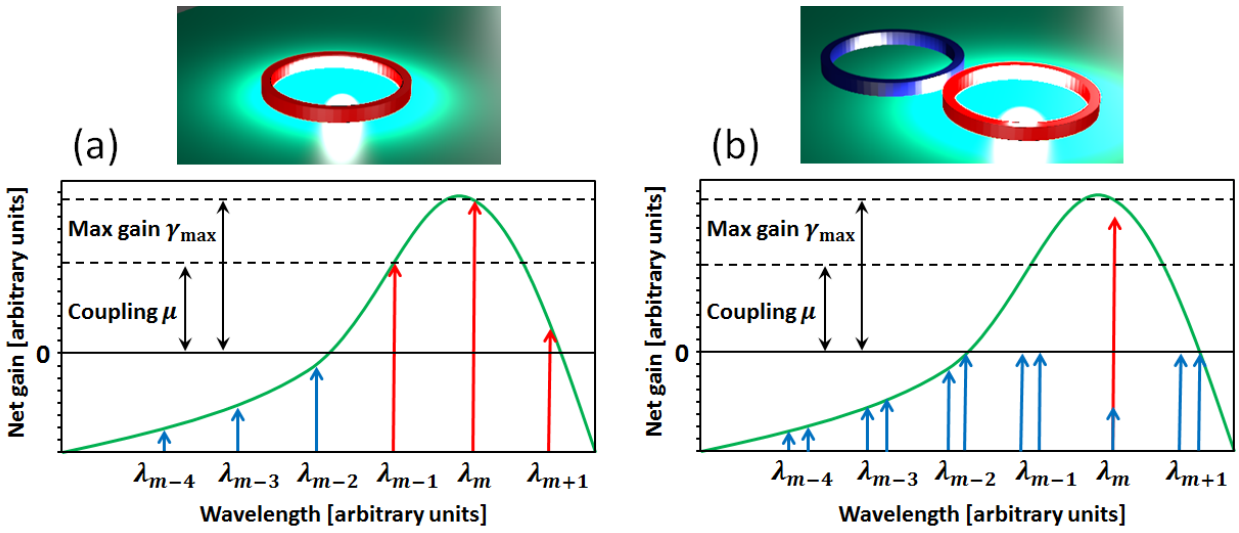

Figure 3.6. The lasing spectrum of (a) single and (b) PT-symmetric micro-ring lasers.

It is worth noting that single-mode operation can also be achieved in a single micro-ring laser simply by increasing the overall loss of the system, so that only the dominant mode

can experience a net gain while even the strongest competing mode cannot overcome the losses. In this case, however the net gain of the lasing mode cannot exceed $\gamma_{\max} - \gamma_{\mathrm{sc}}$. On the other in the case of the single mode PT-symmetric laser the maximum gain is achieved when the coupling level is set to be equal to the gain of the strongest competing mode, i.e., $\mu = \gamma_{sc}$. Therefore, according to Equation (3.8), the maximum gain achieved in the PT laser is $\sqrt{\gamma_{\max}^2 - \gamma_{\mathrm{sc}}^2}$. Obviously, compared to the single-mode single ring laser, the gain of the PT laser is enhanced by a factor η which is:

$$\eta = \frac{\sqrt{\gamma_{\max}^2 - \gamma_{\mathrm{sc}}^2}}{\gamma_{\max} - \gamma_{\mathrm{sc}}} = \sqrt{\frac{1+\gamma_{\mathrm{sc}}/\gamma_{\max}}{1-\gamma_{\mathrm{sc}}/\gamma_{\max}}}. \tag{3.9}$$

3.3.1. Design and simulations of PT micro-ring lasers

The micro-ring resonators used in the experiment are based on Indium-Phosphide (InP) and are buried in a silica glass substrate [17]. The active regions are obtained by embedding six layers of Indium-Gallium-Arsenide-Phosphide (InGaAsP) quantum wells inside the rings [17]. Each ring has an outer radius of $R_{\mathrm{o}} = 10\mu\mathrm{m}$ while the widths and heights are $w = 500\mathrm{nm}$ and $h = 210\mathrm{nm}$ respectively. In simulations the refractive index of the rings and its surrounding medium are assumed to be $n_{\mathrm{g}} = 3.4$, and $n_{\mathrm{c}} = 1.45$ at telecommunication wavelength $\lambda_0 = 1.55\mu\mathrm{m}$ respectively. Let us first consider the corresponding waveguide of a single ring. According to finite element simulations, such waveguide supports three different modes. The fundamental mode is a TE polarized mode

which has the most overlap with the active regions and therefore experiences the maximum amount of gain. On the other had the second TE mode is close to its cutoff while the only TM mode does not have a significant overlap with the quantum wells. As a result we only consider the fundamental TE mode in our analysis.

The coupling coefficient between the two rings can be roughly estimated from the coupling constant between the associated straight waveguides and the effective coupling length (See Appendix A).

Finally it is worth noting that simulations of a straight waveguide cannot fully represent the behavior of a curved waveguide. In fact due to such curvature, the mode profiles will be distorted and shift toward the opposite direction of the bend [18]. This effect becomes even more prominent at lower radii of curvatures.

3.3.2. Experimental results

In experiment, two micro-rings are put in a close proximity $d = 200$nm. The gain and loss regions are obtained by selectively pumping one of the two rings as depicted in Figure 3.7. While the pump laser operates at $\lambda_0 = 1064$ nm, the gain bandwidth obtained from active regions ranges from 1350nm to 1600nm.

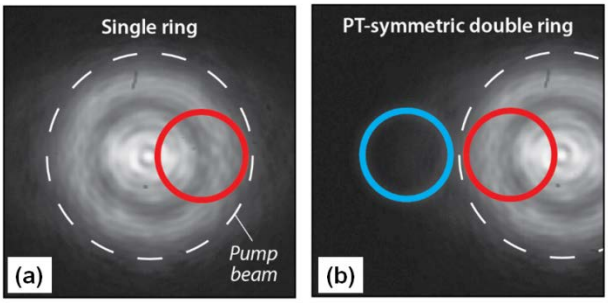

Figure 3.7. Achieving gain and loss regions via selective pumping of the micro-ring resonators [17]

The lasing spectrum of the single and PT-symmetric micro-ring lasers are shown in Figure 3.8. According to this figure, while the single ring lases prominently at four modes, single-mode-lasing is enforced in the PT-symmetric system.

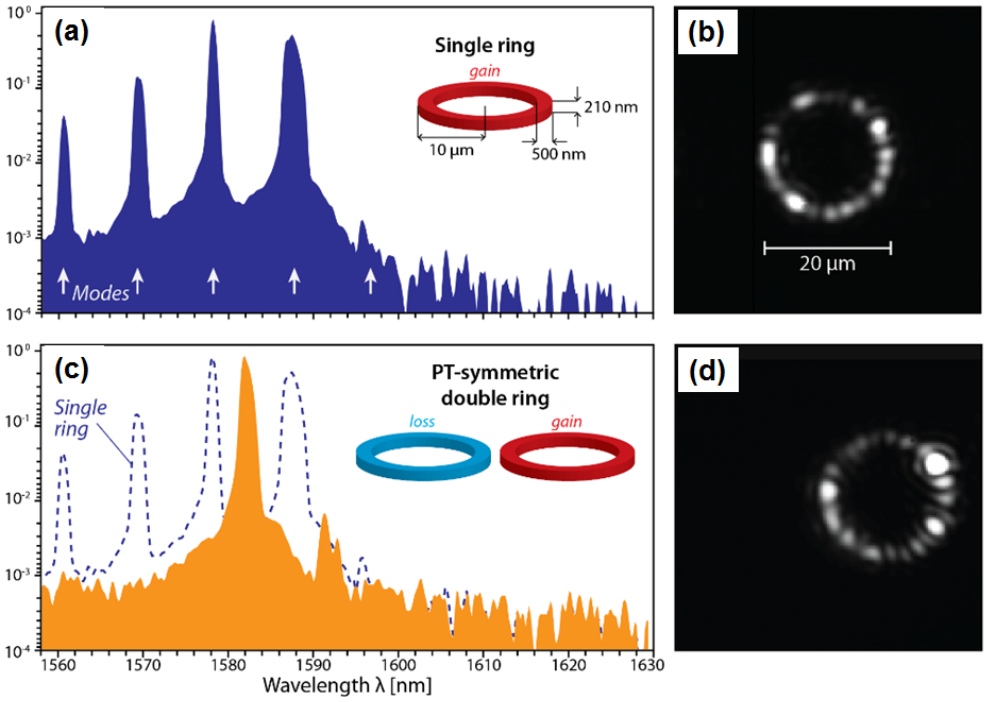

Figure 3.8. The lasing spectrum and the corresponding intensity pattern of (a,b) the single and (c,d) PT-symmetric micro-ring lasers [17]

3.4. Transverse mode filtering

As mentioned in previous sections, if a micro-ring resonator supports several transverse modes, the number of lasing modes increases tremendously. As we will show in this section, similar strategies can be used to suppress both the transverse and longitudinal modes at the same time. In a different experiment, we considered micro-ring resonators with outer radii of $R_o = 6\mu m$ and with widths of $w = 1.5\mu m$. As depicted in finite element simulations of Figure 3.9, this time the each ring supports four transverse TE modes.

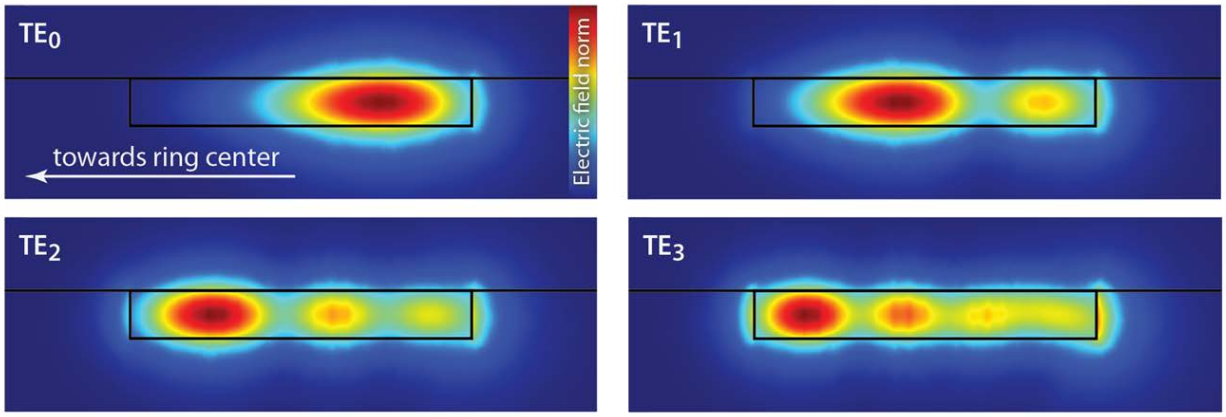

Figure 3.9. Different transverse modes of a micro-ring resonators with a width of $w = 1.5\mu m$ and an outer radius of $R_o = 6\mu m$.

As shown in Figure 3.10(a), a single micro-ring lases in six prominent modes. According to simulations all these modes, are different longitudinal variations of the TE_0 and TE_1 modes. As we expect, in the PT-symmetric arrangement, all longitudinal versions of the transverse TE_1 mode will be suppressed simultaneously (Figure 3.10(b)). On the other hand, by adjusting the power level, two longitudinal variations of the TE_0 mode can also be suppressed to achieve a single mode laser (Figure 3.10(c)).

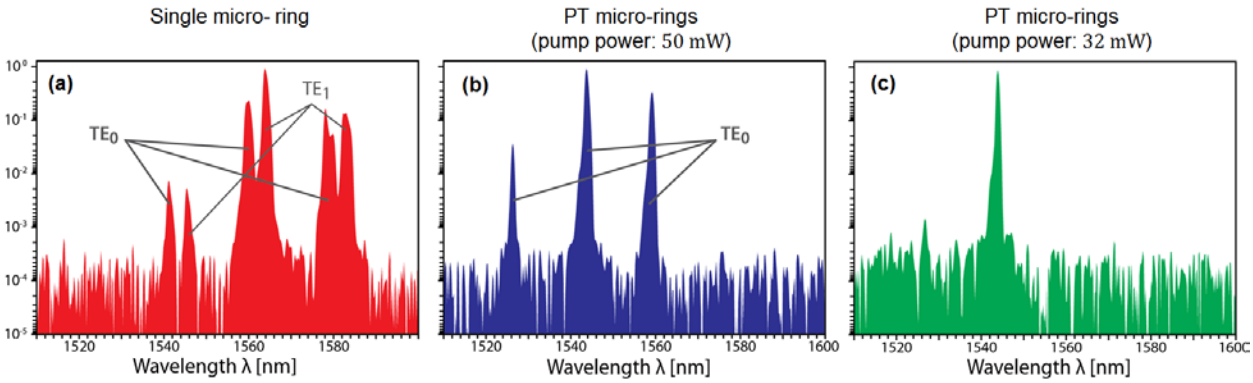

Figure 3.10. Lasing spectrum of (a) single micro-ring and (b,c) PT-symmetric micro-ring lasers. For a certain power level in the PT arrangement, all longitudinal variations of the TE_1 mode can be removed at once as shown in part (b). In addition by further adjusting the power level, only one longitudinal version of the TE_0 modes survives as depicted in part (c).

3.5. References

1. M. Szymanski, J. M. Kubica, P. Szczepanski and B. Mroziewicz, "A theory of broad-area semiconductor lasers with modal reflectors", J. Phys. D: Appl. Phys. **30**, 1181 (1997).

2. L. Goldberg and J. F. Weller, "Narrow lobe emission of high power broad stripe laser in external resonator cavity", Electron. Lett. **25**, 112 (1989).

3. S. Wolff, D. Messerschmidt and H. Fouckhardt, "Fourier-optical selection of higher order transverse modes in broad area lasers", Opt. Express. **5**, 32 (1999).

4. R. J. Lang, K. Dzurko, A. A. Hardy, S. Demarrs, A. Schoenfelder, and D. F. Welch, "Theory of grating-confined broad-area lasers", IEEE, J. Quant. Elect. **34**, 2196 (1998).

5. J. N. Walpole, E. S. Kintzer, S. R. Chinn, C. A. Wang, and L. J. Missaggia, "Highpower strainedlayer InGaAs/AlGaAs tapered traveling wave amplifier", Appl. Phys. Lett. **61**, 740 (1992).

6. J. Limpert, T. Schreiber, S. Nolte, H. Zellmer, T. Tunnermann, R. Iliew, F. Lederer, J. Broeng, G. Vienne, A. Petersson, and C. Jakobsen, "High-power air-clad large-mode-area photonic crystal fiber laser", Opt. Express. **11**, 818 (2003).

7. L. Dong, X. Peng, and J. Li, "Leakage channel optical fibers with large effective area", J. Opt. Soc. Am. B. **24**, 1689 (2007).

8. J. P. Koplow, D. A. V. Kliner, and L. Goldberg, "Single-mode operation of a coiled multimode fiber amplifier", Opt. Lett. **25**, 442 (2000).

9. M. E. Fermann, “Single-mode excitation of multimode fibers with ultrashort pulses”, Opt. Lett. **23**, 52 (1998).

10. J. R. Marciante, “Gain filtering for single-spatial-mode operation of large-mode-area fiber amplifiers”, IEEE, J. Sel. Top. Quantum Electron. **15**, 30 (2009).

11. A. E. Siegman, Y. Chen, V. Sudesh, M. C. Richardson, M. Bass, P. Foy, W. Hawkins, and J. Ballato, “Confined propagation and near single-mode laser oscillation in a gain-guided, index antiguided optical fiber”, Appl. Phys. Lett. **89**, 251101 (2006).

12. K. Ogawa, “Simplified theory of multimode fiber coupler”, Bell Syst. Tech. J. **56**, 729 (1977).

13. Y. W. Lee, M. J. F. Digonnet, S. Sinha, K. E. Urbanek, R. L. Byer, and S. Jiang, “High-power Yb^{3+}-doped phosphate fiber amplifier”, IEEE, J. Sel. Top. Quantum Electron. **15**, 93 (2009).

14. S. Jiang, T. Luo, B. C. Hwang, F. Smekatala, K. Seneschal, J. Lucas, N. Peyghambarian, “Er^{3+}-doped phosphate glasses for fiber amplifiers with high gain per unit length”, J. Non-Crystalline Solids. **263&264**, 364 (2000).

15. B. Peng, S. K. Ozdemir, F. Lei, F. Monifi, M. Gianfreda, G. L. Long, S. Fan, F. Nori, C. M. Bender, and L. Yang, “Parity–time-symmetric whispering-gallery microcavities,” Nature Phys. **10**, 394 (2014).

16. L. Chang, X. Jiang, S. Hua, C. Yang, J. Wen, L. Jiang, G. Li, G. Wang and M. Xiao, “Parity–time symmetry and variable optical isolation in active–passive-coupled microresonators,” Nat. Photon. **8**, 524 (2014).

17. H. Hodaei, M.-A. Miri, M. Heinrich, D. N. Christodoulides, and M. Khajavikhan, “PT-symmetric microring lasers: Self-adapting broadband mode-selective resonators,” arXiv preprint, arXiv:1405.2103 (2014).

18. M.-A. Miri, H. Hodaei, M. Heinrich, D. N. Christodoulides, and M. Khajavikhan, “PT-symmetric micro-ring lasers,” FiO/LS, Tucson, AZ (October 2014).

19. D. Marcuse, “Field deformation and loss caused by curvature of optical fibers,” J. Opt. Soc. Am. **66**, 311 (1976).

CHAPTER FOUR: SCATTERING PROPERTIES OF PT-SYMMETRIC OBJECTS

In this section, the scattering of light from PT-symmetric dielectric objects is studied. In order to avoid dealing with vectorial fields we restrict our attention to two-dimensional objects that are infinitely long in the third dimension. In particular we consider a PT-symmetric Janus-like dielectric cylinder that involves half gain and the half loss as shown in Figure 4.1.

We show that such a structure can deflect the scattered light through a certain angle that is related to the gain/loss contrast. In addition, as we will see, such objects are highly anisotropic and the far-filed scattering pattern can change with the angle of incidence. Finally we discuss two important issues related to the general scattering properties of PT-symmetric structures; the associated optical theorem and reciprocity relations.

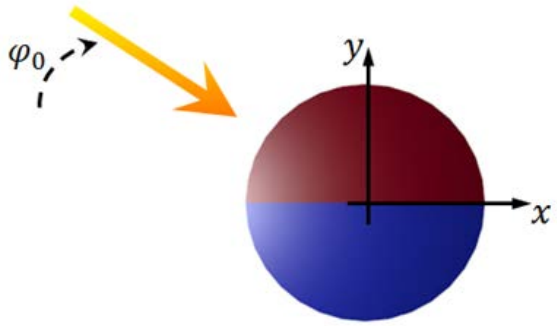

Figure 4.1. Plane wave incident on a PT-symmetric dielectric cylinder where red and blue represent the gain and loss regions respectively.

4.1. Mathematical formulation

As discussed in previous chapters, in general, a dielectric object respects PT symmetry provided that its relative electric permittivity satisfies:

$$\epsilon^*(-\boldsymbol{r}) = \epsilon(\boldsymbol{r}). \tag{4.1}$$

This latter relation directly indicates that for this symmetry to hold, the real part of permittivity (or refractive index) must be an even function of the position vector while its imaginary (gain/loss profile) must be antisymmetric. For example this condition can be readily observed in homogeneous (in terms of their refractive index) Janus spherical or cylindrical configurations where one half exhibits gain while the other an equal amount of absorption. Other more involved PT-symmetric patterns can also ensue from Equation (4.1) in both 2D and 3D systems.

To demonstrate these effects, let us consider a two-dimensional dielectric body in the xy plane. For reasons of simplicity, we restrict our analysis to the TE case where the electric field component $E_z = E(\boldsymbol{r})e^{-i\omega t}$ is perpendicular to the plane of propagation. In this case the electric field obeys:

$$\nabla^2 E(\boldsymbol{r}) + k^2 \epsilon(\boldsymbol{r}) E(\boldsymbol{r}) = 0 \tag{4.2}$$

where in this notation, $\nabla = \hat{\boldsymbol{x}}\,\partial/\partial x + \hat{\boldsymbol{y}}\partial/\partial y$, $\boldsymbol{r} = \hat{\boldsymbol{x}}x + \hat{\boldsymbol{y}}y$, and $k = 2\pi/\lambda$ represents the wavenumber in the background medium (of permittivity ϵ_b) and finally $\epsilon(\boldsymbol{r}) = \epsilon_o(\boldsymbol{r})/\epsilon_b$ corresponds to the normalized spatial distribution of the relative permittivity of this object

$\epsilon_o(\boldsymbol{r})$ which is in general a complex quantity. When a dielectric object is illuminated by an arbitrary incoming wave, the total electric field can always be decomposed in terms of an incident $E^{(i)}$ and scattered $E^{(s)}$ component as follows

$$E(\boldsymbol{r}) = E^{(i)}(\boldsymbol{r}) + E^{(s)}(\boldsymbol{r}), \tag{4.3}$$

where the incident field, of-course, satisfies the Helmholtz equation in the background medium $\nabla^2 E^{(i)}(\boldsymbol{r}) + k^2 E^{(i)}(\boldsymbol{r}) = 0$. Therefore the scattered field should satisfy the following equation:

$$\nabla^2 E^{(s)} + k^2 E^{(s)} = -k^2(\epsilon(x,y) - 1)E(\boldsymbol{r}). \tag{4.4}$$

Note that the right hand side is non-zero only inside the scatterer. By using the two-dimensional Green's function of Equation (4.3)

$$\nabla^2 G(\boldsymbol{r} - \boldsymbol{r}') + k^2 G(\boldsymbol{r} - \boldsymbol{r}') = -\delta^{(2)}(\boldsymbol{r} - \boldsymbol{r}') \tag{4.5}$$

which is found to be:

$$G(\boldsymbol{r} - \boldsymbol{r}') = \frac{i}{4} H_0^{(1)}(k|\boldsymbol{r} - \boldsymbol{r}'|), \tag{4.6}$$

one can show that the scattered field can be written in terms of the total field inside the scatterer according to:

$$E^{(s)}(\boldsymbol{r}) = \frac{ik^2}{4} \int (\epsilon(\boldsymbol{r}') - 1) E(\boldsymbol{r}') H_0^{(1)}(k|\boldsymbol{r} - \boldsymbol{r}'|) d^2 r', \tag{4.7}$$

where $H_0^{(1)}$ represents a Hankel function of the first kind and the integral is taken over the entire surface of the scatterer. On the other hand, the total electric field inside the scatterer can be obtained from the following integral equation:

$$E(\boldsymbol{r}) - \frac{ik^2}{4}\int(\epsilon(\boldsymbol{r}') - 1)E(\boldsymbol{r}')H_0^{(1)}(k|\boldsymbol{r} - \boldsymbol{r}'|)d^2r' = E^{(i)}(\boldsymbol{r}). \tag{4.8}$$

In general, for an arbitrary scattering object, Equation (4.6) does not admit an analytical solution. However, it can always be solved numerically by using the method of moments as in ref. [1].

In most scattering problems, the far-field ($kr \gg 1$) scattering pattern is of a particular importance. Here by using the asymptotic form of the Hankel function at the far-field, $H_0^{(1)}(k|\boldsymbol{r} - \boldsymbol{r}'|) \sim \sqrt{\frac{2}{\pi k_0 r}}\exp\left(ikr - ik\hat{\boldsymbol{r}}\cdot\boldsymbol{r}' - i\frac{\pi}{4}\right)$, one can simply show that Equation (4.4) reduces to:

$$E^{(s)}(\boldsymbol{r}) = \frac{k^2(1+i)}{2\sqrt{\pi}}\frac{e^{ikr}}{\sqrt{kr}}\int(\epsilon(\boldsymbol{r}') - 1)E(\boldsymbol{r}')\exp(-ik\hat{\boldsymbol{r}}\cdot\boldsymbol{r}')\,d^2r', \tag{4.9}$$

where $\hat{\boldsymbol{r}}$ denotes a unit vector along the position vector $\boldsymbol{r}$. Therefore, for an incoming plane wave $E^{(i)} = E_0\exp(i\boldsymbol{k}\cdot\boldsymbol{r})$, the far-field scattering behavior can be described via:

$$E = E_0\left(\exp(i\boldsymbol{k}\cdot\boldsymbol{r}) + f(\theta)\frac{e^{ikr}}{\sqrt{kr}}\right), \tag{4.10}$$

where $f(\theta)$ represents the so called scattering amplitude. It is worth noting that the scattering amplitude f also implicitly depends on the direction $\hat{\boldsymbol{k}}$ of the incoming plane wave.

4.2. Light deflection by a PT cylinder

We now turn our attention to a PT-symmetric infinitely long dielectric cylinder, as depicted in Figure 4.1. In this case, the upper half of this system displays gain, $\epsilon_1 = \epsilon_R - i\epsilon_I$, whereas the lower half an equal amount of loss, $\epsilon_2 = \epsilon_R + i\epsilon_I$, $(\epsilon_I > 0)$. The scattering strength is quantified via the following two dimensionless quantities $m_R = k_0 a\epsilon_R = 2\pi\epsilon_R(a/\lambda)$ and $m_I = k_0 a\epsilon_I = 2\pi\epsilon_I(a/\lambda)$.

Figure 4.2 shows the near and far-field scattering pattern arising from such a PT-symmetric cylinder when illuminated by a plane wave along the x direction. According to this figure, in the near field, light is mostly concentrated in the gain side. However, in the far field light tends to bend toward the lossy section. Note that, aside from this deflection, the azimuthal distribution of the scattering amplitude is almost preserved. By further increasing the gain/loss contrast the bending angle increases until reaching a point where the scattering pattern changes drastically and the deflection angle cannot even be defined.

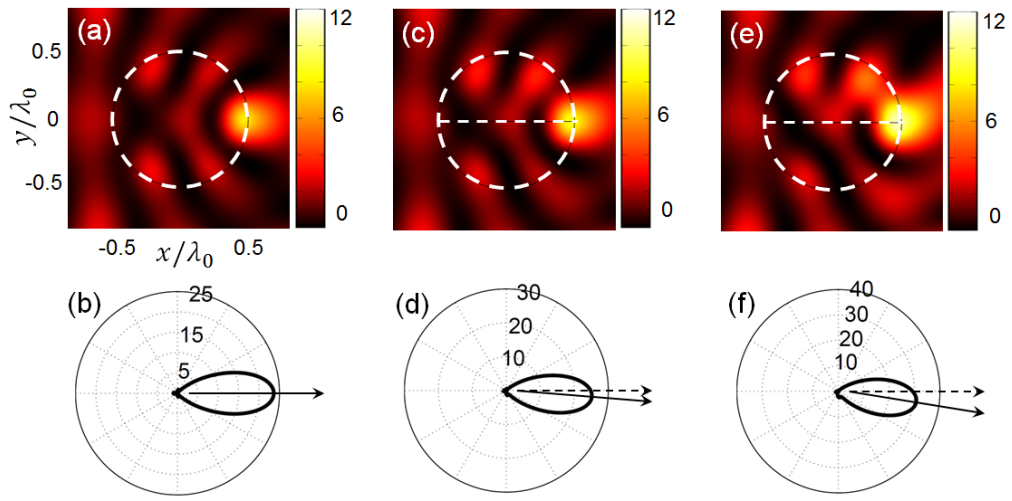

Figure 4.2. (a,b) The near-field pattern of the total electric field intensity ($|E|^2$) and far-filed patterns of the scattered electric field intensity ($|f(\theta)|^2$) for the case of a passive lossless scatterer i.e., $\pm\epsilon_I = 0$, (c,d) near-field and far-field patterns for a PT-symmetric scatterer with $\pm\epsilon_I = \pm 0.2$, (e,f) the same as in the previous case when the imaginary part of permittivity is increased to $\pm\epsilon_I = \pm 0.4$. In all cases $\epsilon_R = 2.1$ and diameter of the cylinder is equal to the wavelength of the incoming plane wave. In the above examples a heavy gain/loss contrast has been used to exemplify these features.

Such deflection of light is an outcome of the local energy flow from the gain toward the loss region which in turn leads to a tilt in the phase front of light while propagating along the gain/loss interface of the PT-symmetric cylinder. Figures 4.3(a,b) depict the Poynting vector $\boldsymbol{S} = (-i/\omega\mu)E(\hat{\boldsymbol{x}}\,\partial/\partial x + \hat{\boldsymbol{y}}\,\partial/\partial y)E^*$ in the near-field of the cylinder which clearly shows the local energy flow at the boundaries of gain/loss regions.

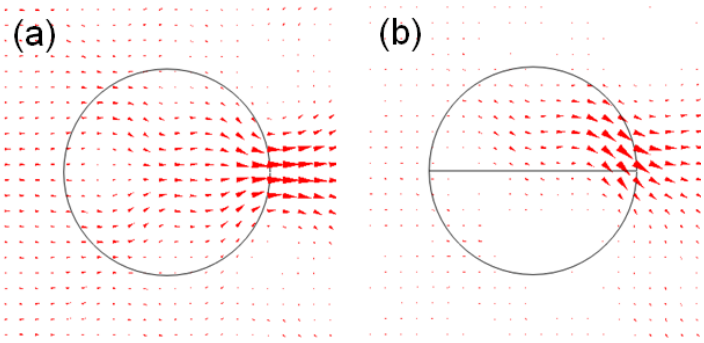

Figure 4.3. (a,b) The Poynting vector associated with the Hermitian and the PT-symmetric cylinders of part (a) and (e) of Figure 4.2 respectively.

According to this discussion, the scattering profile of the PT particle should vary when the angle of the incoming changes with respect to the gain/loss interface. To verify this latter, we performed simulations with different angles of incidence of the incoming plane wave. As illustrated in Figure 4.4, the angle of deflection as well as the maximum scattering amplitude change drastically when the incoming light propagates parallel or normal to the interface.

It is worth noting that, the amount of gain used in the examples of Figure 4.2 might be large and experimentally out of reach.

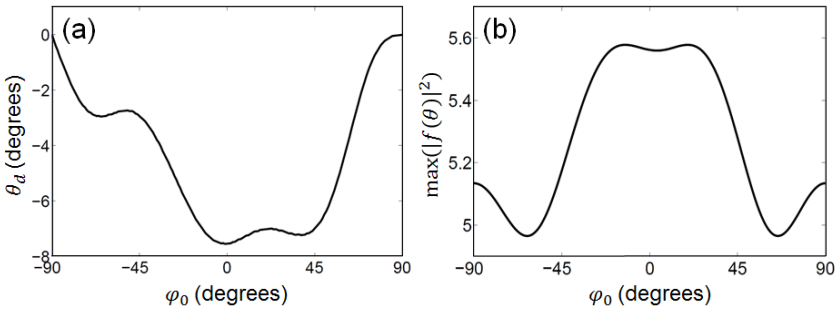

Figure 4.4. The deflection angle (a) and the maximum scattering amplitude (b) for different angles of the incoming plane wave for the example of Figure 4.2.

Of interest would be to see if one can get similar results without exploiting such gain values. For this reason, we consider again the PT cylinder of the previous example while this time the gain region is replaced with a transparent material with the same relative permittivity, i.e., $\epsilon_1 = \epsilon_R$, and $\epsilon_2 = \epsilon_R + i\epsilon_I$. As shown in Figure 4.5, even in the absence of gain, the deflection property is preserved while compared to the PT structure the deflection angle is reduced. This is expected since the deflection depends on the total contrast in the imaginary parts of the two regions rather than the absolute values. Note however that the scattering amplitude is overall reduced and this was expected since there is no net gain to compensate the effect attenuations created in the loss region.

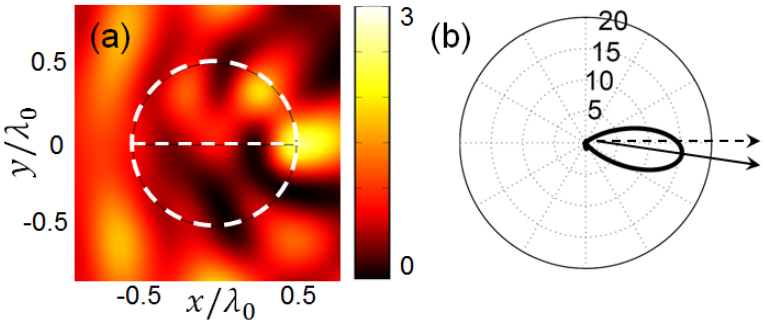

Figure 4.5. Scattering pattern of a PT-like cylinder. The real parts of the relative permittivity in the two regions are the same. While half of such cylinder is transparent (neither gain and nor loss), the other half exhibits loss.

4.3. Modified optical theorem in PT-symmetric structures

According to Figures 4.2, for a transparent dielectric cylinder, maximum scattering amplitude occurs right behind the cylinder. Indeed optical theorem demands that the scattering amplitude right behind a Hermitian scatterer is never zero. Optical theorem is an outcome of the power conservation in Hermitian systems. In such systems it relates the total scattered power to the scattering amplitude right behind the scatterer. For 2D structures and under TE polarization this relation can be stated as $\int_0^{2\pi}|f(\theta)|^2 d\theta = -2\sqrt{\pi}\mathrm{Re}[(1+i)f(0)]$.

Even though in the presence of gain and loss power conservation is lost, as we will show here for PT-symmetric strcutures optical theorem can be modified. To show this, let

us start with Equation (4.2) in the presence of the PT-symmetric relative permittivity of Equations (4.1). Using Equation (4.2) along with its parity and time reversed counterpart one can simply show that $E(\boldsymbol{r})\nabla^2 E^*(-\boldsymbol{r}) - E^*(-\boldsymbol{r})\nabla^2 E(\boldsymbol{r}) = 0$. By integrating this relation over a circle of radius $r \to \infty$ which spans over the entire xy plane, one reaches at $\int_0^{2\pi}\big(E(\boldsymbol{r})\cdot\nabla E^*(-\boldsymbol{r}) - E^*(-\boldsymbol{r})\cdot\nabla E(\boldsymbol{r})\big)\cdot\hat{\boldsymbol{r}}d\theta = 0$. Now, the far-field approximation of E (Eq. (8)) can be used in this relation. By choosing $\boldsymbol{k} = \hat{\boldsymbol{x}}k$, after neglecting terms that decay faster than $(kr)^{-1/2}$, the stationary phase approximation can be used to show:

$$\int_0^{2\pi} f(\theta)f^*(\theta+\pi)d\theta = -2\sqrt{\pi}\mathrm{Re}[(1+i)f(\pi)], \tag{4.11}$$

which is the modified optical theorem for PT-symmetric objects.

4.4. Reciprocity in PT-symmetric structures

Finally in the following we consider reciprocity in PT-symmetric structures. Here we change the notation used for the scattering amplitude from $f(\theta)$ to $f\big(\widehat{\boldsymbol{k}}_1 \to \widehat{\boldsymbol{k}}_2\big)$, where $\widehat{\boldsymbol{k}}_1$ denotes the unit vector along the direction of the incoming wave and $\widehat{\boldsymbol{k}}_2$ a unit vector along an arbitrary direction of scattering. The reciprocity relation can be proved in a similar manner to reference [2]. We assume two solutions of Equation (4.2), E_1 and E_2, that are generated by two plane waves with wavevectors $\boldsymbol{k}_1$ and $-\boldsymbol{k}_2$ respectively. In the far field far-filed these two solutions can be written as

$$E_1 = E_0\left(\exp(+i\boldsymbol{k_1}\cdot\boldsymbol{r}) + f\left(+\widehat{\boldsymbol{k}}_1 \to \widehat{\boldsymbol{k}}\right)\frac{\exp(ikr)}{\sqrt{kr}}\right), \tag{4.12.a}$$

$$E_2 = E_0\left(\exp(-i\boldsymbol{k_2}\cdot\boldsymbol{r}) + f\left(-\widehat{\boldsymbol{k}}_2 \to \widehat{\boldsymbol{k}}\right)\frac{\exp(ikr)}{\sqrt{kr}}\right). \tag{4.12.b}$$

On the other hand note that any two arbitrary solutions of Equation (4.2) satisfy $E_2\nabla^2 E_1 - E_1\nabla^2 E_2 = 0$ which after integrating over a circle of radius $r \to \infty$ leads to $r\int_0^{2\pi}(E_2\nabla E_1 - E_1\nabla E_2)\cdot\hat{\boldsymbol{r}}d\theta = 0$. This is nothing but the Lorentz reciprocity theorem [2]. After inserting solutions of Equations (4.11), into this last relation and using the stationary phase approximation one can show that

$$f\left(\widehat{\boldsymbol{k}}_1 \to \widehat{\boldsymbol{k}}_2\right) = f\left(-\widehat{\boldsymbol{k}}_2 \to -\widehat{\boldsymbol{k}}_1\right) \tag{4.13}$$

It should be noted that Equation (4.12) is not limited to Hermitian or PT-symmetric scatterers. As a matter of fact, this relation is quite general for any arbitrary complex distribution of the relative permittivity as long as it is linear and time invariant. This is because the Lorentz reciprocity theorem as mentioned here is independent of the relative permittivity.

It one-dimensional scattering settings the results of the reciprocity relation is counterintuitive. In such configurations by starting from the Helmholtz equation $\left(d^2/dx^2 + k_0^2\epsilon(x)\right)E(x) = 0$ (for TE polarized light) one can show that two arbitrary solutions E_1 and E_2 satisfy the relation $E_2\, d^2E_1/dx^2 - E_1\, d^2E_2/dx^2 = 0$ which in turn leads to the one-dimensional representation of the Lorentz reciprocity theorem as follows: $E_2\, dE_1/dx - E_1\, dE_2/dx = \text{Const.}$ Now we assume E_1 and E_2 to be the electric fields

generated by two plane waves propagating toward the left and right hand sides respectively therefore:

$$E_1 = \begin{cases} E_0(\exp(+ik_0x) + r_1\exp(-ik_0x)); & x \to -\infty \\ E_0 t_1 \exp(+ik_0x)\,; & x \to +\infty \end{cases} \tag{4.14}$$

and:

$$E_2 = \begin{cases} E_0 t_2 \exp(-ik_0x)\,; & x \to -\infty \\ E_0(\exp(-ik_0x) + r_2\exp(+ik_0x)); & x \to +\infty \end{cases} \tag{4.15}$$

By using these two last relations into the reciprocity relation one can simply show that:

$$t_1 = t_2. \tag{4.16}$$

This simple relation states that the transmission coefficients of the both left- and right-propagating waves are the same. Interestingly nothing can be said about the reflection coefficients of these two waves.

In conclusion, we have studied the scattering properties of PT-symmetric cylinders. We showed that such scatterers can deflect light toward an angle which is controlled via gain/loss contrast. We also investigated two important point regarding the scattering theory of PT-symmetric structures in general; optical theorem and reciprocity. Our results can have potential applications in alignment of micro-particles.

4.5. References

1. J. H. Richmond, "Scattering by a dielectric cylinder of arbitrary cross section shape," IEEE Trans. Antennas Propag. **AP-13**, 334 (1965).

2. M. Born and E. Wolf, "*Principles of Optics: Electromagnetic Theory of Propagation*, *Interference and Diffraction of Light*," Cambridge Univ. Press, (1999).

CHAPTER FIVE: OPTICAL MESH LATTICES

In this section we investigate PT-symmetry in new class of optical lattices, the so called mesh lattices. As we explain later in this section, what makes such lattices a perfect host for realization of PT-symmetric conditions is the fact that coupling between adjacent waveguides of this lattice occurs at discrete positions. And this allows for a physical separation of the coupling and amplification/attenuation segments in a PT lattice [1].

5.1. Hermitian optical mesh lattices

Figure 5.1 illustrates the spatial realization of such a mesh lattice when only passive phase elements are involved. This configuration can be synthesized using an array of waveguides that are periodically and discretely coupled to their next neighbors (at the rectangular regions of Figure 5.1). In addition phase elements can also be inserted. Each phase element introduces at every array site n a phase ϕ_n that happens to be independent of the discrete propagation step m. The location of each phase modulator in the lattice is denoted in the figure by a circle. As we will later demonstrate, these phase modulators effectively play the role of a refractive index profile in spatial arrangements. By exciting only one waveguide, after traveling a certain distance in this waveguide, light couples to the adjacent left (right) channel through a coupler, and after propagating this same distance it then couples to the

adjacent waveguide to its right (left). Indeed light propagation in this system leads to an interference process that is equivalent to a discrete time quantum walk [2].

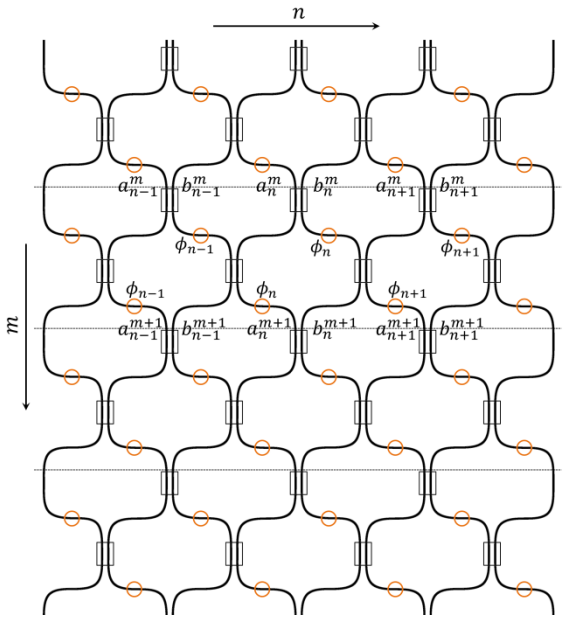

Figure 5.1. An optical mesh lattice; the lattice is composed of an array of waveguides which are periodically coupled together in discrete intervals. Circles indicate the position of phase elements and rectangles the coupling regions. The dashed lines show the discrete points where the field intensity is evaluated before coupling occurs.

As Figure 5.1 clearly indicates, this mesh lattice is di-atomic in nature. Using the simple input/output relation of a 50:50 coupler [3] and by considering the effect of the phase elements, it is straightforward to show that the light evolution equation in this system takes the form:

$$a_n^{m+1} = \frac{e^{i\phi_n}}{2}\left[(a_n^m + ib_n^m) + e^{-i\phi_n}(-a_{n-1}^m + ib_{n-1}^m)\right] \qquad (5.1.a)$$

$$b_n^{m+1} = \frac{e^{i\phi_n}}{2}\left[(b_n^m + ia_n^m) + e^{i\phi_{n+1}}(-b_{n+1}^m + ia_{n+1}^m)\right] \tag{5.1.b}$$

In Equations (5.1), a_n^m and b_n^m represent the field amplitudes at adjacent waveguide sites n (in the n'th column) at a discrete propagation step or distance m (m'th row). It should be noted that in deriving these equations the phase accumulated due to propagation in any waveguide section is ignored. Indeed a waveguide section of length l between two subsequent couplers leads to a phase accumulation of βl, where β is the propagation constant of the guide. Yet, one can readily show that even in the presence of these additional phase terms Equations (5.1) remain the same once a simple gauge transformation is used; $(a_n^m, b_n^m) \rightarrow (a_n^m, b_n^m)e^{i2m\beta l}$.

To establish the necessary periodicity, we assume that the phase elements provide a phase potential that alternates between two different values in n:

$$\phi_n = \begin{cases} +\phi_0; & n \text{ even} \\ -\phi_0; & n \text{ odd} \end{cases} \tag{5.2}$$

This kind of phase potential has a translational symmetry $\phi_{n+2} = \phi_n$ which leads to a transverse periodicity in this "four-atom" lattice with a fundamental period of $N = 2$ where each cell is diatomic. In addition the lattice is now periodic in both n and m.

5.1.1. The band structure

First we study the band structure of this mesh system. Once the band characteristics and corresponding Bloch modes are known, the dynamic properties of the system can then be extrapolated. To find the dispersion relation of this lattice we consider discrete "plane wave solutions" of the form $e^{iQn}e^{i\theta m}$ where Q represents a Bloch momentum in the transverse direction and θ plays the role of a propagation constant. To obtain the corresponding band structure we assume solutions of the form

$$\begin{pmatrix} a_n^m \\ b_n^m \end{pmatrix} = \begin{pmatrix} A_n \\ B_n \end{pmatrix} e^{iQn}e^{i\theta m} \tag{5.3}$$

where A_n and B_n are periodic Bloch functions with the period of $N = 2$, ie. $A_{n+2} = A_n$ and $B_{n+2} = B_n$. In general, for $n = 2j$, we use $A_n, B_n = A_0, B_0$ while for $n = 2j + 1$ we employ $A_n, B_n = A_1, B_1$. This comes from the fact that a unit cell of this periodic structure includes two discrete positions n.

By inserting Equations (5.3) in (5.1), and by adopting the phase potential of Equation (5.2), we obtain the following dispersion relation after expanding the corresponding 4×4 determinant of a unit cell:

$$\cos(2Q) = 8\cos^2(\theta) - 8\cos(\phi_0)\cos(\theta) + 4\cos^2(\phi_0) - 3 \tag{5.4}$$

As expected from the double periodicity of this system in both n and m the band structure is also periodic in both Q and θ having fundamental periods of 2π and π respectively. This represents a major departure from optical waveguide arrays where the propagation

dimension is a continuous variable. Under the assumption of Equation (5.2), this mesh arrangement exhibits four primary bands which are periodic with respect to the two Bloch momenta. Figure 5.2 depicts the band structure of this mesh lattice when $\phi_0 = 0.2\pi$.

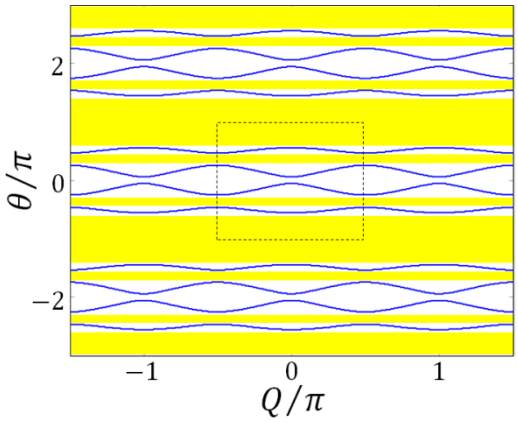

Figure 5.2. Band structure of the optical mesh lattice in the presence of periodic step-like potential created from phases, alternating between $-\phi_0$ and ϕ_0 where $\phi_0 = 0.2\pi$. The shaded area shows the band gap regions and the dotted boundary depicts the primary Brillouin zone of this lattice.

Equation (5.4) is valid in general for any arbitrary choice of ϕ_0. However it should be noticed that in the special case where $\phi_0 = 0$ (empty lattice) this relation becomes degenerate. Indeed for the empty lattice the periodicity of this diatomic lattice is $N = 1$ and hence its Brillouin zone involves two bands and lies in the domain between $-\pi$ and π for $-\pi < \theta < \pi$. The folded version of this Brillouin zone (corresponding to the empty lattice) is shown in Figure 5.4 (a) where the two bands are degenerately folded into four. Figures 5.4(b,c,d) depict the band structure of this mesh lattice for three nonzero values of ϕ_0

within the Brillouin zone as a function of the Bloch momenta, i.e., $-\pi/2 < Q < \pi/2$ and $-\pi < \theta < \pi$. Again the shaded areas show the associated band gaps. According to Figure 5.3, a nonzero ϕ_0 lifts the degeneracy and leads indeed to four bands.

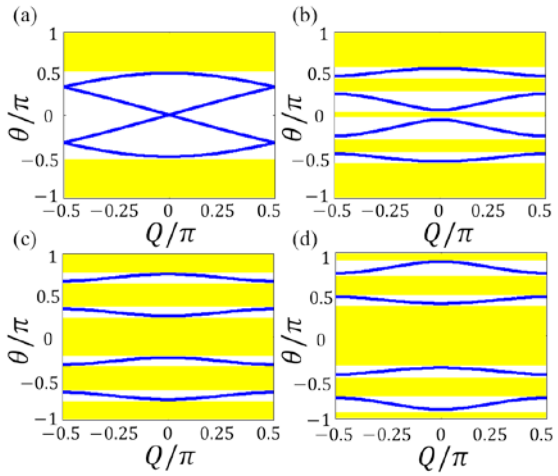

Figure 5.3. Band structure of an optical mesh lattice for several cases; (a) Lattice without any phase potential $\phi_0 = 0$ (empty lattice), (b) Lattice with a symmetric phase step-like potential varying between $-\phi_0$ and ϕ_0 when $\phi_0 = 0.2\,\pi$, (c) same as in (b) but with $\phi_0 = 0.5\,\pi$, (d) $\phi_0 = 0.7\,\pi$. For case (a) the reduced Brillouin zone is depicted while for the rest the first Brillouin zone is shown in its entirety.

According to Equation (5.4) and as one can see from the figures the band structure has a reflection symmetry around $Q = 0$ and $\theta = 0$. For any finite ϕ_0 there are four bands in the Brillouin zone, all having a zero slope at the center ($Q = 0$) and at the edges ($Q = \pm\pi/2$). For the empty lattice on the other hand, in reality there are two bands and the slope is zero at the center ($Q = 0$) of the top band while it is non-zero at the two edges ($Q = \pm\pi/2$) and

at $Q = \theta = 0$ where the bands collide and there is no band gap between them. The addition of the phase potential $\pm\phi_0$ to the empty lattice breaks this degeneracy and creates band gaps at these points. This breaking of the degeneracy becomes clear by comparing Figures 5.4 (a) and (b). Equation (5.4) can also be written in a more explicit form as a function of Q:

$$\theta = \pm \cos^{-1}\left[\frac{1}{2}\left(\cos(\phi_0) \pm \sqrt{\cos^2(Q) + \sin^2(\phi_0)}\right)\right] \tag{5.5}$$

where in this relation any combination of the two plus/minus signs corresponds to each of the four bands.

Before ending this discussion, it is worth noting that this phase potential does not need to be symmetrized in a $\pm\phi_0$ fashion as done before in this section. In fact any periodic potential that is alternating in n between two different phase values will break the degeneracy of an empty lattice, thus creating four bands in the first Brillouin zone. For example let us consider a phase potential that varies between 0 and $2\phi_0$ in n:

$$\phi(n) = \begin{cases} 2\phi_0; & n \text{ even} \\ 0; & n \text{ odd} \end{cases} \tag{5.6}$$

Note that this latter phase potential has the same strength as the one used before. In this latter case, by using the same ansatz of Equation (5.3) we directly obtain the dispersion relation corresponding to the new potential of Equation (5.6).

$$\cos\big(2(Q + \phi_0)\big) = 8\cos^2(\theta - \phi_0) - 8\cos(\phi_0)\cos(\theta - \phi_0) + 4\cos^2(\phi_0) - 3 \tag{5.7}$$

A close examination of Equation (5.7) reveals that this latter dispersion curve is identical to that of Equation (5.4), apart from a phase shift in both θ and Q. More specifically Q has

shifted by an amount of $-\phi_0$ while θ by ϕ_0. Figure 5.4 shows a plot of this dispersion relation for $\phi_0 = 0.2\pi$. The shift of origin (compared to Figure 5.3(b)) is evident in this figure.

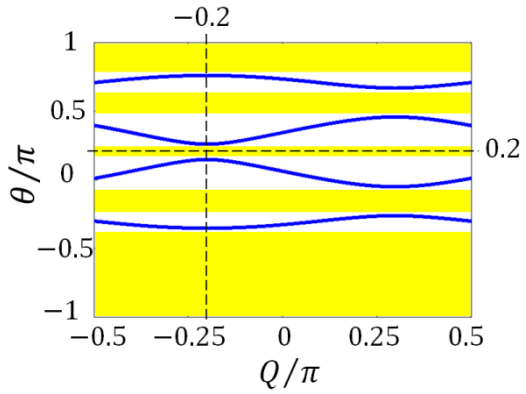

Figure 5.4. Band structure of an optical mesh lattice with a non-symmetric step-like phase potential alternating between 0 and $2\phi_0$ while $\phi_0 = 0.2\pi$. Compared to the case of a symmetric phase potential (Fig. 4(b)) the band structure is shifted from the center.

In the rest of this work we consider for simplicity symmetric phase potentials for which the band structure is symmetric around $Q = \theta = 0$.

5.1.2. Beam dynamics

Here, we investigate optical dynamics in passive mesh lattices. The impulse response of the system is of particular importance since is known to excite the entire band structure. For

this reason only one of the waveguide elements is excited at $m = 0$. In what follows, the impulse response will be studied by using $a_0^0 = 1$with all the other elements in the array initially set to zero.

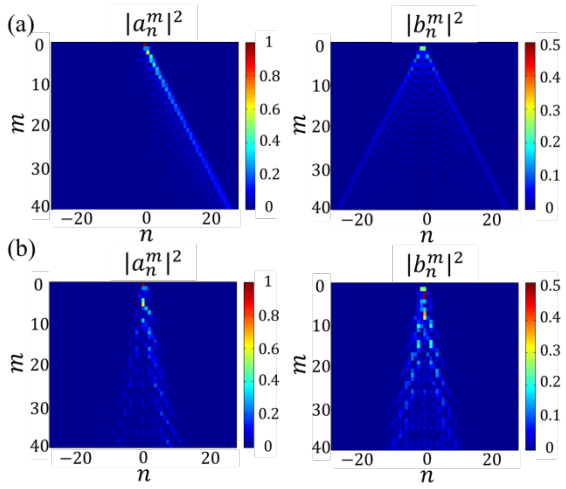

Figure 5.5. Impulse response of a mesh lattice where the intensity profile of a_n^m and b_n^m is plotted; (a) $\phi_0 = 0$ (empty lattice), (b) $\phi_0 = 0.4\pi$. In both cases $a_0^0 = 1$ and all other elements are initially set to zero.

Figure 5.5(a) shows the impulse response of this array lattice when $\phi_0 = 0$ and $a_0^0 = 1$. According to this figure light transport in this system exhibits upon spreading a highest slope of $\Omega_{max} = \pm 1/\sqrt{2}$ with respect to the longitudinal axis. As we will see this result will be formally justified by considering the group velocity in this arrangement. The impulse response of the mesh lattice in the presence of a periodic phase potential with $\phi_0 = 0.4\pi$ is also plotted in Figure 5.5(b) when this time $b_0^0 = 1$. In this last case, it becomes clearly apparent that the maximum speed of the excitation spreading becomes slower when ϕ_0

increases. As in waveguide arrays [4], the impulse response can be viewed as a "ballistic" transport across the array.

The band structure can also provide useful information concerning the evolution of more complicated initial excitations like localized wavepackets. More specifically, we consider initial distributions of a_n^0 and b_n^0 of the form $f_n e^{iQ_0 n}$ where f_n is a slowly varying envelope function (with a narrow spatial spectrum) and $e^{iQ_0 n}$ is a rapidly varying phase term signifying the central Bloch momentum Q_0 of this wavepacket. Therefore the propagation process of this discrete beam excitation can be effectively treated through a Fourier superposition of the Floquet-Bloch modes $e^{iQn}e^{i\theta m}$ assumed before to analyze this system. In this regard, both the group velocity and the dispersion broadening of this wavepacket can be obtained by expanding the propagation constant θ in a Taylor series around Q_0, that is:

$$\theta = \theta_0 + \frac{d\theta}{dQ}\Big|_{Q_0}(Q - Q_0) + \frac{d^2\theta}{dQ^2}\Big|_{Q_0}(Q - Q_0)^2 \tag{5.8}$$

As in continuous lattices, the tangent of the beam angle (or "group velocity") is associated with the term:

$$\Omega = \frac{d\theta}{dQ}\Big|_{Q_0} \tag{5.9}$$

Using the dispersion Equation (5.4), this group speed can then be written as:

$$\frac{d\theta}{dQ} = \frac{1}{4}\frac{\sin(2Q)}{[\sin(2\theta) - \cos(\phi_0)\sin(\theta)]} \tag{5.10}$$

where in this relation θ could be replaced from the dispersion relation of Equation 5.5 to obtain the right hand side as a function of Q and the band under consideration. Using similar arguments, the discrete diffraction factor can be obtained from:

$$D = \frac{d^2\theta}{dQ^2}\Big|_{Q_0} \tag{5.11}$$

Figure 5.6 depicts the beam angle Ω for several lattices with different amplitudes of the phase potential, ϕ_0. According to this figure, in an empty lattice ($\phi_0 = 0$) this beam angle is zero at the center ($Q = 0$) and it is maximum at $Q = \theta = 0$ in the folded Brillouin zone scheme where to first order the dispersion relation dictates that $Q = \pm\sqrt{2}\theta$. Hence, as previously indicated, the maximum slope expected in this configuration is $\Omega_{\max} = \pm 1/\sqrt{2}$. On the other hand for a lattice having a periodic phase potential, each band exhibits a zero group velocity at the center and at the edges ($Q = \pm\pi/2$) of the zone while the maximum happens somewhere in between. For the special case of $\phi_0 = \pi/2$ the bands are translated in θ and hence in groups of two have identical group velocity curves, and as shown in Figure 5.6(c) they lie on top of each other.

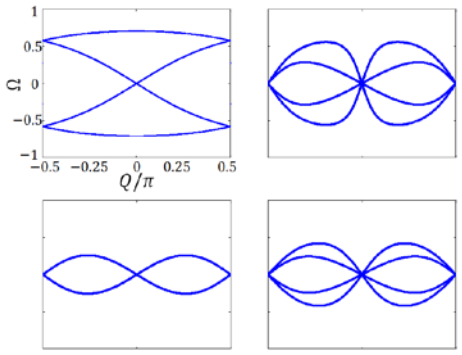

Figure 5.6. Beam tangent angle (Ω) for several cases; (a) empty lattice (note that in this case the curve is folded to the reduced Brillouin zone), (b) for a lattice in the presence of periodic phase potential with $\phi_0 = 0.2\pi$, (c) $\phi_0 = 0.5\pi$, (d) $\phi_0 = 0.7\pi$.

To demonstrate some these transport effects, let us consider for example the evolution of a Gaussian wavepacket having the following initial profile:

$$a_n^0 = e^{-(n/\Delta)^2} e^{iQ_0 n} \tag{5.12}$$

where 2Δ represents the Gaussian beamwidth and Q_0 designates the initial tilt in its phase front or central Bloch momentum. In this case the same input profile is assumed for b_n^0 in order to symmetrize the dynamics. Figure 5.7 shows the propagation dynamics of this Gaussian beam in this mesh lattice. Here the lattice involves a periodic phase potential with $\phi_0 = 0.2\pi$. The Gaussian beam width 2Δ is large enough to avoid the diffraction effects and in addition $Q_0 = 0.25\pi$. According to this figure four independent beams (of the same width) result from this initial excitation, each emanating from a corresponding band, and propagating in different directions. To elucidate these results, the band structure is also

plotted in this same Figure 5.7(c) where the arrows perpendicular to the bands indicate the propagation direction of each of these four beams.

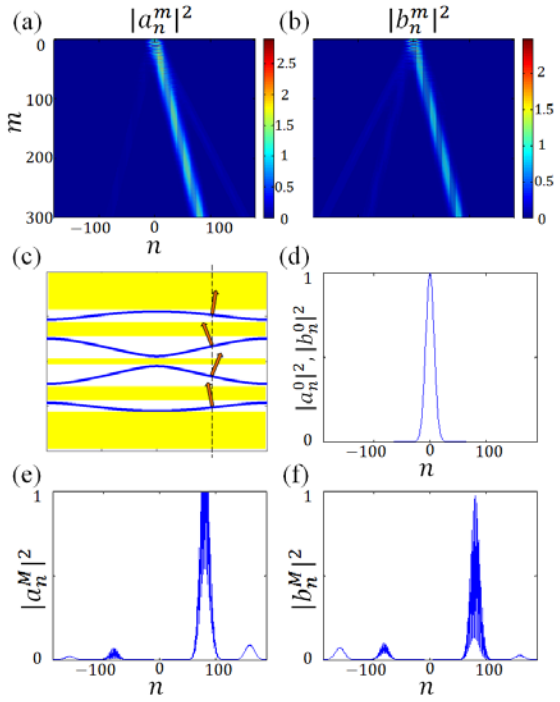

Figure 5.7. Gaussian wavepacket propagating in a mesh lattice. The beam has a width of $2\Delta = 30$ and an initial phase tilt of $Q_0 = 0.25\pi$. The lattice has a phase potential of $\phi_0 = 0.2\pi$ (a) intensity $|a_n^m|^2$, (b) intensity of $|b_n^m|^2$, (c) band structure of the lattice with the dashed line crossing the band at four points at $Q_0 = 0.25\pi$ and the arrows show the propagation direction of the four resulting beams, (d) intensity profile of the initial Gaussian beam, (e) a_n^M intensity profile of a_n^m at the last discrete longitudinal step (here $M = 300$), (e) b_n^M.

Finally in order to investigate diffraction effects in passive mesh systems, we consider the propagation properties of a relatively narrow Gaussian wavepacket. Figure 5.8 depicts the propagation dynamics of a Gaussian beam with a width of $2\Delta = 8$ in a lattice with $\phi_0 = 0.5\pi$. The figures compare the beam propagation for two different values of Q_0, 0 and 0.25π. According to this figure when $Q_0 = 0$, the beam has a very low transverse velocity and experiences a considerable degree of diffraction. As shown in the other panels, when the beam is launched at the dispersion free point of the band ($Q_0 = 0.25\pi$) where $D = 0$ and the transverse group velocity is maximum.

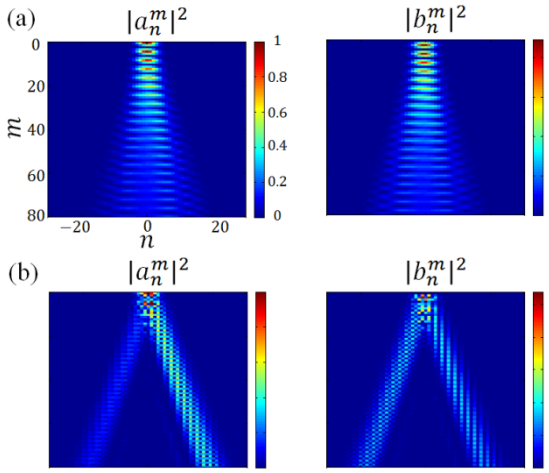

Figure 5.8. Diffraction properties of a Gaussian beam in a mesh lattice with $\phi_0 = 0.5\pi$. The Gaussian beam has a width of $2\Delta = 8$ while the initial phase tilt is: (a) $Q_0 = 0$, (b) $Q_0 = 0.25\pi$.

According to Figure 5.3 this selection of ϕ_0 leads to four bands. Figure 5.8(a) depicts Gaussian beanm spreading at $Q_0 = 0$ and at the same time interference effects resulting

from the excitation of multiple bands. On the other hand for $Q_0 = 0.25\pi$ two Gaussian beams symmetrically emerge with two different propagation speeds. Yet, the interference pattern in each of the two branches demonstrates that all four bands are actually in play in these dynamics. Notice however that at this point little beam spreading occur since for these parameters $D = 0$.

5.2. PT-symmetric optical mesh lattices

After understanding the Hermitian case, in this section we turn our attention to the PT symmetric mesh lattices.

5.2.1. PT synthetic coupler

Before exploring a large-scale PT-symmetric mesh lattice, it is worth analyzing the elemental building block involved in such a network. Figure 5.9 (a) shows a PT-symmetric coupler where the gain and loss is uniformly distributed along the two arms, a structure similar to that considered in previous experimental studies [5,6]. Figure 5.9 (b), on the other hand, depicts a passive coupler where the gain and loss mechanisms are separately inserted in the two arms only. Here we show that this new type of a PT-symmetric coupler

displays exactly the same behavior and characteristics of a standard PT-coupler arrangement considered before.

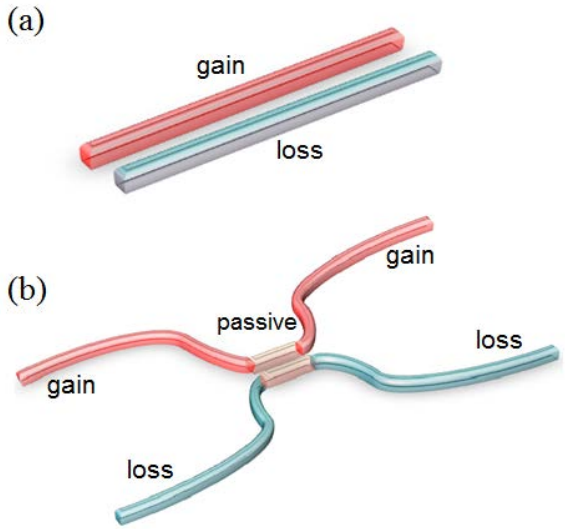

Figure 5.9. A distributed PT-symmetric coupler and a PT-synthetic coupler; (a) The PT-coupler is composed of two similar dielectric waveguides coupled to each other, with one experiencing gain (red) while the other an equal amount of loss (blue), (b) A PT-synthetic coupler is composed of a passive coupler while the gain and loss waveguides are separately used in the arms.

In Figure 5.9(b) we assume a 50:50 passive directional coupler connected to two arms, one providing amplification (red) while the other an equal amount of loss (blue). We assume that each arm delivers an amplification or attenuation of $e^{\pm\gamma/2}$ right before and after the coupler. Hence the modal amplitudes a' and b' at the output of this system, are related to those at the input ports, a and b, in the following way:

$$\binom{a'}{b'} = \begin{pmatrix} e^{\gamma/2} & 0 \\ 0 & e^{-\gamma/2} \end{pmatrix} \frac{1}{\sqrt{2}} \begin{pmatrix} 1 & i \\ i & 1 \end{pmatrix} \begin{pmatrix} e^{\gamma/2} & 0 \\ 0 & e^{-\gamma/2} \end{pmatrix} \binom{a}{b} \tag{5.13}$$

in which case

$$\binom{a'}{b'} = \frac{1}{\sqrt{2}} \begin{pmatrix} e^{\gamma} & i \\ i & e^{-\gamma} \end{pmatrix} \binom{a}{b} \tag{5.14}$$

where a and b represent optical amplitudes in the gain and loss channes respectively. The two supermodes and their respective eigenvalues of this system can be readily found. Depending on the amount of gain/loss in the system two regimes can be distinguished; if $\gamma < \cosh^{-1}(\sqrt{2})$ this PT system is operating below the PT-symmetry breaking threshold and its supermodes are given by:

$$\binom{a_0}{b_0} = \begin{pmatrix} 1 \\ \pm \exp(\pm i\eta) \end{pmatrix} \exp(\pm i\omega) \tag{5.15}$$

where $\cos(\omega) = \frac{1}{\sqrt{2}}\cosh(\gamma)$ and $\sin(\omega) = \frac{1}{\sqrt{2}}\cos(\eta)$. Thus for $\gamma < \cosh^{-1}(\sqrt{2})$ the two modes repeat themselves after passing through this discrete sytem exept from a trivial phase shift of $\pm\omega$. On the other hand if $\gamma > \cosh^{-1}(\sqrt{2})$ the system operates above the PT-symmetry breaking threshold and:

$$\binom{a_0}{b_0} = \begin{pmatrix} 1 \\ i \exp(\mp\eta) \end{pmatrix} \exp(\pm\omega) \tag{5.16}$$

where $\cosh(\omega) = \frac{1}{\sqrt{2}}\cosh(\gamma)$ and $\sinh(\omega) = \frac{1}{\sqrt{2}}\sinh(\eta)$. Interstingly this same behavior is displayed by a standard PT-symmetric coupler where the gain and loss is continuously distributed. Finally at exactly the PT-symmetry breaking threshold $\gamma = \cosh^{-1}(\sqrt{2})$ the two supermodes collapse to one and thus:

$$\begin{pmatrix} a_0 \\ b_0 \end{pmatrix} = \begin{pmatrix} 1 \\ i \end{pmatrix} \tag{5.17}$$

which clearly shows the existence of a phase difference of $\pi/2$ between the two waveguides.

It is worth noting that this arrangment has certain advantages over a standard distributed PT-symmetric coupler. First of all it is experimentally easier to achieve the delicate balance required for PT symmetry. In addition the coupling and amplification/attenuation process take place in two separate steps so there are no physical restrictions imposed by the Kramers-Kronig relations. As previously mentioned, these effects have so far hindered progress in implementing large-scale PT-symmetric networks, since they limit the possibility of achieving the required values for gain/loss and refractive index, all at the same time.

5.2.2. The band structure of PT mesh lattices

Figure 5.10 shows a PT-symmetric mesh lattice made of PT-synthetic couplers, identical to that of Fig. 2.9 (b). In addition phase elements are inserted in this same lattice (shown by circles in Fig. 2.10(a)) in order to provide the needed real part in the potential function. In Fig. 2.10(b) the distributions of phase modulation and that of gain/loss are plotted as a function of the discrete position n - clearly satisfying the requirement for PT-symmetry, i.e. an even distribution for the phase and an odd distribution for the gain/loss profile in n. In fact a comparison with continuous systems suggests that the phase and gain/loss discrete

elements play the role of the real and imaginary parts in the refractive index respectively. By considering an amlification/attenuation factor of $e^{\pm\gamma/2}$ in each waveguide section between two subsequent couplers, then one can show that light propagation in this PT-synthetic mesh network is governed by the following discrete evolution equations:

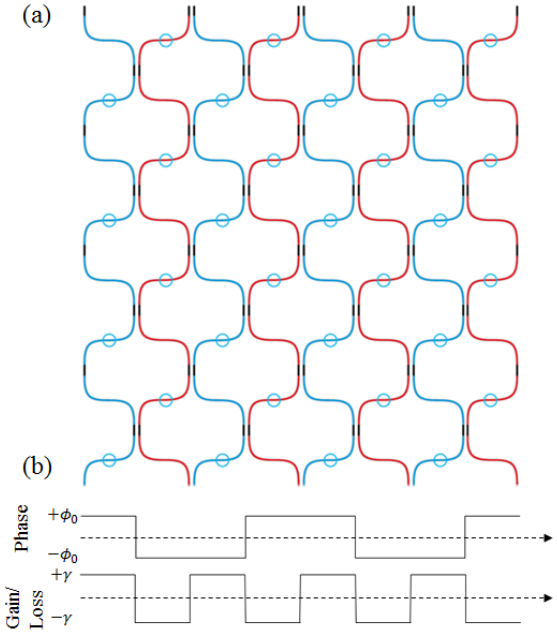

Figure 5.10. (a) A PT-synthetic mesh lattice, (b) transverse distribution of the phase potential (symmetric) and gain/loss (antisymmetric).

$$a_n^{m+1} = \frac{e^{i\phi_n}}{2}\left[e^{-\gamma}(a_n^m + ib_n^m) + e^{-i\phi_n}(-a_{n-1}^m + ib_{n-1}^m)\right], \tag{5.18.a}$$

$$b_n^{m+1} = \frac{e^{i\phi_n}}{2}\left[e^{+\gamma}(b_n^m + ia_n^m) + e^{i\phi_{n+1}}(-b_{n+1}^m + ia_{n+1}^m)\right]. \tag{5.18.b}$$

To understand the behavior of this system, the band structure should be first determined. By adopting the same ansatz of Equations (5.3), one can derive the following dispersion relation for this PT lattice:

$$\cos(2Q) = 8\cos^2(\theta) - 8\cosh(\gamma)\cos(\phi_0)\cos(\theta) + 4\cos^2(\phi_0) - 4 + \cosh(2\gamma) \quad (5.19)$$

Figure 5.11 shows the band structure of this system for several different values of the phase potential amplitude ϕ_0 and gain/loss coefficients γ. In each case the real parts of the propagation constant (θ) is plotted in blue while the imaginary parts are shown in red.

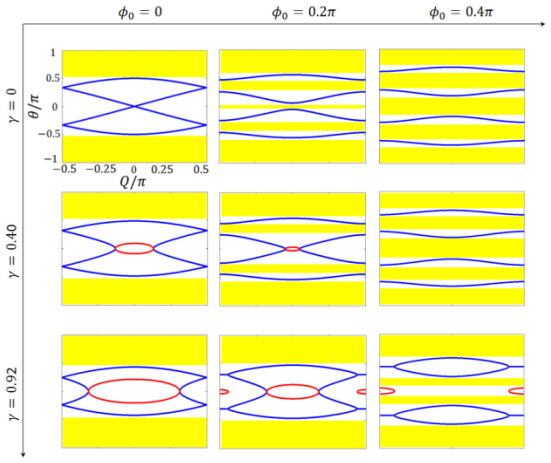

Figure 5.11. Band structure of PT-synthetic mesh lattice for several values of ϕ_0 and γ. In these plots the real part of propagation constant, θ is indicated in blue, while the imaginary part in red.

As it is illustrated in this figure, the presence of a symmetric phase potential in this system tends to pull apart the bands thus creating a band gap, while the antisymmetric gain/loss tends instead to close the gap. The system is said to be operating below the PT-symmetry

breaking threshold as long as the eigenvalues associated with all bands are real. However at a critical amount of gain/loss the bands merge at the so called exceptional points, and for even higher gain/loss values, sections with conjugate imaginary eigenvalues appear in the bands.

In what follows, we consider the case where ϕ_0 is fixed and discuss how the band structure will change by gradually increasing the gain/loss coefficient γ. Analysis shows, that for a given value of ϕ_0, the first band merging occurs at two different positions; if $0 < \phi_0 < \pi/4$, the bands merge at $Q = \theta = 0$ and the second band gap remains open till reaching the a critical value of gain/loss coefficient γ. For even higher gain/loss values the system finds itself in the broken phase regime. For $\pi/4 < \phi_0 < \pi/2$ on the other hand all bands are open till a critical point. Exactly at this threshold, the band gap at the edges of the Brillouin zone at $Q = \pm\pi/2$ closes while the first band gap remains open till reaching another critical point where it eventually evaporates. Based on this observations analytical results for the symmetry breaking point can be obtained. We first consider the case where $0 < \phi_0 < \pi/4$. In this case, as γ increases, we expect that for a fixed ϕ_0, the symmetry breaking will occur at $Q = \theta = 0$. Therefore Eq. 19 can be rewritten as:

$$\cosh^2(\gamma) - 4\cos(\phi_0)\cosh(\gamma) + 2\cos^2(\phi_0) + 1 = 0. \tag{5.20}$$

From here one can easily show that this critical $\gamma$is given by:

$$\gamma = \cosh^{-1}\left(2\cos(\phi_0) - \sqrt{\cos(2\phi_0)}\right). \tag{5.21}$$

This relation dictates the merging condition for the first two bands and is only valid for $0 < \phi_0 < \pi/4$, consistent with our previous observations. To find the corresponding relation for the band merging occurring at the edges, in Equation (5.19) we set $= \pi/2$, which in turn leads to a second order algebraic equation in $\cos(\theta)$. Since we expect that the two eigenvalues will collapse into one (exceptional point), one may use this degeneracy condition in Equation (5.19) at $Q = \pi/2$. After setting the discriminant of the quadratic equation to zero one finds that:

$$\gamma = \cosh^{-1}\left(\sqrt{2}\right) \approx 0.8814 \tag{5.22}$$

This last relation provides the PT-threshold for band merging at the edges of the Brillouin zone and is independent of ϕ_0. Interestingly this same value $\gamma = \cosh^{-1}\left(\sqrt{2}\right)$coincides with the critical PT-thresold of the basic unit involved in this lattice, as found in previous section.

Figure 5.12 depicts the PT-symmetry breaking threshold in the parameter space of ϕ_0 and γ. The area below the curve corresponds to the case where the system operates in the exact PT phase where all the eigenvalues are real. On the curve symmetry breaking occurs and above this line the spectrum is in general complex. The top flat line of this curve corrsponds to the critical value of 0.8814 while the part between $0 < \phi_0 < \pi/4$ can be obtained from Equation (5.21). The other segement symmetrically folows.

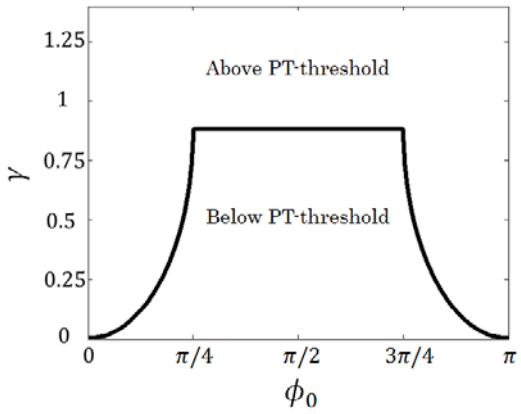

Figure 5.12. PT-symmetry breaking threshold curve in a two dimensional parameter space of ϕ_0 and γ. The region below the curve corresponds to the exact PT-phase while the region above the curve designates the domain where PT symmetry is broken.

5.2.3. Beam dynamics in PT-symmetric mesh lattices

To dynamically explore the symmetry breaking threshold, the impulse response of system is studied. Since the impulse is expected to excite the entire band of this mesh lattice, one should expect that an exponential growth in the total energy of the system should be observed once the PT-symmetry is broken.

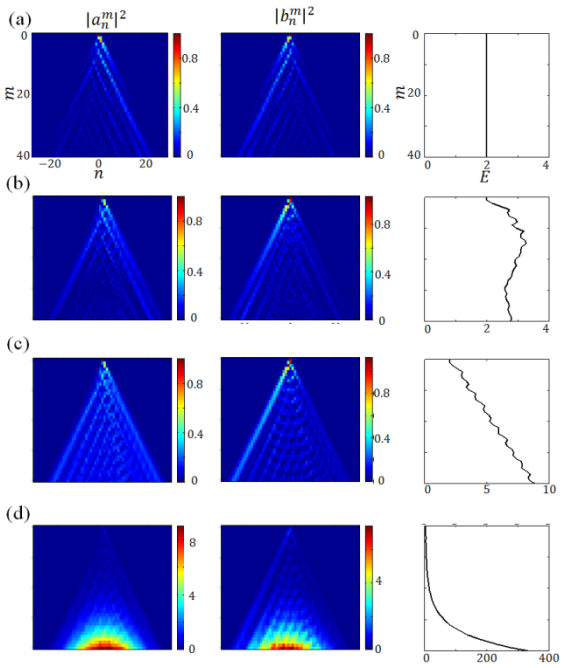

Figure 5.13. Impulse response of the PT-symmetric lattice with a periodic phase potential of $\phi_0 = 0.2\pi$ while several different amounts of gain/loss are considered; (a) $\gamma = 0$ (the passive lattice), (b) $\gamma = 0.3$ (below threshold), (c) $\gamma = 0.35$ (at threshold), (d) $\gamma = 0.4$ (above threshold)

Figure 5.13 shows the impulse response ($a_n^0 = 1$, while all other elements are initially zero) of a PT-symmetric mesh lattice for several different values of gain/loss γ when $\phi_0 = 0.2\pi$. This range covers the passive scenario, or the case where the system operates below, at, and above the PT-symmetry breaking threshold. The total energy in the system $E_m = \sum_n |a_n^m|^2 + |b_n^m|^2$, is also plotted in each case at each discrete step of propagation, m in Figure 5.13. While for the passive system ($\gamma = 0$) the total energy remains constant during propagation, for a PT-symmetric lattice used below its threshold the total energy

tends to oscillate during propagation –but always remains below a certain bound. Note that such power oscillations were previously encountered in other PT-symmetric periodic structures. At exactly the PT-threshold a linear growth in energy is observed (see Figure 5.13(c)). Finally above thereshold an exponential growth in energy is observed as expected from a system involving complex eigenvalues (Figure 5.13(d)).

To further explore the behavior of this PT-synthetic mesh lattice, we use at the input a Gaussian wavepacket, as in Equation (5.12). Indeed by exciting this system with a wide input beam (that has a narrow spectrum) one can selectively excite different sections of the band structure. We now consider a PT-symmetric mesh lattice with a periodic phase potential of amplitude $\phi_0 = 0.2\pi$ and a gain/loss factor of $\gamma = 0.4$. The band sturucture corresponding to this structure is plotted in Fig. 5.11.

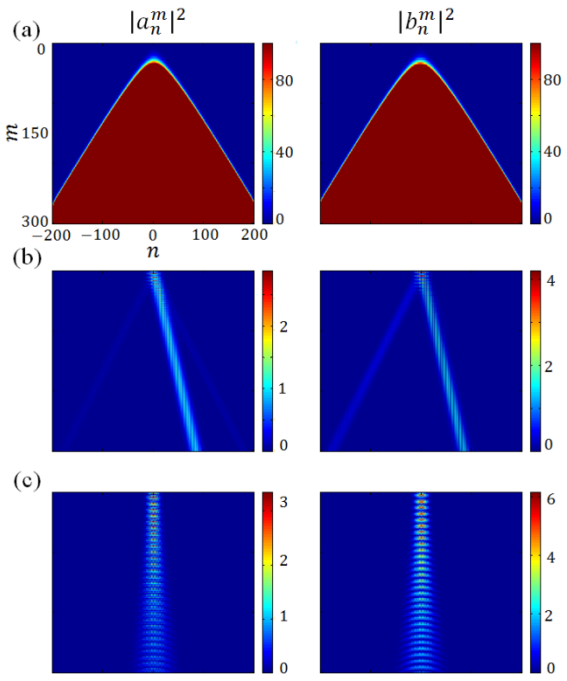

Figure 5.14. Gaussian beam propagation in a PT-symmetric lattice operating in the broken PT phase regime. The lattice has a periodic phase potential of amplitude $\phi_0 = 0.2\pi$ and a gain/loss factor of 0.4. The Gaussian beam has a width of $2\Delta = 30$ and is launched with three different values of initial phase tilt; (a) $Q_0 = 0$, (b) $Q_0 = 0.25\pi$, (c) $Q_0 = 0.5\pi$. In (a) the intensities are only shown up to a level of 100.

Figure 5.14 depicts the propagation of a Gaussian wavepacket in this lattice, when launched with a Bloch momentum Q_0. Three different valus for Q_0 have been selected for this example: $Q_0 = 0$, 0.25π and 0.5π. According to Figure 5.14 while for the first case an exponential energy growth is observed, for the other two cases energy remains essentially bounded. These results reveal that even above the PT-symmetry breaking threshold, non-

growing/decaying modes can be excited in such systems. This all depends on which section of the band structure is excited by the initial conditions.

Compared to a passive mesh lattice, the band structure of its PT-symmetric counterpart reveals another intersting property. As previously discussed, the maximum beam transport angle (Ω_{max}) in an empty lattice is $1/\sqrt{2}$, and even in the presence of a periodic phase potential this angle is always less than this maximum transverse velocity. However according to the Figure 5.11, when approaching the exceptional points from the real section (blue part) of the band, its slope tends to considerably increase and eventually approaches exceedingly around the exceptional points.

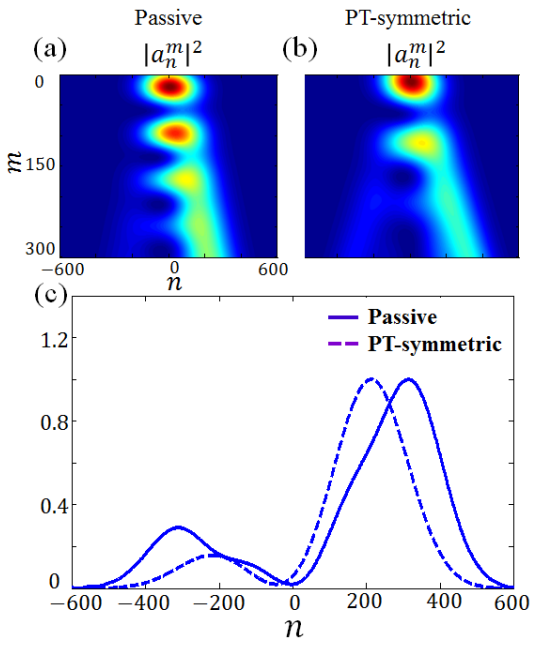

Figure 5.15. A broad Gaussian beam propagating in a passive and a PT-symmetric lattice; (a) evolution of the Gaussian beam in a passive empty lattice, (b) in a PT-symmetric lattice, (c) normalized intensity profiles of the beam at the last propagation step (m=300) in both lattices. The parameters of the PT lattice are $\gamma = 0.039$ and $\phi_0 = 0$. The Gaussian beam has a beam width of $2\Delta = 400$ and an initial phase front tilt of $Q_0 = 0.9817\pi$.

Figure 5.15 compares the propagation a Gaussian beam in a passive and a PT-symmetric mesh lattice operating above threshold. Both lattices are excited with the same Gaussian beam having a Bloch momentum Q_0, which is chosen such that is close to that corresponding to the exceptional point of the PT-symmetric lattice. Close to the exceptional point, the slope of the band structure tends to infinity and therefore, the associated group velocity can become almost arbitarily high for any narrow-bandwith wave packet. While

the maximum beam angle in passive empty lattice is ~0.7 (which is close to the maximum) for the PT-symmetric lattice this angle is approximately 1.04 which is certainly above the maximum limit of the passive lattice. This effect has in fact a counterpart in continuous media. As previously shown, in the presence of a gain medium [7,8] and in PT-symmetric gratings and lattices [9] used close to the exceptional points, the group velocity of light can be superluminal. It should be noted however that none of these effects violates causality since non-causal waveforms are used for excitation.

5.3. References

1. M.-A. Miri, A. Regensburger, U. Peschel, and D. N. Christodoulides, "Optical mesh lattices with PT symmetry," Phys. Rev. A **86**, 023807 (2012).

2. Y. Aharonov, L. Davidovich, and N. Zagury, "Quantum random walks," Phys. Rev. A **48**, 1687 (1993).

3. A. Yariv, Optical Electronics in Modern Communications (Oxford University, New York, 1997).

4. D. N. Christodoulides, F. Lederer, and Y. Silberberg, "Discretizing light behaviour in linear and nonlinear waveguide lattices," Nature (London), **424**, 817 (2003).

5. Guo, G. J. Salamo, D. Duchesne, R. Morandotti, M. Volatier-Ravat, V. Aimez, G. A. Siviloglou, and D. N. Christodoulides, "Observation of PT-symmetry breaking in complex optical potentials," Phys. Rev. Lett. **103**, 093902 (2009).

6. E. Rüter, K. G. Makris, R. El-Ganainy, D. N. Christodoulides, M. Segev, and D. Kip, "Observation of parity-time symmetry in optics," Nat. Phys. **6**, 192 (2010).

7. R. Chiao, "Superluminal (but causal) propagation of wave-packets in transparent media with inverted atomic populations," Phys. Rev. A **48**, R34 (1993).

8. L. J. Wang, A. Kuzmich and A. Dogariu, “Gain-assisted superluminal light propagation,” Nature **406**, 277 (2000).

9. A. Szameit, M. C. Rechtsman, O. Bahat-Treidel, M. Segev, “PT-symmetry in honeycomb photonic lattices,” Phys. Rev. A **84**, 021806(R) (2011).

CHAPTER SIX: PT-SYMMETRY IN NONLINEAR SYSTEMS

In this chapter we find an analytical solution for a nonlinear PT-symmetric grating. It has been known for long time that nonlinear gratings can support a special class of soliton solutions-the so called Bragg solitons [1-3]. Unlike optical solitons propagating in nonlinear dispersive fibers, this family of waves is made possible by nonlinearly interlocking both the forward and backward propagating modes. Here we study behavior of this same family in the presence of an anti-symmetric gain/loss modulation [4].

6.1. Nonlinear PT-symmetric gratings

To begin our work by considering a PT-symmetric optical grating having the following periodic complex refractive index distribution: with let us consider a fiber with the following refractive index of the core:

$$n = n_0 + n_{1R}\cos\left(\frac{2\pi}{\Lambda}z\right) + in_{1I}\sin\left(\frac{2\pi}{\Lambda}z\right) + n_2|E|^2 \tag{6.1}$$

In this profile the first term stands for the refractive index background of the material involved while the three other terms are considered to be small perturbations on n_0; the second term describes periodic Bragg grating, the third term represents the superimposed

complex PT potential (gain or loss) and the last term accounts for the Kerr nonlinearity. We now express the solution as a sum of forward and backward propagating waves:

$$E = E_f(z,t)\exp[i(\beta_0 z - \omega_0 t)] + E_b(z,t)\exp[-i(\beta_0 z + \omega_0 t)] \tag{6.2}$$

where $\omega_0 = 2\pi c/\lambda_0$ is the carrier angular frequency, λ_0 is the free space wavelength and $\beta_0 = n_0\omega_0/c$ is the unperturbed propagation constant. Finally $E_f(z,t)$ and $E_b(z,t)$ represent slowly varying amplitudes for the forward and backward waves respectively. In this case, it can be directly shown that the two slowly varying envelope functions satisfy the following coupled wave equations:

$$+i\left(\frac{\partial E_f}{\partial z} + \frac{1}{v}\frac{\partial E_f}{\partial t}\right) + (\kappa + g)e^{-i2\delta z}E_b + \gamma\left(\left|E_f\right|^2 + 2|E_b|^2\right)E_f = 0, \tag{6.3.a}$$

$$-i\left(\frac{\partial E_b}{\partial z} - \frac{1}{v}\frac{\partial E_b}{\partial t}\right) + (\kappa - g)e^{+i2\delta z}E_f + \gamma\left(|E_b|^2 + 2\left|E_f\right|^2\right)E_b = 0. \tag{6.3.b}$$

In the above equations $v = c/n_0$ is the wave velocity in the background material, $\kappa = \pi n_{1R}/\lambda_0$ is the coupling coefficient arising from the real Bragg grating itself, and $g = \pi n_{1I}/\lambda_0$ is the anti-symmetric coupling coefficient arising from complex PT potential term. In addition, $\delta = (n_0/c)(\omega_0 - \omega_B)$ is a measure of detuning from the Bragg angular frequency $\omega_B = \pi c/(n_0\Lambda)$ and $\gamma = n_2\omega_0/c$ is the self-phase modulation constant.

In the linear regime, the properties of Equations (6.3) can be readily understood by using the following gauge transformation, $E_f = Fe^{-i\delta z}e^{iv\delta t}$, $E_b = Be^{i\delta z}e^{iv\delta t}$, in which case one obtains:

$$+i\left(\frac{\partial F}{\partial z} + \frac{1}{v}\frac{\partial F}{\partial t}\right) + (\kappa + g)B = 0, \tag{6.4.a}$$

$$-i\left(\frac{\partial B}{\partial z}-\frac{1}{v}\frac{\partial B}{\partial t}\right)+(\kappa-g)F=0. \tag{6.4.b}$$

By assuming time harmonic solutions of the form, $(F,B)=(F_0,B_0)\exp\big(i(Kz-\Omega t)\big)$ we arrive at the dispersion relation:

$$K^2=\frac{\Omega^2}{v^2}-(\kappa^2-g^2). \tag{6.5}$$

The effect of the PT-symmetric term arising from g on the overall dispersion characteristics of this Bragg grating is obvious. In essence, its presence can effectively shift the photonic band gap as illustrated in Figure 6.1, for different ratios of g/κ.

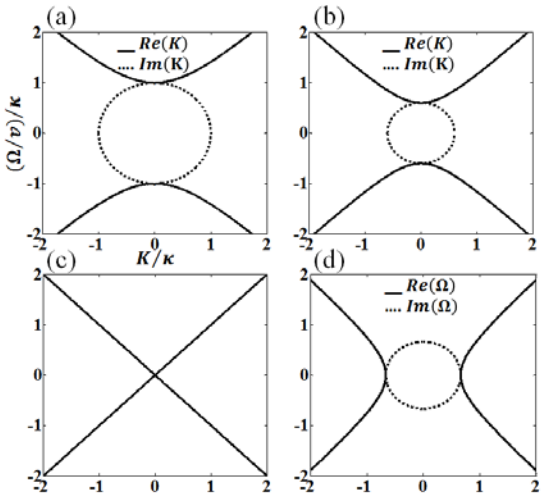

Figure 6.1. Band structure of a PT-symmetric periodic grating (linear case) for different ratios of g/κ; (a) 0, (b) 0.8, (c) 1, and (d) 1.2.

In Figure 6.1, the dispersion properties of this periodic PT grating are depicted for three different regimes, depending on the ratio of g/κ; (a) for $g\leq\kappa$ (below PT-symmetry

breaking threshold) the band structure has essentially the shape of an ordinary Bragg grating-with the photonic band gap reduced, (b) for $g = \kappa$ (at the PT threshold or exceptional point) the band gap is closed and the dispersion curve is identical to that expected from the homogeneous background material, and (c) for $g \geq \kappa$ (above threshold) where no band gap exists and the dispersion relation is totally different in shape. As Figure 6.1(d) illustrates, above the PT-symmetry breaking threshold, around the origin, there is always a range of wavevectors associated with complex frequencies. As we will see, this latter observation explains why in this case field configurations can grow/decay exponentially with propagation distance. In addition, in this same regime the group velocity is always larger than velocity of light within the background material. In this work, we mainly restrict our attention in the first range, i.e., we will assume that the PT grating will be operated below the PT threshold where the entire frequency spectrum is real.

6.2. PT Bragg solitons: Mathematical model

In this section we investigate the existence of solitary wave solutions for the coupled wave equations (6.3). To do so, we exploit the existing similarity between Equations (6.3) and of that of the massive Thirring model [5]. By introducing the two parameters $\rho = \sqrt{(\kappa - g)/(\kappa + g)}$ and $\kappa_\rho = \sqrt{\kappa^2 - g^2}$ and by employing the gauge transformations $E_f = Fe^{-i\delta z}e^{iv\delta t}$, $E_b = \rho Be^{i\delta z}e^{iv\delta t}$, these coupled wave equations can be written in the following form:

$$+i\left(\frac{\partial F}{\partial z}+\frac{1}{v}\frac{\partial F}{\partial t}\right)+\kappa_\rho B+\gamma(|F|^2+2\rho^2|B|^2)F=0 \tag{6.6.a}$$

$$-i\left(\frac{\partial B}{\partial z}-\frac{1}{v}\frac{\partial B}{\partial t}\right)+\kappa_\rho F+\gamma(\rho^2|B|^2+2|F|^2)B=0 \tag{6.6.b}$$

We note that the above mentioned gauge transformation is only valid when $\kappa > g$, e.g. below the PT threshold point. As a next step we consider a solution of the form:

$$(F,B)=\alpha\left(\psi_f,\psi_b\right)e^{i\eta(z,t)} \tag{6.7}$$

where the constant α and the function $\eta(z,t)$ remain to be determined. On the other hand, $\left(\psi_f,\psi_b\right)$ represent solutions to the Thirring model [5]:

$$\psi_f=+\sqrt{\frac{\kappa_\rho}{2\gamma}}\frac{1}{\Delta}\sin(\sigma)\,e^{i\Phi}\,\mathrm{sech}\left(\theta-i\frac{\sigma}{2}\right) \tag{6.8.a}$$

$$\psi_b=-\sqrt{\frac{\kappa_\rho}{2\gamma}}\Delta\,sin(\sigma)\,e^{i\Phi}\,sech\left(\theta+i\frac{\sigma}{2}\right) \tag{6.8.b}$$

where σ and θ are functions of z and t defined as follows:

$$\theta=\kappa_\rho\sin(\sigma)\frac{z-vmt}{\sqrt{1-m^2}} \tag{6.9}$$

$$\Phi=\kappa_\rho\cos(\sigma)\frac{mz-vt}{\sqrt{1-m^2}} \tag{6.10}$$

In the above, the dimensionless quantity m is defined as $m=(1-\Delta^4)/(1+\Delta^4)$ and finally Δ and σ $(0<\sigma<\pi)$ are free parameters. After inserting these solutions into equations (3.9) we then obtain:

$$\frac{d\eta}{d\theta}=+\left(\frac{1}{2}\frac{\alpha^2}{\Delta^4}+\rho^2\alpha^2-1\right)\sin(\sigma)\,|\,\mathrm{sech}\left(\theta-i\frac{\sigma}{2}\right)|^2 \tag{6.11.a}$$

$$\frac{d\eta}{d\theta} = -\left(\frac{1}{2}\alpha^2\rho^2\Delta^4 + \alpha^2 - 1\right)\sin(\sigma)\,|\,\mathrm{sech}\left(\theta - i\frac{\sigma}{2}\right)|^2 \tag{6.11.b}$$

A valid solution of Equation (6.11) requires that both sides are equal. This condition in turn determines the unknown coefficient α:

$$\alpha = \left(\frac{1+\rho^2}{2} + \frac{1+\rho^2\Delta^8}{4\Delta^4}\right)^{-\frac{1}{2}} \tag{6.12}$$

Finally η can then be obtained by integrating either one of Equations (6.11):

$$\eta(\theta) = 2\left(\frac{\alpha^2}{2\Delta^4} + \rho^2\alpha^2 - 1\right)\tan^{-1}\left(\tanh(\theta)\tan\left(\frac{\sigma}{2}\right)\right) \tag{6.13}$$

Here it is worth discussing the velocity and instantaneous frequency associated with this soliton solution. According to Equations (6.8) and (6.9) the soliton velocity can be readily obtained from:

$$v_s = \frac{(1-\Delta^4)}{(1+\Delta^4)}v \tag{6.14}$$

Hence the soliton velocity can reach any value between zero ($\Delta = 1$) and the group velocity in the background medium ($\Delta = 0$). Using an amplitude and phase representation of Eqs. (6.7) and (6.8), the corresponding phase of this soliton solutions could be written as,

$$\Xi = \eta + \Phi \pm \tan^{-1}\left(\tanh(\theta)\tan\left(\frac{\sigma}{2}\right)\right) \tag{6.15}$$

where the plus and minus signs correspond to the forward F and backward component B respectively. Note that these phases are obtained after the aforementioned gauge transformation. Hence to obtain the actual phases for the forward and backward waves

(E_f, E_b) the term $v\delta t \mp \delta z$ must be added to these phases respectively. The instantaneous angular frequency can then be obtained from a first order term Taylor series expansion of the respective phase of Equation (6.15):

$$\Omega_s = \frac{\kappa_\rho v}{\sqrt{1-m^2}}\left(\cos(\sigma) + m\left(\frac{\alpha^2}{2\Delta^4} + \rho^2\alpha^2 - 1 \pm 0.5\right)\sin^2(\sigma)\right) \tag{6.16}$$

Given that a gauge transformation was used, the quantity $v\delta$ must be subtracted from the result of Equation (6.16), which is measured with respect to the Bragg frequency. Thus the total instantaneous angular frequency of this soliton solution is given by $\omega_s = \Omega_s - v\delta + \omega_B$. According to the linear dispersion analysis used in the previous section, the frequency band gap for the PT-symmetric grating can be obtained from $-\kappa_\rho v < \Omega < \kappa_\rho v$. Therefore, based on Equation (6.16) the soliton frequency Ω_s may or may not lie in the band gap.

Up to this point, the solutions were obtained for $\kappa > g$, i.e., before the PT symmetry is broken. On the other hand, at exactly the PT-symmetry breaking point ($\kappa = g$), the effective coupling coefficient κ_ρ goes to zero. In this case, the evolution equations are not completely decoupled and can be more effectively treated in the original set of variables. By introducing the gauge transformations $E_f = Fe^{-i\delta z}e^{iv\delta t}$, $E_b = Be^{i\delta z}e^{iv\delta t}$, the coupled wave equations (6.3) reduce to:

$$+i\left(\frac{\partial F}{\partial z} + \frac{1}{v}\frac{\partial F}{\partial t}\right) + 2\kappa B + \gamma(|F|^2 + 2|B|^2)F = 0, \tag{6.17.a}$$

$$-i\left(\frac{\partial B}{\partial z} - \frac{1}{v}\frac{\partial B}{\partial t}\right) + \gamma(|B|^2 + 2|F|^2)B = 0. \tag{6.17.b}$$

The linear coupling term between the forward and backward waves now breaks the symmetry in the evolution equations. Note that there is no energy transfer from the forward wave to the backward but the backward wave facilitates energy transfer to the forward. This can be better understood by considering the general solution of Equation 6.17(b), given by:

$$B = b(y)\, exp\left(-i\gamma\left[b^2(y)x + 2\int_0^x |F|^2 d\xi\right]\right) \tag{6.18}$$

where $x = z - vt$, $y = z + vt$ are forward and backward propagation coordinates and b is an arbitrary function. On the other hand Equations (6.17) admit a trivial solution when $B = 0$. In this latter case, Equation 6.17 (a) reduces to that describing a forward propagating wave in the presence of nonlinear self-phase modulation, which admits the following solution:

$$F = f(x)\exp(i\gamma f^2(x)y) \tag{6.19}$$

where f is an arbitrary function. In the other words, in this regime the intensity profile of the forward propagating wave remains invariant during propagation while no energy is transferred to the backward mode.

6.3. PT Bragg solitons: Simulations

In what follows we exemplify our results through numerical simulations of Equations (6.6). The numerical methods used for solving the coupled wave equations presented are based on finite difference methods using different discretizing approaches in order to account for numerical stability. Here for discretization we use Euler's method that is based on a first order approximation for both temporal and spatial derivatives. In this case stability would not be an issue as long as the temporal step size is way smaller than the spatial step size.

First we investigate the behavior of the solitary wave solution given by Equations (6.7-6.13). Figure 6.2 depicts the corresponding propagation dynamics of this solution for both the forward and backward waves. According to this figure, these two components propagate at a common velocity and they have the same profile.

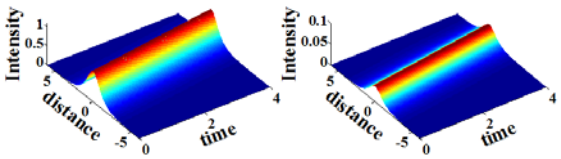

Figure 6.2. Propagation dynamics of a solitary wave solution in a PT-symmetric Bragg structure; intensity evolution for both the forward (left) and backward waves (right) during propagation.

In this numerical example $g/\kappa = 0.8$, and the space-time coordinates are normalized as follows: $Z = \kappa z$ and $T = \kappa v t$. In addition the forward and backward electric fields are also here normalized with respect the quantity $E_0 = \sqrt{\kappa/\gamma}$. The parameter σ that determines the beam width of these solitons is taken to be $\pi/2$, and parameter Δ that determines the common velocity of the two constituent waves is taken to be 0.8. In this figure the total energy of each component that is proportional to $\int_{-\infty}^{\infty} |H(z,t)|^2 dz$ (where H is either a forward or a backward wave) is plotted as a function of time. In the case of PT-symmetric soliton solutions this quantity is constant with propagation.

Figures 6.3 and 6.4 on the other hand show the evolution of a Gaussian pulse when it excites only the forward wave within such a PT-symmetric Bragg grating, for three different cases: below the PT-symmetry breaking point and at threshold. In these simulations g/κ is set to be 0.8 and 1 respectively.

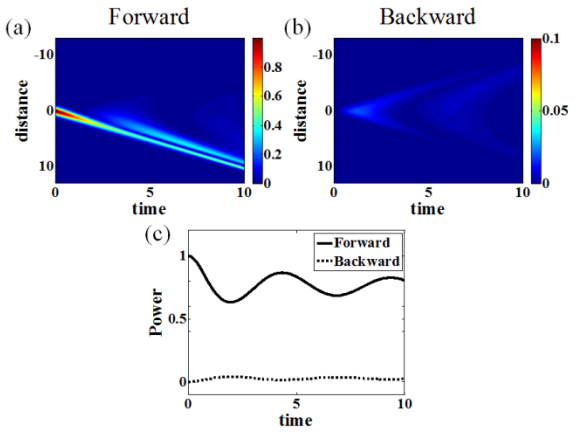

Figure 6.3. Propagation dynamics of a Gaussian wavepacket when injected only in the forward direction when the PT grating is operated below the PT-symmetry breaking threshold. Parts (a) and (b) depict the forward and backward components respectively, and (c) the associated energy as a function of normalized time.

According to Figure 6.3, below PT threshold there is an oscillatory power exchange between the forward and backward waves. In this same regime, by increasing the amplitude of the imaginary potential (amplitude of gain or loss), then the rate of this energy exchange decreases.

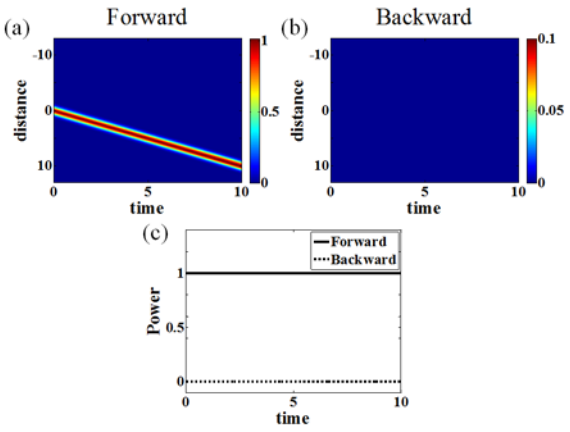

Figure 6.4. The same as Figure (6.3) when the PT grating is operated at the PT-symmetry breaking threshold. Parts (a) and (b) depict the forward and backward components respectively and (c) the associated energy as a function of normalized time.

Figure 6.4 shows that the forward Gaussian wave remains unchanged during propagation while the backward wave is not excited at all. This is in agreement with our previous discussion, as expected from equation (6.19). This is because there is no energy coupling between the forward and backward wave.

6.4. References

1. W. Chen and D. L. Mills, "Gap solitons and the nonlinear optical response of superlattices," Phys. Rev. Lett. **58**, 160 (1987).

2. D. N. Christodoulides and R. I. Joseph, "Slow Bragg solitons in nonlinear periodic structures," Phys. Rev. Lett. **62**, 1746 (1989).

3. A.B. Aceves and S. Wabnitz, Phys. Lett. A, “Self-induced transparency solitons in nonlinear refractive periodic media,” **141**, 37 (1989).

4. M.-A. Miri, A. B. Aceves, T. Kottos, V. Kovanis, and D. N. Christodoulides, “Bragg solitons in nonlinear PT-symmetric periodic potentials,” Phys. Rev. A **86**, 033801(2012).

5. W. E. Thirring, “A soluble relativistic field theory,” Ann. Phys. **3**, 91 (1958).

CHAPTER SEVEN: SUPERSYMMETRY IN OPTICS

Supersymmetry (SUSY) emerged within quantum field theory as a means to relate fermions and bosons [1–6]. In this mathematical framework, these seemingly very different entities constitute superpartners and can be treated on equal footing. Transitions between their respective states require transformations between commuting and anticommuting coordinates—better known as supersymmetries. The development of SUSY was also meant to resolve questions left unanswered by the standard model [7], such as the origin of mass scales or the nature of vacuum energy, and to ultimately link quantum field theory with cosmology towards a grand unified theory. Moreover, SUSY has found numerous applications in random matrix theory and disordered systems [8]. Even though the experimental validation of SUSY is still an ongoing issue, some of its fundamental concepts have been successfully adapted to nonrelativistic quantum mechanics. Interestingly, in this context, SUSY has led to new methods in relating Hamiltonians with similar spectra. In this regard, it has been used to identify new families of analytically solvable potentials and to enable powerful approximation schemes [9–12]. SUSY schemes have been also theoretically explored in quantum cascade lasers [13,14] and ion-trap arrangements [15].

In this chapter we show how the mathematical formalism of the supersymmetric quantum mechanics can be used to establish a peculiar relation between two optical structures [16]. In this manner we show that for any given one-dimensional structure a superpartner can be constructed. Such superpartner can share interesting properties with

the original structure even though it is different in shape. This formalism can be applied to optical guided wave settings as well as scatterers. Each case is discussed in greater details in the next two chapters.

7.1. SUSY operators

Assume the general eigenvalue equation $\mathcal{L}\mathrm{X} = \Omega\mathrm{X}$ for two different operators $\mathcal{L}^{(1)}$ and $\mathcal{L}^{(2)}$:

$$\mathcal{L}^{(1)}X^{(1)} = \Omega^{(1)}X^{(1)}, \tag{7.1.a}$$

$$\mathcal{L}^{(2)}X^{(2)} = \Omega^{(2)}X^{(2)}. \tag{7.1.b}$$

An interesting question arises as to whether two different operators $\mathcal{L}^{(1)} \neq \mathcal{L}^{(2)}$ can have the exact same eigenvalue spectra $\Omega^{(1)} = \Omega^{(2)}$. This classical problem has been addressed in different areas of physics and mathematics. In linear algebra, for example, the answer can be found through the concept of similar matrices. In the framework of linear differential operators, on the other hand, similar questions are addressed in inverse scattering theories. However, supersymmetry is known to offer a simple and straightforward answer to this problem, although its equivalence to the previous methods has been proved in many occasions.

Assume that the first operator can be factorized in terms of two operators A and B as

$$\mathcal{L}^{(1)} = \mathcal{B}\mathcal{A}. \tag{7.2}$$

Then it is straightforward to show that the second operator (superpartner) defined as

$$\mathcal{L}^{(2)} = \mathcal{A}\mathcal{B}, \tag{7.3}$$

can share its entire spectra with the original operator. To show this, consider again Equation (7.1.a) based on relation (7.2) $\mathcal{B}\mathcal{A}X^{(1)} = \Omega^{(1)}X^{(1)}$. Now by multiplying both sides by $\mathcal{B}$ from the left this relation becomes $\mathcal{A}\mathcal{B}\mathcal{A}X^{(1)} = \Omega^{(1)}\mathcal{A}X^{(1)}$ which based on Equation (7.3) reduces to $\mathcal{L}^{(2)}\mathcal{A}X^{(1)} = \Omega^{(1)}\mathcal{A}X^{(1)}$. Comparing this with Equation (7.1.b) simply results in the following relation between the eigenvalues:

$$\Omega^{(2)} = \Omega^{(1)}. \tag{7.4}$$

and for eigenstates:

$$X^{(2)} \propto \mathcal{A}X^{(1)}. \tag{7.5}$$

Similarly one can also show that:

$$X^{(1)} \propto \mathcal{B}X^{(2)}, \tag{7.6}$$

where, in these two last relations a normalization factor is required to maintain the equality. Consider now the case where the operator $\mathcal{A}$ annihilates the fundamental eigenstate (associated with the largest eigenvalue) of the first operator $\mathcal{L}^{(1)}$. In addition to Equations (7.2) and (7.3) supersymmetry also demands that $\mathcal{A}$ annihilates the ground state of $\mathcal{L}^{(1)}$. In this case, the corresponding eigenvalue is then removed from the spectrum of $\mathcal{L}^{(2)}$ while according to Equation (7.4) all the other eigenvalues are the same for both

operators. If on the other hand, $\mathcal{A}$ does not annihilate the ground state of $\mathcal{L}^{(1)}$, then the two operators share the exact same spectrum, and supersymmetry is said to be broken. These two scenarios are schematically shown in Figure 7.1.

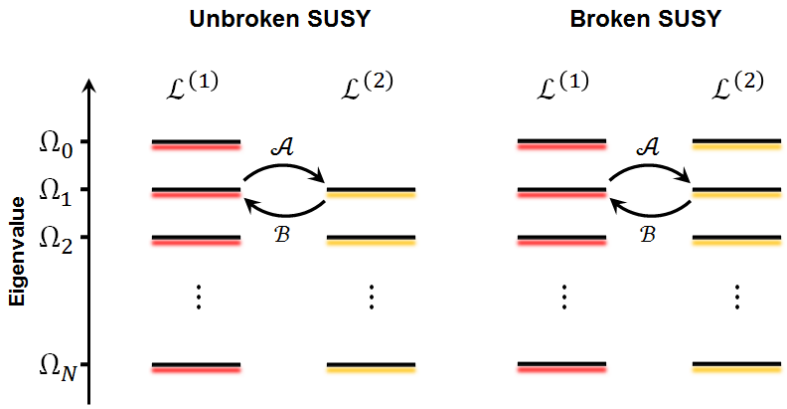

Figure 7.1. The eigenvalue spectrum of two superpartner operators in (a) unbroken and (b) broken supersymmetry regimes.

After this general introduction about supersymmetric linear operators, we now turn our attention to the case of differential operators in one-dimensional optical structures.

7.2. SUSY formalism in paraxial regime

Here we show how the formalism of supersymmetry can be applied to one-dimensional optical structures governed by the paraxial wave equations. This formalism is then generalized beyond the paraxial approximations for both TE and TM polarizations in the

next two sections. Let us consider an index landscape $n(x) = n_0 + \Delta n(x)$ in the transverse coordinate x, where the index modulation $\Delta n(x)$ is assumed to be weak compared to the background index n_0, $\Delta n(x) \ll n_0$. Under these conditions one finds that the slowly varying envelope U of the electric field component $E(x,z) = U(x,z)e^{ik_0 n_0 z}$ satisfies the following evolution equation:

$$i\frac{\partial U}{\partial Z} + \frac{\partial^2 U}{\partial X^2} + V(X)U = 0. \tag{7.7}$$

Here the normalized transverse and longitudinal coordinates are respectively given by $X = x/x_0$ and $Z = z/(2k_0 n_0 x_0^2)$, where x_0 is an arbitrary length scale, and $k_0 = 2\pi/\lambda_0$ is the wave number corresponding to the free space wavelength λ_0. The optical potential $V(X)$ is directly proportional to the refractive index variation,

$$V = 2k_0^2 n_0 x_0^2 \Delta n. \tag{7.8}$$

Looking for stationary (modal) solutions of the form $U(X,Z) = \psi(X) \cdot e^{i\mu Z}$, we then obtain the following Schrödinger eigenvalue problem:

$$\mathcal{H}\psi = \mu\psi, \tag{7.9}$$

where the operator $\mathcal{H} = \frac{d^2}{dX^2} + V(X)$ represents the Hamiltonian of the optical configuration and μ the respective eigenvalue. The resulting Hamiltonian can be factorized as

$$\mathcal{H} = \frac{d^2}{dX^2} + V(X) = \mathcal{B}\mathcal{A} + \alpha, \tag{7.10}$$

and, on the other hand, a superpartner Hamiltonian can be defined as:

$$\mathcal{H}_p = \frac{d^2}{dX^2} + V_p(X) = \mathcal{A}\mathcal{B} + \alpha. \tag{7.11}$$

Here α is a constant to be discussed later and the intervening operators $\mathcal{A}$ and $\mathcal{B}$ are defined as first order differential operators as follows:

$$\mathcal{A} = \frac{d}{dX} + W, \tag{7.12.a}$$

$$\mathcal{B} = \frac{d}{dX} - W. \tag{7.12.b}$$

where the unknown function $W(X)$ is the so-called superpotential. Note that $\mathcal{B} = -\mathcal{A}^\dagger$ where "†" represents the Hermitian conjugate. According to Equations (7.11-13), the original optical potential and its suerpartner can be written in terms of the superpotential W as follows:

$$V = +W' - W^2 + \alpha, \tag{7.13.a}$$

$$V_p = -W' - W^2 + \alpha. \tag{7.13.b}$$

We note that two options for choosing α exist: (a) Assuming that the structure supports at least one bound state, one may opt to set α equal to the fundamental mode's eigenvalue, i.e., $\alpha = \mu_0$. (b) The other possibility is to choose $\alpha > \mu_0$, irrespective of whether the system supports bound states or not. The first case corresponds to an unbroken SUSY where the two potentials share the guided wave eigenvalue spectra, except for that of the fundamental mode, which does not have a corresponding state in the partner. In the second

case, however, SUSY is broken, and the two arrangements share an identical eigenvalue spectrum, including that of the fundamental mode.

It is worth noting that by knowing a given optical potential $V(X)$, and by choosing the parameter α one can always solve the nonlinear Riccati equation (7.14.a) for $W(X)$ numerically. This is of course doable in unbroken and broken supersymmetry regimes. Interestingly however, in the unbroken supersymmetry regime, W can be found analytically. In this case, by rewriting the eigenvalue equation (7.10) for the fundamental bound state of the original potential $\mathcal{H}\psi_0 = \mu_0\psi_0$ and after using the factorization relation (7.11) one finds that: $\mathcal{B}\mathcal{A}\psi_0 = 0$. This in turn leads to $\mathcal{A}\psi_0 = 0$ and as a result W can be obtained in terms of this fundamental mode as:

$$W(X) = -\frac{d}{dX}\ln\psi_0 \tag{7.14}$$

Note that ψ_0 is a nonzero function of X and therefore the superpotential W obtained by Eq. (7.15) is never singular.

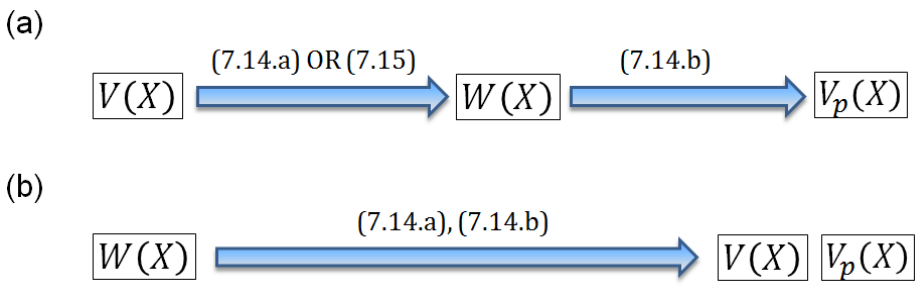

Figure 7.2. (a) Finding a superppartner for a given original potential, (b) finding two superpartner potentials from a given superpotential W.

As a result by starting from an original optical potential, one can always obtain the superpotential W and from there the superpartner potential V_p can be obtained easily by using Equation (7.14.b). This process is shown in Figure (7.2.a). Note also that in this case, one can deliberately find an unbroken or broken superpartner. An alternative approach is to start with an arbitrary superpotential $W(X)$ and construct the two superpartner potentials $V(X)$ and $V_p(X)$ according to Equations (7.14) (Figure 7.2(b)). In this scenario, a question natural arises as to whether these two superpartner potentials are in the unbroken or broken supersymmetry regimes. In quantum field theories this is addressed through a topological number so-called Witten index [6]. In our case, to answer this question, let us first assume that SUSY is unbroken. As a result the ground state of the first potential can be obtained through Equation (7.15):

$$\psi_0 \sim \exp\left(-\int_{-\infty}^{X} W(X')dX'\right) \tag{7.15}$$

Note that ψ_0 can represent a bound state only if it is square integrible and for this to happen $W(X)$ should take opposite signs at positive and negative infinities. On the other hand all realistic optical potentials approach a finite and constant value at infinities therefore for $X \to \pm\infty$ the superpotential approaches constant values $W \to W_{\pm}$. As a result unbroken SUSY regime unbroken SUSY requires $W_+ = -W_-$, while a broken SUSY demands that $W_+ = W_-$.

Finally, note that based on Equations (7.11) and (7.12) the eigenstates of the two superpartner Hamiltonians can be related pairwise via:

$$\psi_p(X) \propto \mathcal{A}\psi(X) = \left(\frac{d}{dX} + W\right)\psi(X), \tag{7.16.a}$$

$$\psi(X) \propto \mathcal{B}\psi_p(X) = \left(\frac{d}{dX} - W\right)\psi_p(X). \tag{7.16.b}$$

This relation is in general true not only for the bound states of the two partner structures but also for the scattering states.

Figure 7.3 depicts an exemplary optical potential, along with its superpartner in the unbroken SUSY regime. The associated superpotential is also depicted in part (c) of this figure. In this example, the original potential supports six bound states while its unbroken superpartner supports five modes.

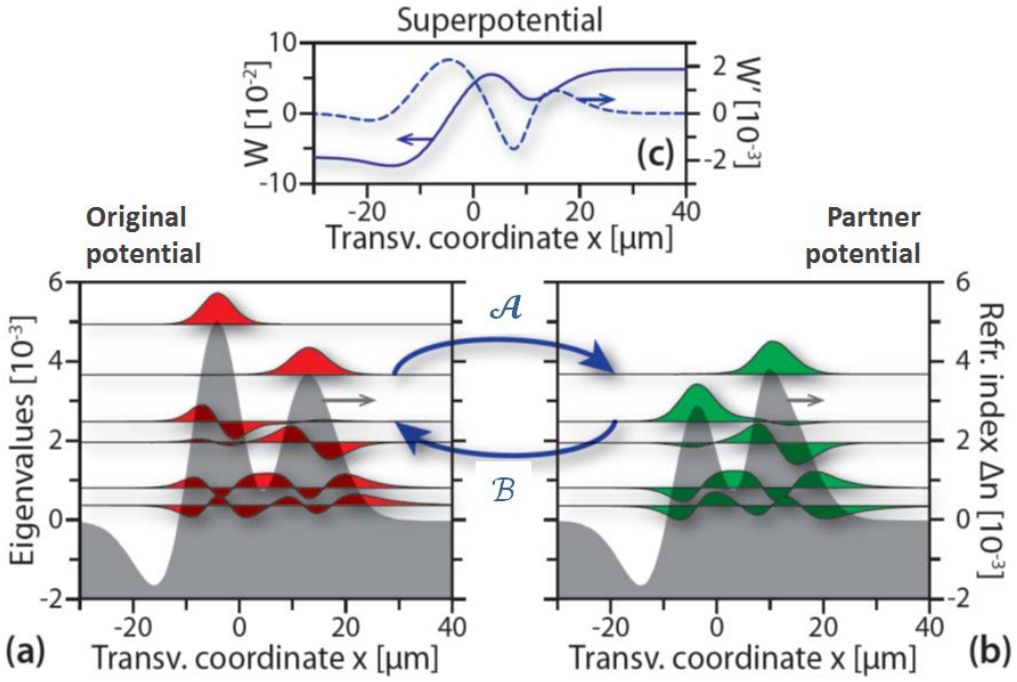

Figure 7.3. (a) Exemplary refractive index landscape (gray area) and its six bound modes (vertical placement indicates their respective eigenvalues). (b) SUSY partner and its five modes. The operators $\mathcal{A}$, $\mathcal{B}$ transform the phase-matched modes into each other. (c) Both index landscapes can be constructed from the superpotential $W(X)$ and its first derivative $W'(X)$.

7.3. Iso-spectral potentials

It is important to note that more than one superpotential can exist for any given distribution $V(X)$. In fact, as we show here, one can systematically generate an entire parametric family $W_f(X;C)$ of viable superpotentials (with parameter C) which establish a

partnership relation between a family of original potentials $V_f(X;C)$ and a fixed superpartner potential $V_p(X)$. To show this, let us first consider:

$$V_f(X;C) = +W_f'(X;C) - W_f^2(X;C) + \alpha, \tag{7.17.a}$$

$$V_p(X) \quad = -W_f'(X;C) - W_f^2(X;C) + \alpha. \tag{7.17.b}$$

and solve for the family of W_f that satisfy the second equation. Starting from a particular W, this solution can be generalized by adopting the form $W_f = W + 1/v$, in which case the unknown function v satisfies $(d/dX - 2W)v = 1$. Direct integration readily leads to $v = e^{+2\int_{-\infty}^{X} W dX'}\left(C + \int_{-\infty}^{X} e^{-2\int_{-\infty}^{X'} W dX''} dX'\right)$, where C is an arbitrary real-valued constant, giving rise to a parametric family W_f of superpotentials $W_f(X;C) = W + \partial_X \ln\left(C + \int_{-\infty}^{X} e^{-2\int_{-\infty}^{X'} W dX''} dX'\right)$. If the superpotential W has been specifically obtained from the bound state ψ_0 (from Equation (7.15)), then this parametric family can be obtained via:

$$W_f(X;C) = W + \frac{\mathrm{d}}{dX}\ln\left(C + \int_{-\infty}^{X} \psi_0^2(X')dX'\right). \tag{7.18}$$

Whereas all members of this family lead to the same superpartner V_p, each of them describes a different original potential $V_f(X;C)$ according to Equation (7.18.a). The resulting parametric family [12] of structures $V_f(X;C)$ is associated with the fundamental distribution $V(X)$ and its ground state ψ_0 as follows:

$$V_f(X;C) = V(X) + 2\partial_{XX}\ln\left(C + \int_{-\infty}^{X} \psi_0^2(X')dX'\right), \tag{7.19}$$

where C represents a free parameter. Note that here the transformation between the original structure and its superpartner was only used to prove Equation (7.20), which itself is completely independent from the superpartner. According to this equation, simply by starting from a given potential and its ground state eigenfunction, a whole family of iso-spectral potentials can be established. According to equations (7.18), the eigenstates of the iso-spectral potentials ψ_f are related to that of the superpartner potential ψ_p according to $\psi_f \propto \left(d/dX - W_f\right)\psi_p$. On the other hand, according to Equations (7.14), $\psi_p(X) = (d/dX + W)\psi$, therefore:

$$\psi_f \propto \left(\frac{d}{dX} - W_f\right)\left(\frac{d}{dX} + W\right)\psi. \tag{7.20}$$

7.4. Inverse supersymmetry

In the unbroken symmetry regime, the conventional SUSY transformation may remove a mode from a given fundamental structure V. In doing so, the total area of the refractive index is reduced. This can be shown easily by noting that in the unbroken supersymmetry regime the two superpartners are related via

$$V_p - V = -2W'. \tag{7.21}$$

After integrating both sides of this equation we get

$$\int_{-\infty}^{+\infty} V_p(X)dX - \int_{-\infty}^{+\infty} V(X)dX = -2(W_+ - W_-)\,. \tag{7.22}$$

Since in the unbroken supersymmetry regime $W_- \neq W_+$, the SUSY transformation cannot preserve the total area of the relative permittivity distribution.

On the other hand, one can utilize an inverse SUSY transformation and add a bound state to a given structure V, and in doing so elevate the total area of a given permittivity distribution. We factorize the fundamental Hamiltonian as $\mathcal{H} = \mathcal{A}\mathcal{B} + \alpha$ and define the partner Hamiltonian as $\mathcal{H}_e = \mathcal{B}\mathcal{A} + \alpha$. Consequently, the two superpartner permittivity distributions can be written as:

$$V(X) = -W_e' - W_e^2 + \alpha, \tag{7.23.a}$$

$$V_e(X) = +W_e' - W_e^2 + \alpha. \tag{7.23.b}$$

Equation (7.24.a) can be solved numerically to obtain the superpotential W_e, and from that the partner structure V_e can be constructed through Equation (7.24.b). Note that, by imposing appropriate asymptotic conditions for this superpotential, both the unbroken and broken supersymmetry regimes can be established. In this case, in the unbroken SUSY regime, the partner structure V_e exhibits all the guided mode eigenvalue spectrum of the fundamental structure V, as well as an additional guided mode, which takes the place of its previous ground state. As it turns out, the eigenvalue of this additional state is given by the factorization parameter α. Note that any value $\alpha > \Omega_0$ can be chosen, where Ω_0 represents the ground state eigenvalue of the fundamental structure.

7.5. SUSY in non-paraxial regime: TE polarization

Assume now an arbitrary one-dimensional distribution of the relative permittivity $\epsilon(x) = n^2(x)$ along the x axis. Waves propagating in the xy-plane can always be The evolution of TE waves is governed by the Helmholtz equation $\left(\partial^2/\partial x^2 + \partial^2/\partial y^2 + k_0^2\epsilon(x)\right)E_z(x,y) = 0$ where the E_z component is normal to the plane of propagation. By assuming eigenmode solutions of the form $E_z(x,y) = f(x)e^{i\beta y}$ and after defining normalized dimensionless coordinates $X = k_0 x$ and $Y = k_0 y$, the following Schrödinger-like equation is obtained:

$$\left(\frac{d^2}{dX^2} + V(X)\right)\psi(X) = \Omega\psi(X), \tag{7.24}$$

in which $V(X) = \epsilon(X)$ and $\Omega = \beta^2/k_0^2$. Note that this is the same as Equation (7.10) therefore supersymmetry can be directly applied.

7.6. SUSY in non-paraxial regime: TM polarization

Under TM polarization conditions the magnetic field component satisfies the equation:

$$\left(\frac{\partial^2}{\partial X^2} - \frac{\partial}{\partial X}(\ln\epsilon)\frac{\partial}{\partial X} + \epsilon\right)H_Z = \Omega H_Z \tag{7.25}$$

As is, this is not a Schrödinger-like equation, and hence the factorization technique cannot be directly applied. On the other hand, by using the transformation $\psi = \sqrt{\epsilon} H_Z$, this equation can be converted to the desired form:

$$\left(\frac{d^2}{dX^2} + V_{\text{eff}}\right)\psi = \Omega\psi \tag{7.26}$$

where V_{eff} is an effective potential that can be expressed in terms of the relative permittivity ϵ as $V_{\text{eff}} = \epsilon - \frac{3}{4}(\epsilon'/\epsilon)^2 + \frac{1}{2}(\epsilon''/\epsilon)$. This relation can also be rewritten as:

$$V_{\text{eff}} = \epsilon + \left(\frac{\epsilon'}{2\epsilon}\right)' - \left(\frac{\epsilon'}{2\epsilon}\right)^2 \tag{7.27}$$

Following the SUSY formalism, the two superpartner effective potentials can now be written in terms of the superpotential W via

$$V_{\text{eff}}(X) = +W' - W^2 + \alpha, \tag{7.28.a}$$

$$V_{\text{eff},p}(X) = -W' - W^2 + \alpha. \tag{7.28.b}$$

One can then reconstruct the relative permittivity of the partner structure ϵ_p from its corresponding effective potential $V_{\text{eff},p}$ by numerically solving the nonlinear equation

$$V_{\text{eff},p} = \epsilon_p + \left(\frac{\epsilon_p'}{2\epsilon_p}\right)' - \left(\frac{\epsilon_p'}{2\epsilon_p}\right)^2. \tag{7.29}$$

7.7. References

1. P. Ramond, "Dual theory for free fermions," Phys. Rev. D **3**, 2415 (1971).

2. Neveu and J. H. Schwarz, "Factorizable dual model of pions," Nucl. Phys. B **31**, 86 (1971).

3. Y. A. Gel'fand and E. P. Likhtman, JETP Lett. **13**, 323 (1971).

4. D. V. Volkov and V. P. Akulov, "Is the neutrino a Goldstone particle?," Phys. Lett. B **46**, 109 (1973).

5. J. Wess and B. Zumino, "Supergauge transformations in four dimensions," Nucl. Phys. B **70**, 39 (1974).

6. E. Witten, "Dynamical breaking of supersymmetry," Nucl. Phys. B **188**, 513 (1981).

7. P. Binetruy, "*Supersymmetry: Theory, Experiment and Cosmology*," Oxford University Press, Oxford (2006).

8. K. Efetov, "*Supersymmetry in Disorder and Chaos*," Cambridge University Press, Cambridge (1999)

9. F. Cooper and B. Freedman, "Aspects of supersymmetric quantum mechanics," Ann. Phys. **146**, 262 (1983).

10. L. E. Gendenshtein and I. V. Krive, "Supersymmetry in quantum mechanics", Usp. Fiz. Nauk **146**, 553-590 (August 1985).

11. A. Lahiri, P. Roy, and B. Bagchi, "Supersymmetry in quantum mechanics," Int. Jour. Mod. Phys. A **5**, 1383 (1990).

12. F. Cooper, A. Khare, and U. Sukhatme, "Supersymmetry and quantum mechanics," Phys. Rep. **251**, 267385 (1995).

13. J. Bai and D. Citrin, "Supersymmetric optimization of second-harmonic generation in mid-infrared quantum cascade lasers," Opt. Express **14**, 4043 (2006).

14. J. Radovanović, V. Milanović, Z. Ikonić, and D. Indjin, "Quantum-well shape optimization for intersubband-related electro-optic modulation properties," Phys. Rev. B **59**, 5637 (1999).

15. M.-A. Miri, M. Heinrich, R. El-Ganainy, and D. N. Christodoulides, “Supersymmetric optical structures,” Phys. Rev. Lett. **110**, 233902 (2013).

CHAPTER EIGHT: SUPERSYMMETRY IN OPTICAL WAVEGUIDES

In this chapter we utilize the formalism of supersymmetry in guided wave optical structures in order to establish a superpartnership relation between optical waveguides. We first explore this possibility in graded index planar waveguides. We show that two such superpartners can share the same set of propagation constants. In addition, we present analytical expressions for the superpartners of the well-known planar optical waveguides. Afterwards we explore supersymmetry in periodic array of optical waveguides and we show that two superpartner periodic systems exhibit identical band structures. In addition we show that, within the framework of the tight-binding approximation, SUSY formalism can be applied to photonic lattices by using simple matrix operations. We then present the first experimental demonstration of beam dynamics in supersymmetric lattices. We finally show that SUSY formalism can also be applied to circularly symmetric fiber waveguides. Based on the interesting global phase matching property of SUSY partner waveguides, we propose the possibility of mode filtering and mode multiplexing in SUSY structures.

8.1. Supersymmetry in one-dimensional optical waveguides

In this section we show use the SUSY formalism developed in previous chapter to find a superpartner for several examples of optical waveguides [1]. Let us consider again a

dielectric waveguide which is described by a one-dimensional distribution of the relative permittivity along the x axis; $\epsilon(x) = n^2(x)$. Assuming time-harmonic waves propagating in the xy-plane, the electric field component of the TE-polarized light satisfies the following equation $\frac{\partial^2 E_z}{\partial x^2} + \frac{\partial^2 E_z}{\partial y^2} + k_0^2 \epsilon(x) E_z = 0$, where $k_0 = 2\pi/\lambda_0$ represents the free-space wavevector associated with the vacuum wavelength λ_0. The guided wave solutions ($E_z = f(x)e^{i\beta z}$) of this latter equation are governed by the eigenmode equation $\frac{d^2}{dx^2}\psi(x) + k_0^2 \epsilon(x)\psi(x) = \beta^2 \psi(x)$. Assuming that $\psi_0(x)$ represents the ground sate of the original waveguide, the relative permittivity of the superpartner waveguide is obtained from $\epsilon_p(x) = \epsilon(x) + \frac{2}{k_0^2}\frac{d^2}{dx^2}\ln\big(\psi_0(x)\big)$, which can also be simplified to:

$$\epsilon_p(x) = \epsilon(x) + \frac{2}{k_0^2}\left(\left(\frac{\psi_0''}{\psi_0}\right) - \left(\frac{\psi_0'}{\psi_0}\right)^2\right). \tag{8.1}$$

In the following sections we will employ this mathematical framework to identify superpartner structures for a number of exemplary optical waveguide profiles.

8.1.1 Slab waveguide

Consider a symmetric step-index slab waveguide with a core of relative permittivity ϵ_g and width $2h$ embedded in a substrate material with relative permittivity ϵ_s. The overall relative permittivity of this structure can be written as

$$\epsilon(x) = \begin{cases} \epsilon_g & |x| \le h \\ \epsilon_s & |x| > h \end{cases}. \tag{8.2}$$

For such a waveguide, the fundamental mode is known to follow the analytical expression

$$\psi_0(x) = \begin{cases} A\cos(\kappa_1 x) & |x| \le h \\ Be^{-\gamma_1(|x|-h)} & |x| > h \end{cases}. \tag{8.3}$$

where $\kappa_1 = \sqrt{k_0^2\epsilon_g - \beta_0^2}$, $\gamma_1 = \sqrt{\beta_0^2 - k_0^2\epsilon_s}$, $\kappa_1 \tan(\kappa_1 h) = \gamma_1$ and $B = A\cos(\kappa_1 h)$. Under these conditions, by using Equation (8.1) it is straightforward to show that the superpartner has the following form:

$$\epsilon_p(x) = \begin{cases} \epsilon_g - 2\frac{\kappa_1^2}{k_0^2}\sec^2(\kappa_1 x) & |x| \le h \\ \epsilon_s & |x| > h \end{cases}. \tag{8.4}$$

Based on Equation (8.4), the following points can be deduced: (a) The peak value of the relative permittivity of the partner waveguide is reduced to $\epsilon_{\max} = \epsilon_g - 2\,\kappa_1^2/k_0^2$. This is to be expected, since the partner waveguide should support one mode less. (b) Due to discontinuity of the original waveguide (and as a results the second derivative of its fundamental mode) at $x = \pm h$, the partner profile is also discontinuous at these edges. (c) The discontinuity of the original waveguide, leads to sharp features in the partner waveguide especially at the edges of the core where the relative permittivity goes even below that of the substrate medium. However, it should be noted that $\epsilon^{(2)}$ is free of any singularities since $\kappa_1 h$ is always less than $\pi/2$.

Figure 8.1 depicts the relative permittivity of the slab waveguide and its superpartner. In each case the mode profiles are also shown, while the vertical position of these modes indicates their respective eigenvalue β_n^2/k_0^2 (effective index squared). In this example, the slab waveguide (parameters $\epsilon_s = 2$, $\epsilon_g = 2.1$, $h = 3\mu m$) supports four guided modes, and its superpartner supports three guided modes.

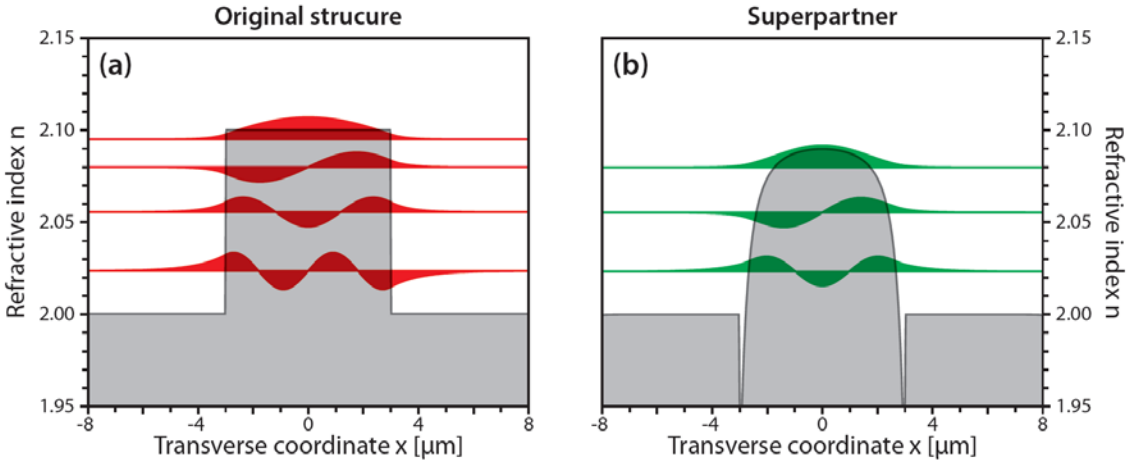

Figure 8.1. (a) Relative permittivity distribution of a slab waveguide with $\epsilon_s = 2$, $\epsilon_g = 2.1$ and $h = 3\mu m$. (b) Relative permittivity distribution of the superpartner waveguide. In each case the mode profiles are also plotted while the vertical position of each mode shows their respective eigenvalue $\Omega_n = \beta_n^2/k_0^2$.

8.1.2. Super-Gaussian waveguide

In order to avoid the inherent discontinuities of the step-index slab waveguide and its superpartner, here we consider a super-Gaussian profile

$$\epsilon = \epsilon_s + (\epsilon_g - \epsilon_s)\exp\left(-\left(\frac{x}{h}\right)^{2n}\right), \tag{8.5}$$

of high order $2n \gg 1$. Note that for $2n \to \infty$, such a profile approaches the step-index waveguide profile of Equation (8.2). To obtain a reasonably sharp transition, here we choose $2n = 8$. Figure 8.2(a) depicts the corresponding super-Gaussian profile with parameters similar to that of Figure 8.1(a). In this case the eigenmodes and the superpartner waveguide are obtained numerically by using standard finite-difference schemes. As can be seen in Figure 8.2(b) the superpartner waveguide now features a smooth permittivity profile.

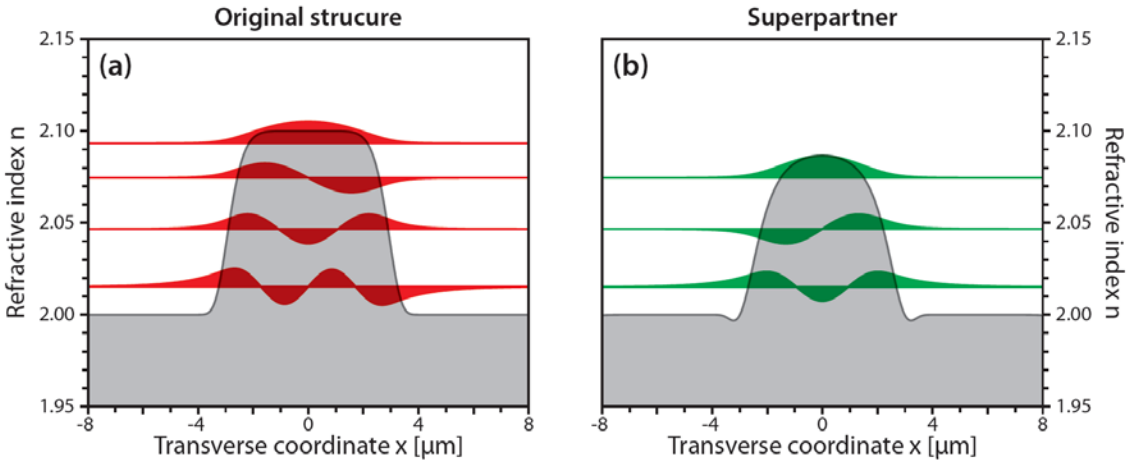

Figure 8.2. A super-Gaussian waveguide profile (a) and its superpartner (b).

8.1.3. Parabolic waveguide

Next, we consider the parabolic waveguide. This profile is one of the few continuous index distributions, which can be solved analytically [2] (after using some approximations). Similar to the quantum mechanical harmonic oscillator, the parabolic waveguide exhibit interesting properties including an equidistant eigenvalue spectrum. As a result, as we will see, the superpartner of a parabolic waveguide is another parabolic waveguide that is downshifted in relative permittivity. In general a parabolic graded index waveguide profile can be described via

$$\epsilon = \begin{cases} \left(\epsilon_g - \left(\epsilon_g - \epsilon_s\right)(x/h)^2\right) & |x| \le h \\ \epsilon_s & |x| > h\,. \end{cases} \tag{8.6}$$

For highly multimode structures, this can be approximated with by an infinitely extended parabola

$$\epsilon \approx \epsilon_g - \left(\epsilon_g - \epsilon_s\right)(x/h)^2 \tag{8.7}$$

with the corresponding fundamental mode

$$\psi_0 = \exp\left(-\frac{k_0}{2h}\sqrt{\epsilon_g - \epsilon_s}x^2\right) \tag{8.8}$$

and its associated propagation constant:

$$\beta_0 = \left(k_0^2\epsilon_g - \frac{k_0}{h}\sqrt{\epsilon_g - \epsilon_s}\right)^{1/2} \tag{8.9}$$

Using, Equation (8.1) the superpartner waveguide profile can be obtained as:

$$\epsilon_p \approx \epsilon_g - \frac{2}{k_0 h}\sqrt{\epsilon_g - \epsilon_s} - (\epsilon_g - \epsilon_s)\left(\frac{x}{h}\right)^2 \tag{8.10}$$

This last relation again represents a parabola, which is vertically shifted by $\Delta\epsilon = -\frac{2}{k_0 h}\sqrt{\epsilon_g - \epsilon_s}$ with respect to the original one. Figure 8.3(a) depicts a parabolic waveguide with $\epsilon_s = 2$, $\epsilon_g = 2.1$ and $h = 5\mu m$. The dashed blue line outlines the envelope parabola. The superpartner waveguide along with its parabolic envelope calculated from Equation (8.10) are plotted in Figure 8.3(b).

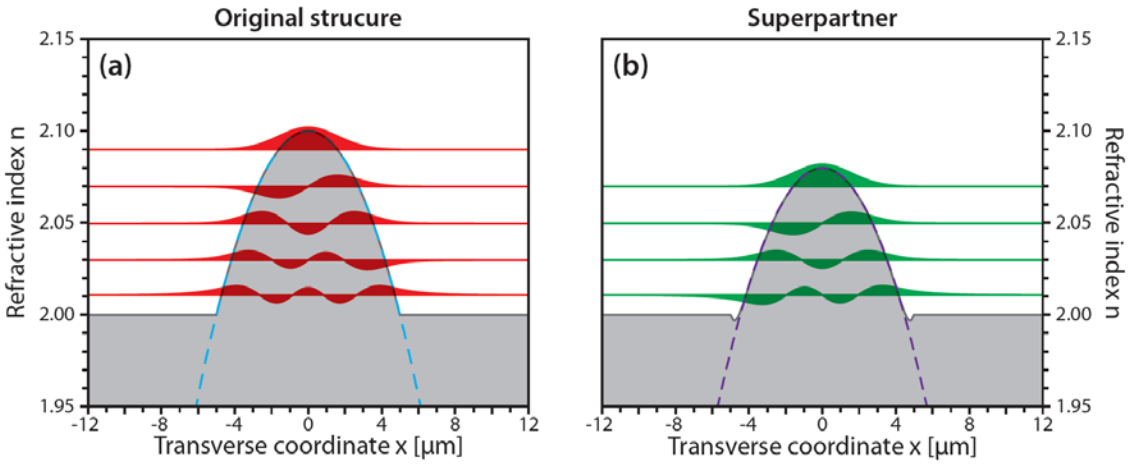

Figure 8.3. Parabolic waveguide with $\epsilon_s = 2$, $\epsilon_g = 2.1$ and $h = 5\mu m$ (a) and its superpartner (b). In each case the solid black line shows the waveguide itself while the dashed blue line depicts the parabolic envelope. Note that the superpartner and all the eigenmodes are calculated numerically. However, the analytical results obtained from the parabolic approximation are very close to numerical findings.

8.1.4. Exponential waveguide

Here, we consider the exponential waveguide which again exhibits an analytic solution. The exponential profile is described with:

$$\epsilon = \epsilon_s + \left(\epsilon_g - \epsilon_s\right)e^{-|x|/h}. \tag{8.11}$$

Using a change of variable of $\xi = e^{-|x|/2h}$, one can show that the governing Helmhltz equation under this distribution of permittivity can be converted to the Bessel equation and therefore the fundamental mode of this waveguide can be written as [2]:

$$\psi_0(x) = J_{p_0}\left(Ve^{-|x|/2h}\right), \tag{8.12}$$

and the fundamental mode has the following eigenvalue:

$$\beta_0 = \sqrt{k_0^2\epsilon_s + p_0^2/4h^2}, \tag{8.13}$$

where $V = 2k_0h\sqrt{\epsilon_g - \epsilon_s}$, and p_0 can be obtained from the following relation

$$J'_{p_0}(V) = 0. \tag{8.14}$$

As a result, the partner waveguide can be written as:

$$\epsilon_p(x) = \epsilon_s + \left(\epsilon_g - \epsilon_s\right)e^{-|x|/h} + \\ + \frac{1}{2k_0^2h^2}\left(V^2e^{-|x|/h}\left(\frac{J''_{p_0}\left(Ve^{-|x|/2h}\right)}{J_{p_0}\left(Ve^{-|x|/2h}\right)} - \frac{{J'_{p_0}}^2\left(Ve^{-|x|/2h}\right)}{J^2_{p_0}\left(Ve^{-|x|/2h}\right)}\right) + Ve^{-|x|/2h}\frac{J'_{p_0}\left(Ve^{-|x|/2h}\right)}{J_{p_0}\left(Ve^{-|x|/2h}\right)}\right) \tag{8.15}$$

Figure 8.4 depicts an exponential waveguide profile with $\epsilon_s = 2$, $\epsilon_g = 2.1$ and $h = 3\mu m$ and its superpartner. As this figure shows, the superpartner faithfully reproduces the decreasing eigenvalue spacing for higher order modes in such a structure.

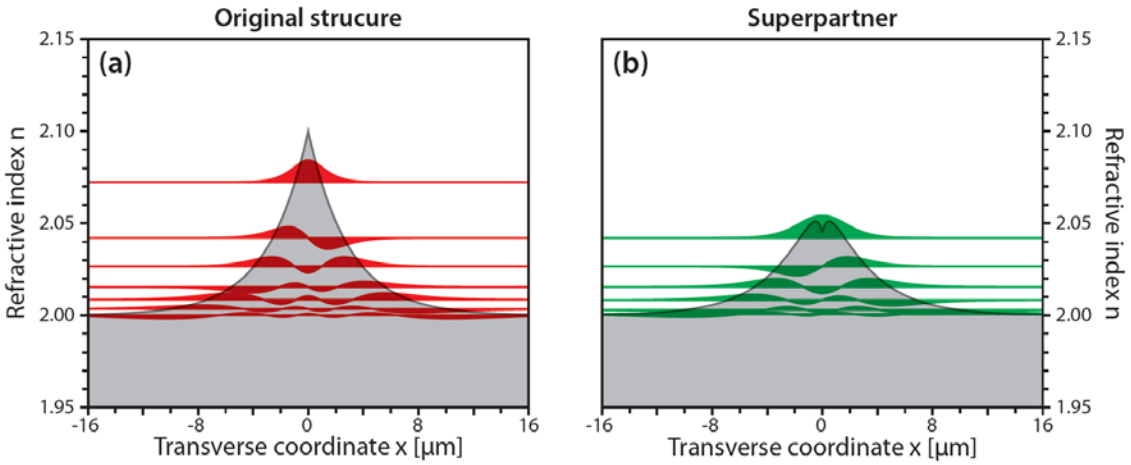

Figure 8.4. The exponential waveguide with $\epsilon_s = 2$, $\epsilon_g = 2.1$ and $h = 3\mu m$ (a), and its superpartner (b).

8.1.5. Hierarchichal ladder of supersymmetric waveguides

The formalism outlined in the previous sections can be iteratively applied in order to synthesize a ladder of optical waveguides, each of which acts as superpartner to the adjacent channel. This is shown in Figure 8.5, using the super-Gaussian waveguide shown in Figure 8.2 as fundamental structure. SUSY transformations are then used to remove the guided modes one by one, until reaching a single-mode configuration. In each step, the

remaining modes of the resulting waveguide are phase matched to the higher order modes of the previous step's waveguide.

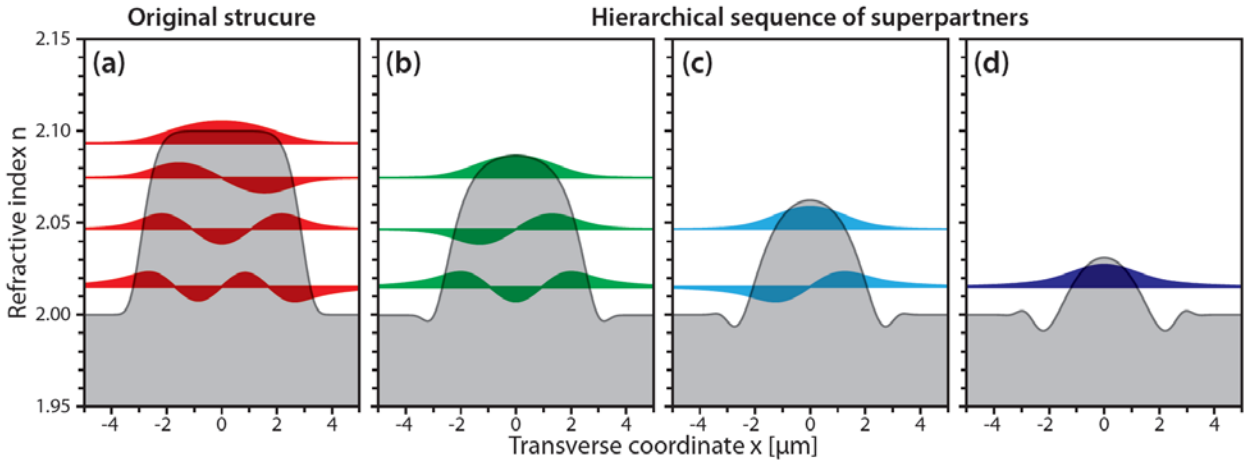

Figure 8.5. A hierarchical ladder of SUSY waveguides.

8.2. Supersymmetric optical fibers

As discussed in the previous chapter, supersymmetry is based on the factorization of the second order Hamiltonian operator of the Schrödinger equation. In general such factorization is limited to one-dimensional operators. In particular cases, however, the formalism of supersymmetry can be applied to two-dimensional structures. Perhaps the simplest case will be a separable potential i.e., $V(x,y) = f(x) + g(y)$. In this case the 2D Schrödinger equation can be reduced to two 1D schrodinger equation. On the other hand as we will see here, for structures with cylindrical

symmetry the formalism of supersymmetry can be exploited to construct superpartner structures with cylindrical symmetry.

In this section we investigate the formalism of supersymmetry in circularly symmetric dielectric waveguides. Perhaps the best know example of such a waveguide is the step index fiber. As we will show for such structure, under the paraxial approximation the evolution equation can reduce to a 1D Schrödinger-like equation. The factorization technique can then be applied and as a result SUSY partner fibers can be constructed.

Consider a circularly symmetric refractive index profile of $n(r) = n_0 + \Delta n(r)$ where $\Delta n \ll n_0$ and the profile is assumed to be uniform in the propagation direction z. Within the framework of paraxial approximation the slowly varying field envelope satisfies the paraxial equation

$$i\frac{\partial}{\partial \xi}U + \left(\frac{\partial^2}{\partial \eta^2} + \frac{1}{\eta}\frac{\partial}{\partial \eta} + \frac{1}{\eta^2}\frac{\partial^2}{\partial \phi^2} + V(\eta)\right)U = 0, \tag{8.16}$$

where in this relation U is the slowly varying envelope of the electric field, and η is the normalized radial coordinate $\eta = r/r_0$, ϕ represents the azimuthal coordinate and ξ stands for the normalized longitudinal coordinate $\xi = z/(2k_0 n_0 r_0^2)$. Finally $V = 2n_0 k_0^2 r_0^2 n_1$ is the optical potential. By assuming eigenmode solutions of the form $U = e^{i\mu\xi}e^{il\phi}R(\eta)$ Equation (8.16) can be simplified as $\left(\frac{\partial^2}{\partial \eta^2} + \frac{1}{\eta}\frac{\partial}{\partial \eta} + V(\eta) - \frac{l^2}{\eta^2}\right)R = \mu R$. This equation can be converted to the standard canonical form by using the gauge transformation $R = \eta^{-\frac{1}{2}}u$:

$$\left(\frac{d^2}{dr^2} + \mathrm{V_{eff}}(r)\right)u = \mu u, \tag{8.17}$$

where V_{eff} is an effective potential defined as $V_{\text{eff}}(\eta) = V(\eta) + \frac{\frac{1}{4}-l^2}{\eta^2}$. Clearly this effective potential depends on the azimuthal mode number l. Therefore one expect the supersymmetry to be hold only for a specific pair of modes corresponding to one azimuthal order l. In other words by labeling different modes of the guide by R_{lm} (where l and n are azimuthal and radial mode numbers respectively) for certain l_1 and l_2 only the two set of $R_{l_1 m}$ and $R_{l_2 m}$ from two guides can share the eigenmode spectra. To find the relation between l_1 and l_2 we use SUSY algebra to first establish the second potential. By assuming u_0 as the ground state of Equation (8.17) the second potential can be written as $V_{p,\text{eff}} = V_{\text{eff}} + 2\frac{d^2}{d\eta^2}(\ln u_{l0})$. By writing the effective potentials in terms of the original potential and by using the fact that $R_{l0} = \eta^{-\frac{1}{2}} u_{l0}$ one can show:

$$V_p(\eta) = V(\eta) + 2\frac{d^2}{d\eta^2}\left(\ln\left(\eta^{\frac{l_1^2 - l_2^2 + 1}{2}} R^{(1)}_{l_1,0}\right)\right) \tag{8.18}$$

Note that here $R_{l_1,0}$ is the radial part of the ground state of Equation (8.16). In general the partner potential V_p due to its second term in Equation (8.18) can be singular at the origin $\eta = 0$. However as we will discuss in what follows l_1 and l_2 can be chosen in a correct way so as to avoid this singularity. In general one can show that for any arbitrary well behaved potential $V_p(\eta)$, solution of the radial part of Equation (8.16) for an azimuthal number l_1 and for $\eta \ll 1$ is proportional to $\eta^{|l_1|}$, therefore $R_0(\eta) \sim \eta^{|l_1|}$ for $\eta \ll 1$. Therefore the only possible choice of l_2 which leads to a non-singular solution is governed by:

$$|l_2| = |l_1| + 1. \tag{8.19}$$

This latter relation reveals an interesting property of supersymmetric circularly symmetric optical waveguides; the supersymmetric ladder holds only between two sets of modes while there is a difference of unity between the azimuthal numbers of these two sets. Finally since the behavior of the partner potential V_p was studied for $\eta \to 0$, it is also interesting to see how this potential behaves for large very large η in the so called cladding regions of the fiber. This latter can be of practical importance in realization of supersymmetric optical fibers. Assuming that the first potential is approximately zero for large values of η it can be shown that $R_{l_1,0}^{(1)} \sim \frac{1}{\sqrt{\eta}} e^{-\sqrt{\mu}\eta}$. Using this latter relation in Equation (8.18) we finally get $V_p(\eta) \to 1/\eta^2$ for $\eta \to \infty$.

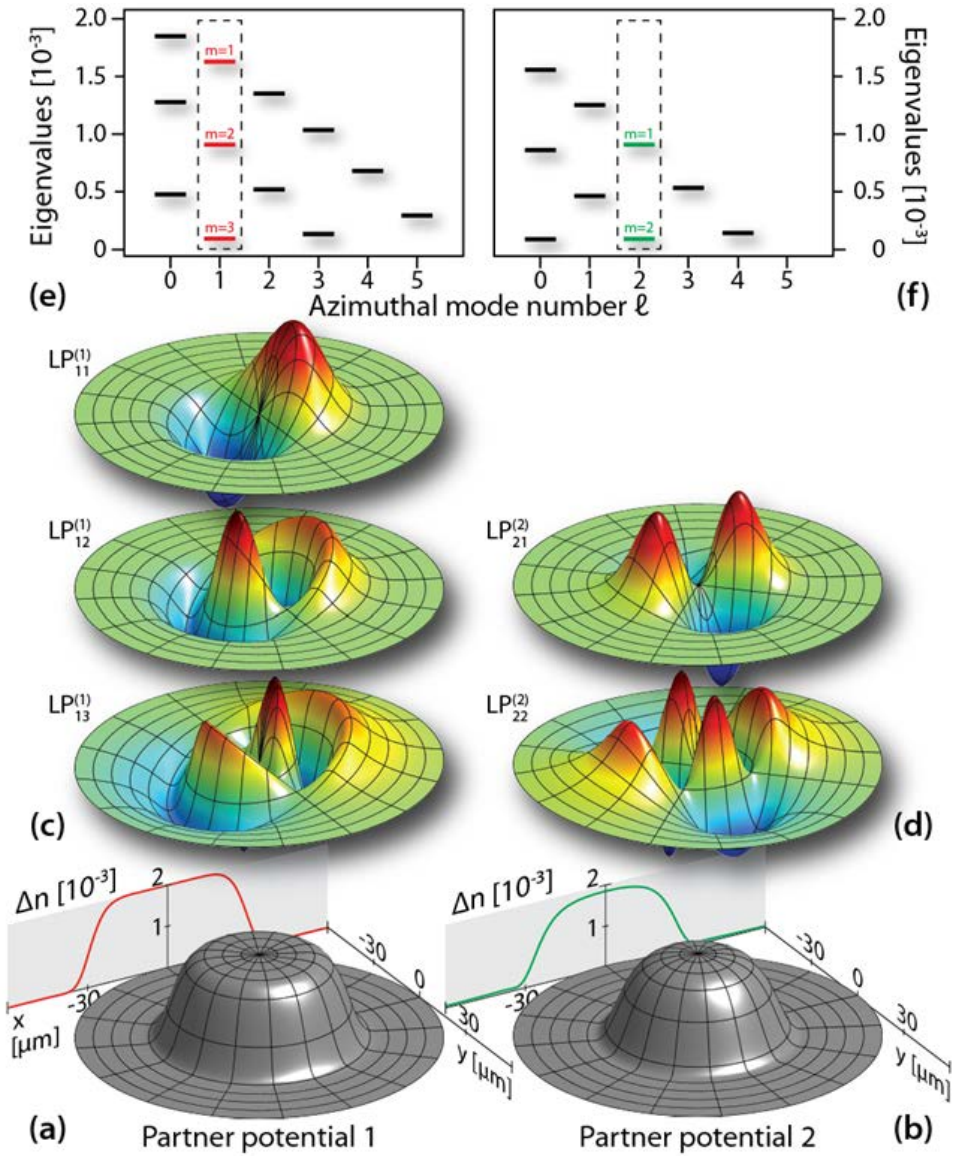

Figure 8.6. (a) Refractive index profile of a cylindrically symmetric fiber. (b) Index profile of the SUSY partner obtained for a choice of $l^{(1)} = 1$ / $l^{(2)} = 2$. (c) Bound states of potential 1 with radial mode number $l^{(1)} = 1$. (d) Corresponding SUSY states of potential 2 with radial mode number $l^{(2)} = 2$. (e,f) Complete eigenvalue spectra (effective refractive indices) of both potentials. The respective subsets of SUSY states are indicated by dashed frames.

Figure 8.6(a,b) depicts two super-partner circularly symmetric optical waveguides. The first guide is a multimode optical fiber of 60μm diameter while the index difference between the core and cladding is assumed to be $\Delta = 0.002$ and cladding has a refractive index of $n_0 = 1.5$. By assuming a refractive index profile of $n(r) = n_0 + \Delta e^{-(r/r_0)^8}$ where $r_0 = 30\mu m$, numerical solution of eigenvalue Equation (8.18) shows that this waveguide without counting the degeneracies supports 12 modes (modes corresponded to $l_1 = 0$ are not degenerate while those with $l_1 \neq 0$ are two-fold degenerate. Also note that in general there is a second factor of degeneracy due to polarization. Here we only consider one of the two linear polarization i.e. either x or y) with $l_1 = 0,1, \dots ,5$. For $l_1 = 1$, which includes three modes with different radial index, we numerically obtain the partner potential via Eq. (8.18). The eigenvalue ladders of both waveguides are shown in terms of effective indices ($N_{lm}^{(1,2)}$) in Figures 8.6(e,f). As expected the supersymmetric ladder holds between modes with $l_1 = 1$ in the first and $l_2 = 2$ in the second guide i.e. $N_{1,m+1}^{(2)} = N_{2,m}^{(1)}$ for $m = 1,2$ but $N_{11}^{(1)}$ that is completely removed from the second guide. The corresponding filed profiles of this set of modes are also plotted in Figures 8.6(c,d). Although the supersymmetric ladder exist only between the set of $l_1 = 1$ and $l_2 = 2$, the eigenvalues between any set of l_1 and $l_2 = l_1 + 1$ are very close even though they do not match and supersymmetry does not exist. This qusi-supersymmetric behavior is clearly indicated in Figures 8.6(e,f).

8.3. SUSY for mode filtering and mode demultiplexing applications

As shown in section 8.1, SUSY provides a way to achieve global phase matching condition between a large number of modes in two multimode optical waveguides while the fundamental mode is excluded from this phase matching principle. This interesting property can be exploited for mode filtering applications [3]. This idea is illustrated in Figure 8.7 where the first channel has the form of a step-index like waveguide that supports three modes at $\lambda_0 = 1\mu m$. The optical propagation when this system is excited with an arbitrary input beam, is depicted in the first propagation section of this figure. In this range, the field evolution is almost chaotic because of modal interference. Once however the superpartner waveguide is put in proximity, then because of phase matching, all the modes of of n (apart from the fundamental) are periodically coupled between these two structures. If for example the second waveguide is made intentionally lossy, then all the modes of n eventually disappear except the fundamental-as shown in Figures 8.7(b,c). In principle, the fundamental mode in this arrangement can also be selectively amplified if gain is introduced in the first waveguide while suppressing the rest of the modes. This behavior could be potentially very useful in large area laser sources.

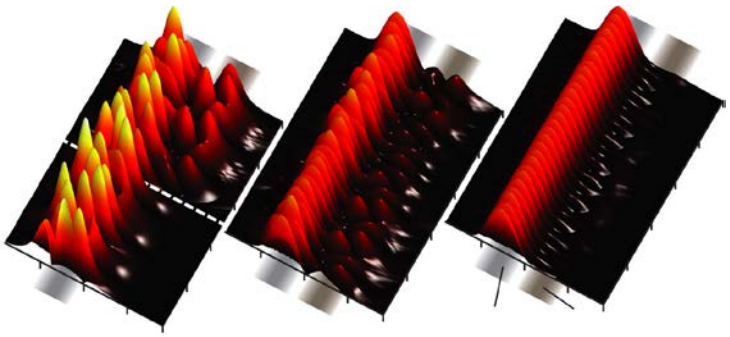

Figure 8.7. Beam propagation in a multimode waveguide. (a) When isolated (before dashed line), and when coupled to its lossy superpartner (after dashed line, losses: 0.4cm^{-1}). Two more advanced stages of this same field evolution in the coupled system are shown in (b), (c).

8.4. References

1. M.-A. Miri, M. Heinrich, and D. N. Christodoulides, "Supersymmetric optical waveguides", Proc. SPIE 8980, Physics and Simulation of Optoelectronic Devices XXII, 89801F (March 7, 2014).

2. T. Tamir, "*Guided-Wave Optoelectronics*," Springler-Verlag, New York (1988).

3. M.-A. Miri, M. Heinrich, R. El-Ganainy, and D. N. Christodoulides, "Supersymmetric Optical Structures," Phys. Rev. Lett. **110**, 233902 (2013).

CHAPTER NINE: SYPERSYMEETRY AND SCATTERING

The problem of reconstructing the shape of a potential distribution solely from information carried by its far-field scattering pattern has a long-standing history in various disciplines. These include classical optics [1-3], quantum mechanics [4,5] and applied mathematics [6,7]. Naturally, the question of uniqueness is of crucial importance: Is an object fully described by the amplitudes and phases of its reflection and transmission coefficients for all angles of incidence? Indeed, as long as a potential does not support any bound states, the far-field scattering information is unique. This is because one can always identify an N-parameter family of potentials with an identical discrete set of N bound-state eigenvalues, which exhibit the same scattering coefficients [7]. Closely related to this subject is the concept of supersymmetry (SUSY). In the context of quantum mechanics, supersymmetric methods have been utilized to identify isospectral and phase-equivalent potentials [8-12].

In recent years, advances in the field of transformation optics and optical conformal mapping, have brought forth a powerful new approach in solving inverse problems. Transformation optics allows one to find the constitutive parameters of a medium, which are required to manipulate optical wavefronts in a desired manner. Based on this method, optical devices with peculiar properties like invisibility cloaks, optical black holes and broadband graded index lenses have been proposed [13-18], to mention a few.

In general however, such structures call for a substantial range of control over the spatial distribution of electric permittivities and magnetic permeabilities of the materials involved. Clearly

of interest would be to develop alternative strategies that allow one to systematically control the scattering properties of an object, while at the same time reducing the complexity of the structures involved.

In this chapter, we explore the implications of optical supersymmetry in the context of scattering and introduce a new type of optical transformations in one-dimensional refractive index landscapes. Along these lines, we show that, in addition to superpartners with similar scattering behavior, systematic deformations allow one to construct structures that exhibit identical reflection and transmission coefficients, down to the phase, for all incident angles, rendering them perfectly indistinguishable in the far field. Our analytical results are illustrated in terms of pertinent examples.

9.1. Reflection/transmission coefficients of supersymmetric structures

In one-dimensionally inhomogeneous systems, the propagation of TE polarized waves is known to obey the Helmholtz equation $[\partial_{xx} + \partial_{yy} + k_0^2\epsilon(x)]E_z(x,y) = 0$ where k_0 is the vacuum wavenumber and $\epsilon(x)$ is the relative permittivity. The spatial dependence of the electric field E_z can be described via $E_z(x,y) = \psi(x)e^{i\beta y}$. Here, $\beta = k_0 n_b \sin\theta$ represents the y-component of the wave vector for an incidence angle θ, and $n_b = \sqrt{\epsilon_b}$ is the background refractive index. By employing the normalized quantities $X = k_0 x$, $Y = k_0 y$ and $\Omega = \beta^2/k_0^2$, the Helmholtz equation then reduces to a 1D Schrödinger-like equation

$H\psi(X) = \Omega\psi(X)$. In the following we related the reflection and transmission coefficients of two superprtner potentials.

9.1.1. Structures with similar backgrounds

We first assume that the original structure (and therefore its superpartner) has the same asymptotic behavior in positive and negative infinity, i.e., $n(x \to \pm\infty) = n_0$. This restriction is then removed in the next section where the general case is studied.

Consider two superpartner structures. Assuming a plane waves propagating towards such scatterers, of interest would be to see how the reflection/transmission coefficients of these superpartners are related. Let us first consider an incident plane wave with an angle θ described by $\exp(ixk_0n_0\cos\theta + iyk_0n_0\sin\theta)$ that hits both structures from the left side. The reflected and transmitted waves in the original structure are then described by $r\exp(-ixk_0n_0\cos\theta + iyk_0n_0\sin\theta)$ and $t\exp(ixk_0n_0\cos\theta + iyk_0n_0\sin\theta)$ respectively. Accordingly, in the superpartner structure the corresponding reflected and transmitted wave components are given by $r\exp(-ixk_0n_0\cos\theta + iyk_0n_0\sin\theta)$ and $t\exp(ixk_0n_0\cos\theta + iyk_0n_0\sin\theta)$. To find a relation between the scattering coefficients of the original (r, r) and the superpartner (r_p, t_p) structures, we use the fact that the scattering states of these two structures are related via the intervening operators $\mathcal{A}$ and $\mathcal{B}$. Such states are defined as

$$\psi(x) = N \times \begin{cases} e^{ixn_0\cos\theta} + re^{-ixn_0\cos\theta}, & x \to -\infty \\ te^{ixn_0\cos\theta}, & x \to +\infty \end{cases} \tag{9.1}$$

for the original and as

$$\psi_p(x) = N_p \times \begin{cases} e^{ixn_0\cos\theta} + r_p e^{-ixn_0\cos\theta}, & x \to -\infty \\ t_p e^{ixn_0\cos\theta}, & x \to +\infty \end{cases} \tag{9.2}$$

for the superpartner which both corresponds to the eigenvalue $\Omega = \Omega_p = n_0^2 \sin^2\theta$. Note that here $N_{1,2}$ represents an arbitrary scale for the scattering state that can be compared with the normalization factor in bound states. After applying the intervening relation $\psi_p \propto (d/dX + W)\psi$ between the wave functions of such radiation states from the two structures, one can readily show that

$$N_p\left(e^{+ixn_0\cos\theta} + r_p e^{-ixn_0\cos\theta}\right) = N\left((+in_0\cos\theta + W_-)e^{+ixn_0\cos\theta} + (-in_0\cos\theta + W_-)re^{-ixn_0\cos\theta}\right) \tag{9.3}$$

for $x \to -\infty$, and

$$N_p t_p e^{+ixn_0\cos\theta} = N(+in_0\cos\theta + W_+)te^{+ixn_0\cos\theta} \tag{9.4}$$

for $x \to +\infty$. In these two equations $W_\pm$ denotes the asymptotic limits of the superpotential W at $x \to \pm\infty$ respectively. Based on this two last relations, one can simply show that the reflection/transmission coefficients of the superpartner structures are related via:

$$r_p = \frac{W_- - ik_0n_0\cos\theta}{W_- + ik_0n_0\cos\theta} r, \tag{9.5.a}$$

$$t_p = \frac{W_+ + ik_0n_0\cos\theta}{W_- + ik_0n_0\cos\theta} t. \tag{9.5.b}$$

Obviously, the intensity of the reflected ($R = |r|^2 = |r_p|^2$) as well as the transmitted ($T = 1 - R = |t|^2 = |t_p|^2$) waves in the superpartner structures are identical. However, the phases are in general different and the phase difference depend on whether supersymmetry is unbroken or broken. In particular the reflection phases of the superpartners are different in both regimes. The transmission phases on the other hand are equal in the case of the broken supersymmetry since in this regime $W_- = W_+$.

9.1.2. Structures with dissimilar backgrounds

Consider now the case where the original structure (and therefore its superpartner) has different asymptotic behavior at positive and negative infinity, i.e., $n(x \to \pm\infty) = n_\pm$ where $n_- \neq n_+$. In this case the incident plane wave is assumed to be of the form of $\exp(ixk_0n_- \cos\theta_- + iyk_0n_- \sin\theta_-)$ while the reflected and transmitted wave components of the superpartners are $(r, r_p)\exp(-ixk_0n_- \cos\theta_- + iyk_0n_- \sin\theta_-)$ and $(t, t_p)\exp(ixk_0n_+ \cos\theta_+ + iyk_0n_+ \sin\theta_+)$ respectively. Here $\theta_\pm$ represent the propagation angles of the incoming or scattered waves at $x \to \pm\infty$ and are related via the Snell's law: $n_- \sin\theta_- = n_+ \sin\theta_+$. After following analogous steps to those of the previous section, it can be shown that the reflection/transmission coefficients of the two superpartners are connected through:

$$r_p = \frac{W_- - ik_0n_- \cos\theta_-}{W_- + ik_0n_- \cos\theta_-} r, \tag{9.6.a}$$

$$t_p = \frac{W_+ + ik_0 n_+ \cos\theta_+}{W_- + ik_0 n_- \cos\theta_-} t. \qquad (9.6.b)$$

Again, it follows that the intensity of the reflected ($R = |r_p|^2 = |r|^2$) and the transmitted ($T = 1 - R = |t_p|^2 \cdot (n_+/n_-)(\cos\theta_+ / \cos\theta_-) = |t|^2 \cdot (n_+/n_-)(\cos\theta_+ / \cos\theta_-)$) waves in the two structures are identical.

9.1.3. Scattering coefficients of the iso-spectral family of structures

In order to derive a relation between the reflection/transmission coefficients of the family iso-spectral structures $n_f(x;C)$ (which includes the original structure $n(x)$) we assume reflected and transmitted waves as $r_f \exp(-ixk_0 n_0 \cos\theta + iyk_0 n_0 \sin\theta)$ and $t_f \exp(ixk_0 n_0 \cos\theta + iyk_0 n_0 \sin\theta)$ respectively. We can then relate r_f and t_f to r and t via the relation $\psi_f \propto \left(\partial_x - W_f\right)(\partial_x + W)\psi$. Note that W_f itself can be written in terms of W and the ground state of the original potential. According to this relation, W_f and W have the same asymptotic behavior at $x \to \pm\infty$, i.e., $W_{f,\pm} = W_\pm$. Therefore, in the far field, the intervening relation simplifies to $\psi_f \propto (\partial_X - W)(\partial_X + W)\psi$. On the other hand, note that $(\partial_X - W)(\partial_X + W) = (\partial_{XX} + W' - W^2) = H - \alpha$, and therefore $\psi_f \propto (H - \alpha)\psi = (\Omega - \alpha)\psi$. Since the scattering states depend on y according to $\exp(iyk_0 n_0 \sin\theta)$, the corresponding eigenvalue in the Helmholtz equation is given by $\Omega = n_0^2 \sin^2\theta$. Hence, $\psi_f \propto (n_0^2 \sin^2\theta - \alpha)\psi$, and therefore:

$$N_f\left(e^{+iXn_0\cos\theta}+r_f e^{-iXn_0\cos\theta}\right)=N(n_0^2\sin^2\theta-\alpha)\left(e^{+iXn_0\cos\theta}+re^{-iXn_0\cos\theta}\right) \tag{9.7}$$

for $x\to-\infty$, and

$$N_f t_f e^{+iXn_0\cos\theta}=N(n_0^2\sin^2\theta-\alpha)te^{+iXn_0\cos\theta} \tag{9.8}$$

for $x\to+\infty$, where N and N_f represent the scaling factors for the scattering states of the original structure and the iso-spectral family of structures respectively. These two last equations directly lead to:

$$r_f=r, \tag{9.9.a}$$

$$t_f=t. \tag{9.9.b}$$

9.2. SUSY transformation optics

Figure 9.1 schematically shows that by staring from a given structure, how different variations of a secondary potential can be established by using appropriate transformations [19]. Table 9.1 on the other hand summarizes the relations between the reflection/transmission coefficients of superpartner structures in the unbroken and broken supersymmetry regime as well as the iso-spectral family of potentials. According to this table, by starting from a given structure one can construct a secondary structure with similar scattering properties. As a result SUSY transformations can be viewed as a one-

dimensional transformation optics technique since it offers several degrees of freedom for obtaining a 1D structure with desired scattering properties.

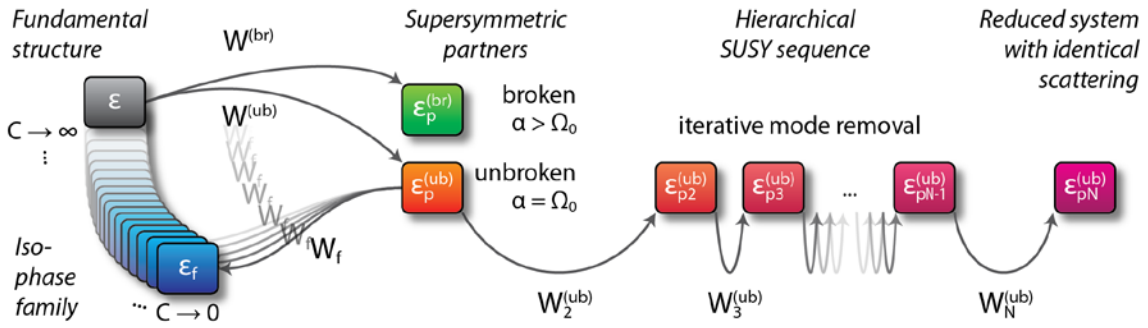

Figure 9.1. Schematic overview of the different SUSY optical transformations. Starting from a given fundamental structure ϵ, supersymmetric partners ϵ_p can be constructed. Whereas the broken SUSY system $\epsilon_p^{(br)}$ preserves all bound modes, unbroken SUSY ($\epsilon_p^{(ub)}$) removes the fundamental mode. Regardless, in both cases the intensity reflection and transmission coefficients of the superpartners are identical to those of the fundamental system. In order to maintain the full complex scattering characteristics, a family ϵ_f of iso-phase structures can be synthesized. Finally, a hierarchical sequence of higher-order superpartners $\epsilon_{p,2\ldots N}^{(ub)}$ may be utilized to obtain a scattering-equivalent structure, which requires a substantially lower refractive index contrast than that involved in the original system ϵ.

Table 9.1. Reflection and transmission coefficients for the different SUSY transformations. $\boldsymbol{W_-} = \boldsymbol{W}(\boldsymbol{X} \to -\infty)$ designates the asymptotic value of the superpotential on the left side of the structure, and $\boldsymbol{r}, \boldsymbol{t}$ are the coefficients of the original structure.

Coefficient	**Unbroken SUSY**	**Broken SUSY**	**Iso-phase**
Reflection	$r_p = r \cdot \exp\left[-2i \tan^{-1}\left(\frac{n_0 \cos\theta}{W_-}\right)\right]$	$r_p = r \cdot \exp\left[-2i \tan^{-1}\left(\frac{n_0 \cos\theta}{W_-}\right)\right]$	$r_p(C) = r$
Transmission	$t_p = t \cdot \exp\left[-2i \tan^{-1}\left(\frac{n_0 \cos\theta}{W_-}\right)\right]$	$t_p = t$	$t_p(C) = t$

Figure 9.2 depicts different SUSY transformed variations of an original potential defined as $\epsilon(X) = 1 + \exp[-(X/5)^8]$. In all cases the amplitude of the reflection and transmission coefficients are the same for all angles of incidence while in general phases are different.

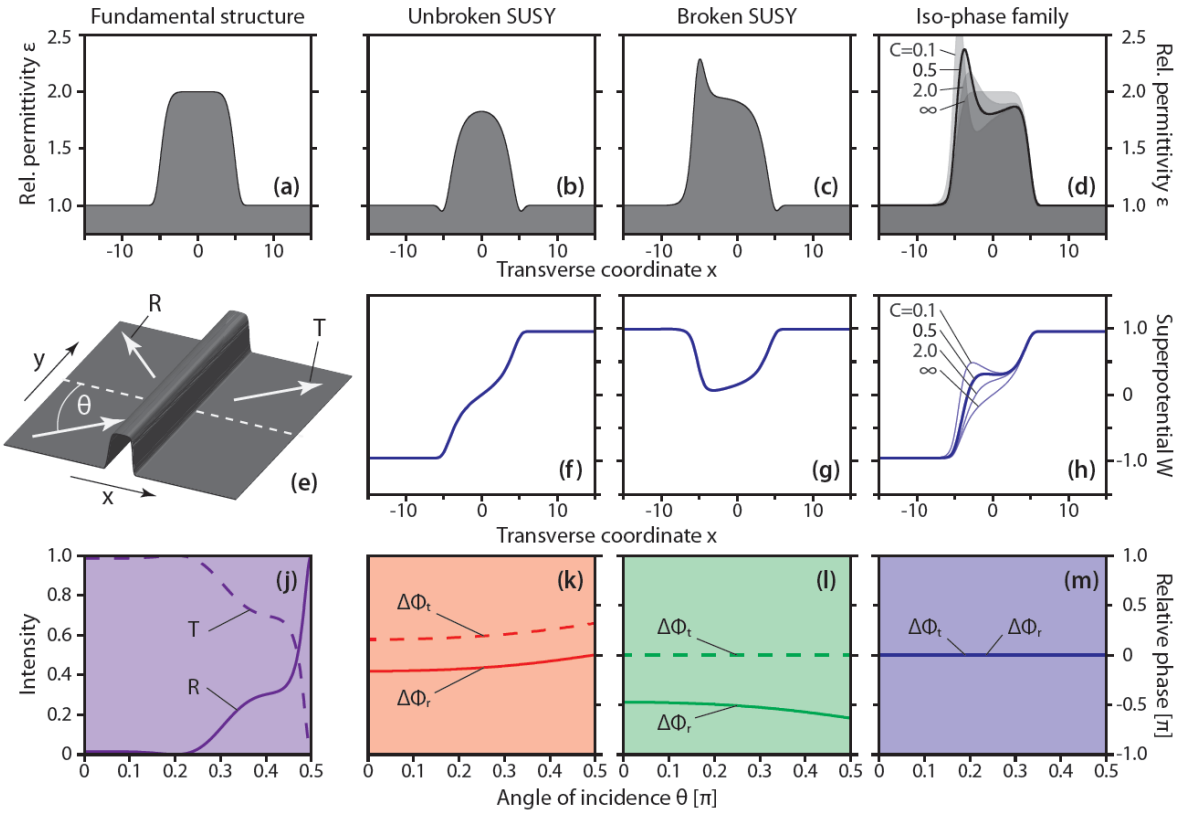

Figure 9.2. Relative permittivity distributions of the original and the transformed potentials, (a) The fundamental system has a step-like profile $\epsilon(X) = 1 + \exp[-(X/5)^8]$. (b) The superpartner in the unbroken SUSY regime, (c) The superpartner in the broken SUSY case, and (d) phase-equivalent structures. (e) Scattering geometry. (f-h) Superpotentials W corresponding to panels (b-d). (j) Identical reflectivity R (solid line) and transmittivity T (dashed line) corresponding to Figs. 1(a-d). (k-m) Relative phases of the reflection ($\Delta\Phi_r$, solid line) and transmission ($\Delta\Phi_t$, dashed) coefficients of the structures in (b-d) compared to the fundamental system (a) as a function of the incident angle θ. The scattering characteristics were evaluated by means of the differential transfer matrix method.

9.3. Wavelength dependencies of supersymmetric scattering

So far the performance of these systems has been examined at a given operating wavelength λ_0. Of importance would be to investigate to what extend their supersymmetric properties persist when the wavelength λ varies around λ_0. As one would expect, even if two dissimilar profiles exhibit the same phases at a given wavelength, their internal light dynamics may gradually undergo different changes with λ. To elucidate this structural dispersion, we provide the spectral dependence of the difference in transmittivities ΔT (or reflectivities ΔR) between the fundamental structure (Figure 9.2(a)) and its superpartners (Figure 9.2(b-d)) as a function of the incidence angle θ, as shown in Figures 9.3(a-c). As these figures indicate, this difference only becomes notable in the unbroken SUSY regime (Figure 9.3(a)), while it is almost absent under broken SUSY and iso-phase conditions (Figures 9.3(b,c)). The difference in the corresponding reflection phases is similarly presented in Figures 9.3(d-f). The dashed lines trace the abrupt phase jumps of π, which mark the resonances in the two partners and intersect at the design wavelength λ_0. Evidently, the iso-phase design displays the greatest resilience with respect to spectral deviations. Note that resonances play no role in the transmission phases, as can be seen in Figures 9.3(g-j). In this latter case, the iso-phase system again proves to be the least susceptible to spectral deviations. These results demonstrate that SUSY transformations can be robust over a broad spectral range around the design wavelength.

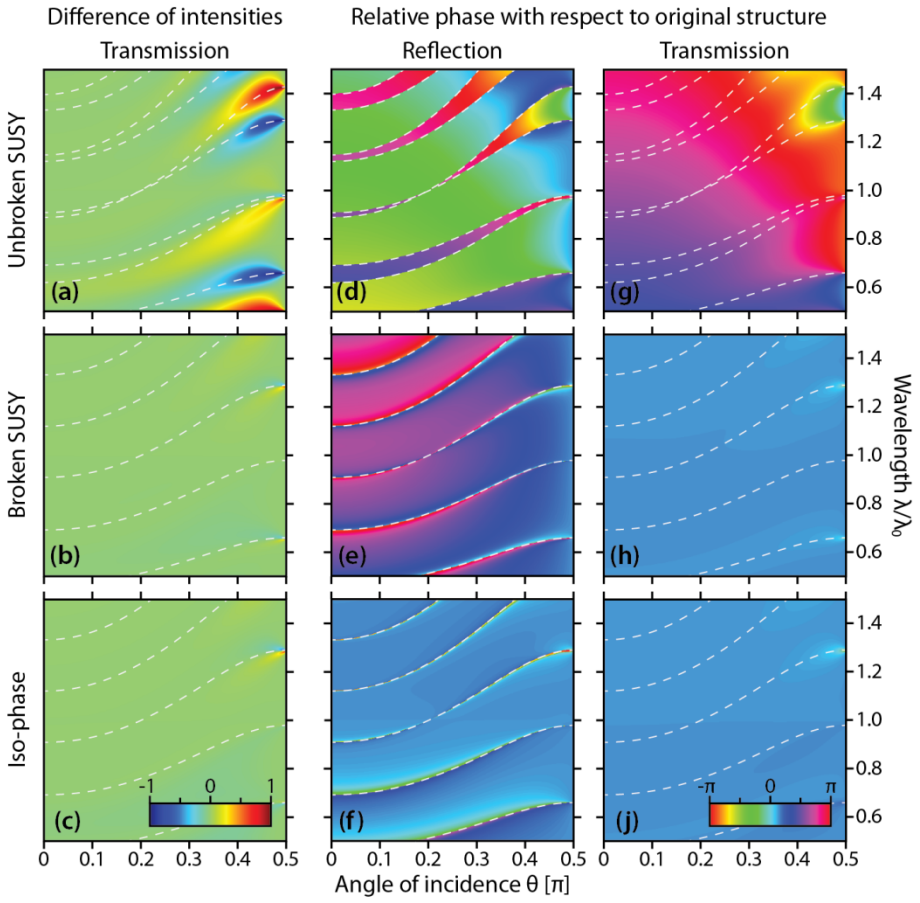

Figure 9.3. Reflection/transmission characteristics of structures obtained by SUSY transformations depicted in Figure 9.2 as function of wavelength λ and angle of incidence θ. (a-c) Intensity difference in transmission. (d-f) Relative phases in reflection and (g-j) Relative phases in transmission. The dashed lines follow the resonance-induced π phase jumps in fundamental structure and unbroken-SUSY partner. Top row: Unbroken SUSY, Middle row: Broken SUSY, bottom row: Iso-phase case ($C = 0.5$).

9.4. Index contrast reduction using SUSY

One of the main challenges in designing optical systems is the limited dynamic range of refractive indices associated with available materials. This issue becomes particularly acute when high contrast arrangements are desirable. For example, the number of grating unit cells required to achieve a certain diffraction efficiency grows with the inverse logarithm of the index contrast n_2/n_1 between the individual layers [20]. As it turns out, SUSY optical transformations can be utilized to reduce the index contrast needed for a given structure. This can be done through a hierarchical ladder of superpartners, i.e. sequentially removing the bound states of the original high-contrast arrangement (Figure 9.4(a)). As a general trend, each successive step demands less contrast in the corresponding index landscape than the previous one (Figure 9.4(b)). The ultimate result is a low-contrast equivalent structure that fully inherits the reflectivity and transmittivity of the original configuration (Figures 9.4(c,d)).

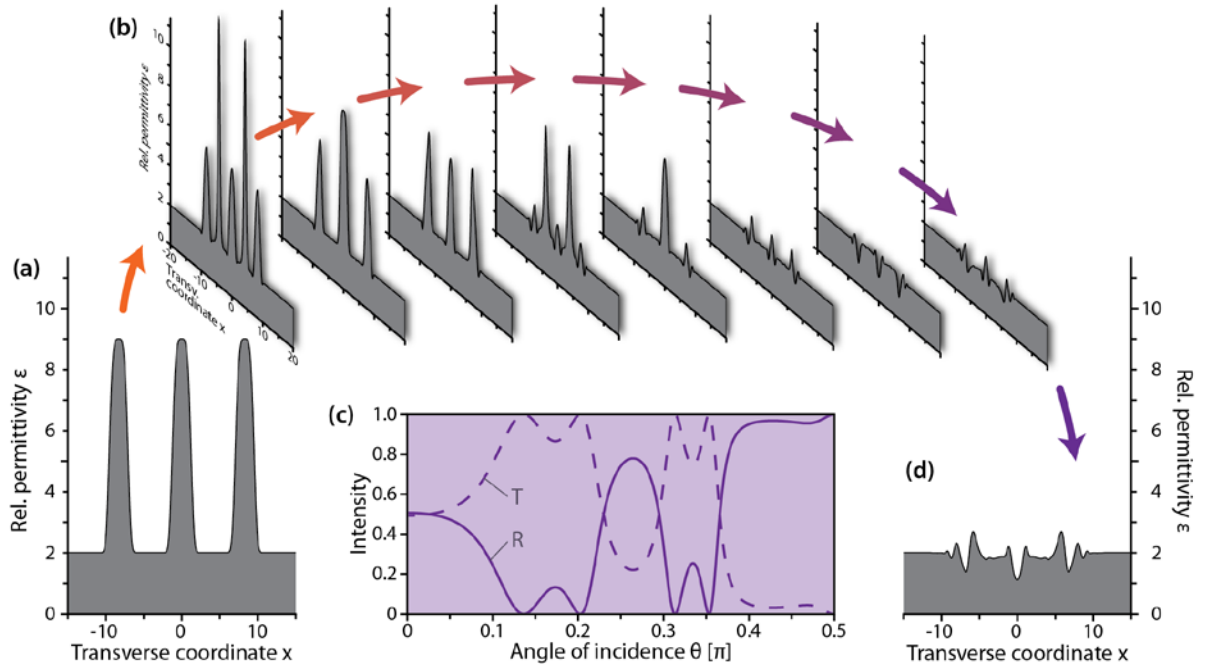

Figure 9.4. (a) Hypothetical high-contrast dielectric layer arrangement that supports $N = 9$ guided modes. (b) Hierarchical sequence of partner structures obtained through iterative SUSY transformations. (c) Despite the general trend towards lower-contrast configurations, each intermediate step inherits the reflectivity and transmittivity of the fundamental system (a). (d) The resulting low-contrast structure is free of bound states and faithfully mimics the intensity scattering characteristics of the original high-contrast configuration for all angles of incidence.

9.5. Replacing negative permittivity materials using SUSY

Finally, SUSY transformations can provide a possible avenue in replacing negative-permittivity inclusions (typically accompanied by losses) by purely dielectric materials. In this respect, inverse SUSY transformations, which now add modes with certain propagation constants to a given structure, can instead be used to locally elevate the permittivity (see supplementary information). Along similar lines, it is possible to find superpotentials that relate a structure with metallic or negative permittivity regions to an equivalent arrangement with entirely positive ϵ, as depicted in Figure 9.5. Here we make use of the fact that in a broken-SUSY transformation, the spatial average of ϵ happens to be a conserved quantity. Therefore, changes in the broader vicinity of the original metal-dielectric structure can be used to achieve this goal.

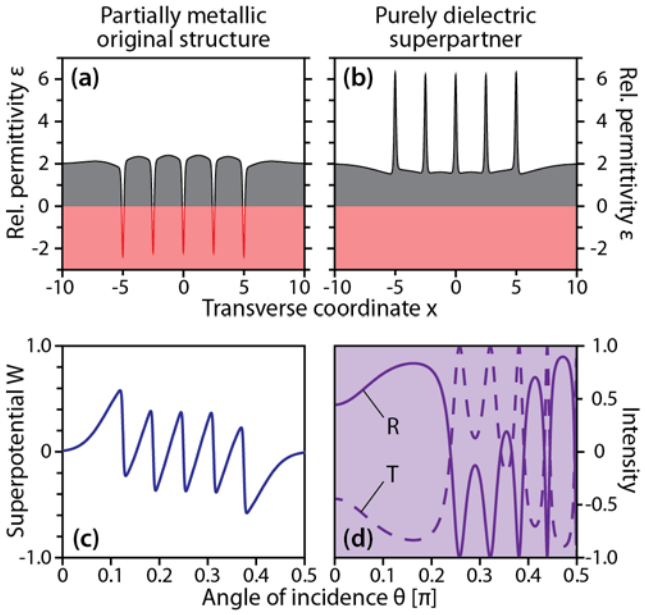

Figure 9.5. (a) A metal-dielectric grating arrangement comprising five layers of negative electrical permittivity (red sections). (b) An entirely dielectric superpartner grating constructed in the broken SUSY regime, using the respective superpotential (c). (d) Despite the absence of any metallic regions, the equivalent structure exhibits identical reflectivities/transmittivities.

9.6. References

1. I. Kay and H.E. Moses, Reflectionless transmission through dielectric scattering potentials, J. Appl. Phys. **27**, 1503 (1956).

2. E. Wolf, "Three-dimensional structure determination of semi-transparent objects from holographic data", Opt. Commun. **1**, 153 (1969).

3. A. J. Devaney, “Inverse-scattering theory within the Rytov approximation”, Opt. Lett. **6**, 374 (1981).

4. H. E. Moses, “Calculation of the Scattering Potential from Reflection Coefficients”, Phys. Rev. **102**, 559 (1956).

5. K. Chadan and P. C. Sabatier, “*Inverse Problems in Quantum Scattering Theory*,” Springer, New York, (1977).

6. I. M. Gel’fand, and B. M. Levitan, “On the determination of a differential equation from its spectral function”, Izvest. Akad. Nauk, **15**, 309 (1951).

7. P. Deift and E. Trubowitz, “Inverse scattering on the line”, Commun. Pure Appl. Math. XXXII, 121 (1979).

8. F. Cooper, A. Khare, and U. Sukhatme, “Supersymmetry and quantum mechanics”, Phys. Rep. **251**, 267 (1995).

9. A. Lahiri, P. Roy, and B. Bagchi, “Supersymmetry in quantum mechanics”, Int. J. Mod. Phys. A **5**, 1383 (1990).

10. A. Khare and U. Sukhatme, “Phase-equivalent potentials obtained from supersymmetry”, J. Phys. A: Math. Gen. **22**, 2847 (1989).

11. M. M. Nieto, “Relationship between supersymmetry and the inverse method in quantum mechanics”, Phys. Lett. B **145**, 208 (1984).

12. C. V. Sukumar, “Supersymmetric quantum mechanics and the inverse scattering method”, J. Phys. A: Math. Gen. **18**, 2937 (1985).

13. J. B. Pendry, D. Shurig, and D. R. Smith, “Controlling electromagnetic fields”, Science **312**, 1780 (2006).

14. U. Leonhardt, “Optical conformal mapping”, Science **312,** 1777 (2006).

15. Y. Lai, J. Ng, H. Y. Chen, D. Z. Han, J. J. Xiao, Z.-Q. Zhang, and C. T. Chan, “Illusion optics: the optical transformation of an object into another object”, Phys. Rev. Lett. **102**, 253902 (2009).

16. E. E. Narimanov, and A. V. Kildishev, “Optical black hole: Broadband omnidirectional light absorber”, Appl. Phys. Lett. **95**, 041106 (2009).

17. N. Kundtz, and D. R. Smith, “Extreme-angle broadband metamaterial lens”, Nat. Mater. **9**, 129 (2010).

18. H. Chen, C. T. Chan, and P. Sheng. “Transformation optics and metamaterials”, Nat. Mater. **9**, 387 (2010).

19. M.-A. Miri, M. Heinrich, and D. N. Christodoulides, “SUSY-inspired one-dimensional transformation optics”, Optica **1**, 89 (2014).

20. P. Yeh, “*Optical Waves in Layered Media*,” Wiley, New York (1988).

CHAPTER TEN: SUPERSYMMETRY AND COMPLEX POTENTIALS

In this section we explore the ramifications of supersymmetry in the context of complex optical potentials [1-8]. First we consider PT-symmetric potentials only and we show that the SUSY formalism allows for the construction of partner structures where the fundamental mode, or any other higher order bound state, can be removed at will [9]. We then investigate iso-spectral families of non-Hermitian index landscapes that share the exact same spectrum starting from a PT-symmetric configuration. Through this approach, one can synthesize optical structures where the guided modes experience zero net gain and loss despite of the fact that their shape violates PT-symmetry. In addition, refractive index profiles with spontaneously broken PT symmetry are investigated. Here, the contrast between gain and loss is sufficiently strong as to prevent their mutual compensation in the overlap of a guided mode. In this case it is shown that removing the resulting pair of complex conjugate modes by means of SUSY leads to a PT-symmetric potential without spontaneous symmetry breaking.

10.1. SUSY formalism in PT-symmetric optical potentials

Let us first consider how the notion of supersymmetry can be applied in complex optical potentials. As previously discussed the SUSY formalism can be generally used in arbitrary

one-dimensional refractive index landscapes. In fact, this is the case even under high-contrast conditions where the degeneracy between TE and TM waves is broken and necessitates the use of the Helmholtz equation. Here, for brevity, we limit the scope of our work to one-dimensional weakly guiding settings. In this regime, the beam dynamics can be described within the paraxial approximation. In our system $n(x) = n_0 + \Delta n(x)$ describes the refractive index distribution in the transverse coordinate x, where the index modulation $\Delta n(x)$ is assumed to be weak compared to the background index n_0, $\Delta n(x) \ll n_0$. Under these conditions one finds that the slowly varying envelope U of the electric field component $E(x,z) = U(x,z)e^{ik_0 n_0 z}$ satisfies the following evolution equation:

$$i\frac{\partial U}{\partial Z} + \frac{\partial^2 U}{\partial X^2} + V(X)U = 0. \tag{10.1}$$

Here the normalized transverse and longitudinal coordinates are respectively given by $X = x/x_0$ and $Z = z/(2k_0 n_0 x_0^2)$, where x_0 is an arbitrary length scale, and $k_0 = 2\pi/\lambda_0$ is the wave number corresponding to the free space wavelength λ_0. The optical potential $V(x)$ is directly proportional to the refractive index variation,

$$V = 2k_0^2 n_0 x_0^2 \Delta n(x) \tag{10.2}$$

and in general is complex, $V = V_R + V_I$, where the real part $V_R(X)$ is the outcome of index modulation, while the imaginary part $V_I(X)$ indicates the presence of gain or loss. Looking for stationary (modal) solutions of the form $U(X,Z) = \psi(X) \cdot e^{i\mu Z}$, we then obtain the following Schrödinger eigenvalue problem:

$$H\psi = -\mu\psi, \tag{10.3}$$

where the operator $H = -\frac{d^2}{dX^2} - V(X)$ represents the Hamiltonian of the optical configuration and μ the respective eigenvalue.

We now assume that a given potential $V^{(1)}$ supports at least one guided optical mode $\psi_1^{(1)}(X)$ with a corresponding eigenvalue $\mu_1^{(1)}$. Following the approach detailed in [10], one can then factorize the Hamiltonian as $H^{(1)} + \mu_1^{(1)} = BA$ with

$$A = +\frac{d}{dX} + W, \tag{10.4.a}$$

$$B = -\frac{d}{dX} + W. \tag{10.4.b}$$

Note that, whereas in Hermitian systems described by a real-valued superpotential $W(X)$ the two operators $B = A^\dagger$ form a Hermitian-conjugate pair, this is no longer true in the general case of a complex W.

Defining a partner Hamiltonian as $H^{(2)} + \mu_1^{(1)} = AB$, one quickly finds that the optical potentials of original and the partner system can both be generated from the superpotential and its transverse derivative:

$$V^{(1,2)}(X) = \mu_1^{(1)} - W^2 \pm W' \tag{10.5}$$

It readily follows that the two optical potentials $V^{(1,2)}$ then share a common set of eigenvalues:

$$\mu_m^{(1)} = \mu_{m-1}^{(2)} \quad \forall \; m \geq 2. \tag{10.6}$$

The only exception is the fundamental mode of $V^{(1)}$, which lacks a counterpart in $V^{(2)}$. Note that this SUSY mode partnership is not limited to the discrete sets of bound states, but rather extends to the continua of radiation modes of both structures. The operators A and B also provide a link between the wave functions of the two potentials:

$$\psi_m^{(2)} = A\psi_{m+1}^{(1)} \tag{10.7.a}$$

$$\psi_{m+1}^{(1)} = B\psi_m^{(2)}. \tag{10.7.b}$$

In order to derive an expression for the superpotential, we make use of the fact the A should annihilate the fundamental mode of the first potential; $A\psi_1^{(1)} = 0$. Therefore, by using Equation 10.4(a), W can be written as a logarithmic derivative of the fundamental mode's wave function:

$$W = -\frac{d}{dX}\ln\left(\psi_1^{(1)}\right), \tag{10.8}$$

Similarly, the partner potential $V^{(2)}$ can be expressed in terms of $V^{(1)}$ and $\psi_1^{(1)}$ as follows:

$$V^{(2)} = V^{(1)} + 2\frac{d^2}{dX^2}\ln\left(\psi_1^{(1)}\right) \tag{10.9}$$

We now apply this formalism when $V^{(1)}$ is PT-symmetric, i.e. $V^{(1)}(-X) = \left(V^{(1)}(X)\right)^*$. At this point we also assume that the symmetry of $V^{(1)}$ is not spontaneously broken. Under these conditions, the eigenvalue spectrum is real-valued, i.e. $Im\left(\mu_m^{(1)}\right) = 0$, and the individual modes inherit the potential's symmetry: $\psi_m^{(1)}(-X) = \left(\psi_m^{(1)}\right)^*$. Following Eq. (10.8), one then concludes that the superpotential should be anti-PT-symmetric:

$W^*(-X) = -W(X)$. On the other hand, Eq. (10.9) clearly shows that $V^{(2)}$ again respects the condition of PT symmetry. Since SUSY dictates that its spectrum is also real-valued, it follows that PT symmetry is unbroken in the partner potential.

Figure 10.1 illustrates the implications of supersymmetry when for example a PT-symmetric multimode waveguide is considered, that has the refractive index profile

$$\Delta n^{(1)}(x) = \delta \cdot \left(1 + i\gamma \tanh \frac{x}{0.2\lambda_0}\right) \cdot \exp\left(-\left(\frac{x}{0.8\lambda_0}\right)^8\right) \qquad (10.10)$$

Here, the index elevation is $\delta = 4.2 \times 10^{-2}$ and the imaginary gain/loss contrast is $\gamma = 0.1$. This waveguide supports a total of four guided modes at a wavelength of $\lambda_0 = 10^{-6}$ m. The figure shows the real- and imaginary parts of the refractive index profile as well as the absolute value $\left|\psi_m^{(1)}\right|$ of the modal distributions (Fig. 10.1(a)). The corresponding superpartner waveguide and its three guided modes are depicted in Fig. 10.1(b), and the eigenvalue spectra of both structures are compared in Fig.1c. Note that none of the PT-symmetric modes exhibit any nodes in their intensity profile.

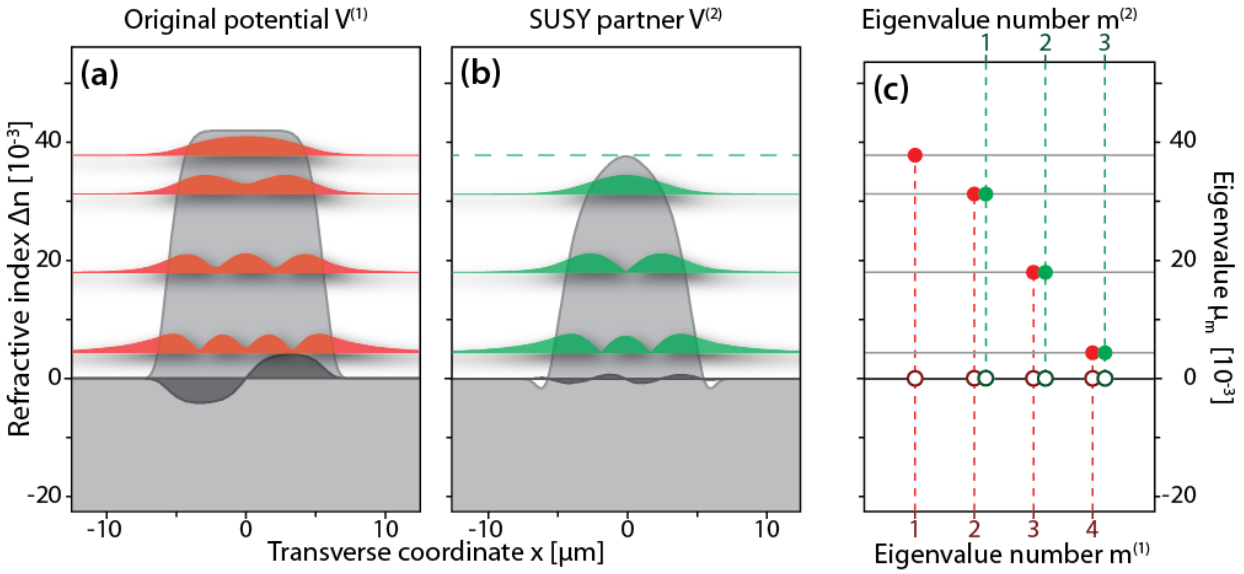

Figure 10.1. (a) Refractive index profile (real part: light gray / imaginary part: dark gray area) of a PT-symmetric multimode waveguide supporting a total of four bound states (shown absolute values $\left|\psi_m^{(1)}\right|$ at the vertical positions corresponding to their respective eigenvalues $\mathrm{Re}\left(\mu_m^{(1)}\right)$. (b) Corresponding SUSY partner and its three modes. (c) Eigenvalue spectra of the two structures $\mathrm{Re}\left(\mu_m^{(1,2)}\right)$ are shown as full circles, whereas empty circles denote $\mathrm{Im}\left(\mu_m^{(1,2)}\right)$.

10.2. Removal of higher modes

In Hermitian systems, all modes except for the fundamental state exhibit nodes where the absolute value of the wave function vanishes. Given that the superpotential W as

constructed from Eq. (10.8) relies on the logarithmic derivative of an eigenfunctions $\psi_m^{(1)}$, in this case one can only use the nodeless ground state $\psi_1^{(1)}$. In contrast, the zeros of the real and imaginary parts of modes associated with non-Hermitian systems do not occur at the same positions. This peculiar behavior now allows one to use any higher order mode $\psi_m^{(1)}$ (see Figure 10.2(a)) in constructing a SUSY partner, i.e. by removing the eigenvalue $\mu_m^{(1)}$ from the spectrum. In other words,

$$\bar{V}^{(1,2)}(X) = \mu_m^{(1)} - \bar{W}^2 \pm \bar{W}' \tag{10.11.a}$$

$$\bar{W} = -\frac{d}{dX}\ln\left(\psi_m^{(1)}\right) \tag{10.11.b}$$

The relations between eigenvalues and wave functions for these two structures then can be written as

$$\mu_m^{(1)} = \mu_m^{(2)} \quad \forall \quad m < m_0 \ , \ \mu_m^{(1)} = \mu_{m-1}^{(2)} \quad \forall \quad m > m_0 \tag{10.12.a}$$

$$\psi_m^{(2)} = A\psi_m^{(1)} \ , \quad \psi_m^{(1)} = B\psi_m^{(2)} \quad \forall \ m < m_0 \tag{10.12.b}$$

$$\psi_m^{(2)} = A\psi_{m+1}^{(1)} \ , \quad \psi_{m+1}^{(1)} = B\psi_m^{(2)} \quad \forall \ m > m_0 \tag{10.12.c}$$

respectively.

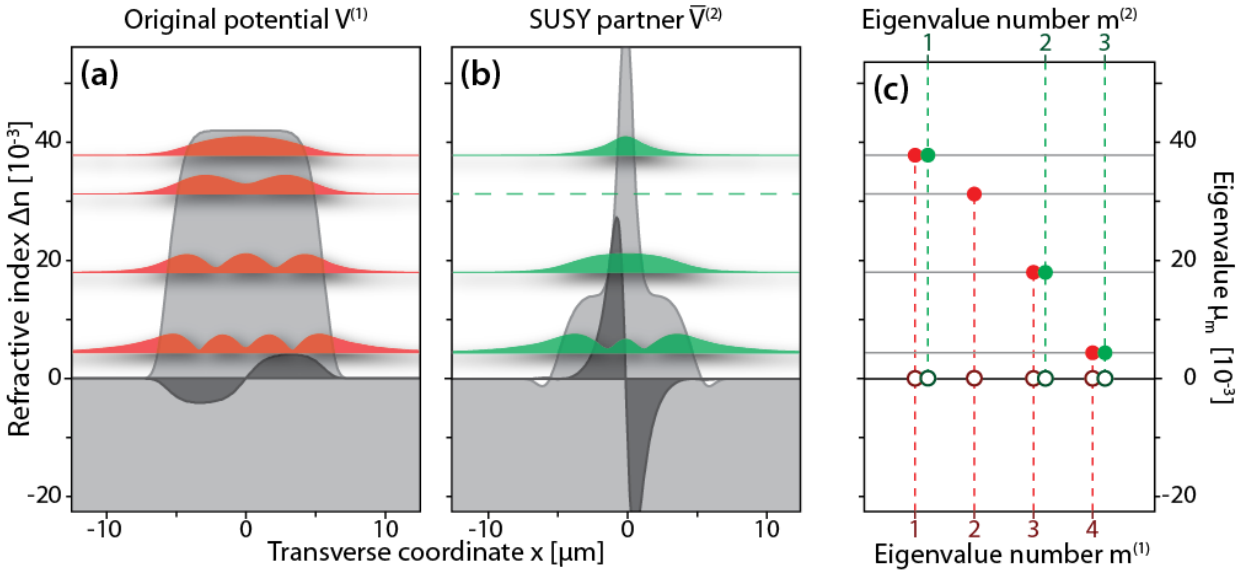

Figure 10.2. (a) Refractive index profile of a PT-symmetric multimode waveguide supporting a total of four bound states, as in Figure 10.1. (b) Corresponding SUSY partner where the second mode has been removed from the original waveguide. (c) Eigenvalue spectra of the two structures.

Figure 10.2 illustrates the removal of the eigenvalue associated with the second mode from the spectrum of the multimode waveguide discussed in Figure 10.2(a) Again the SUSY partner potential (Figure 10.2(b)) supports three modes, which now are matched to the eigenvalues of the first, third and fourth mode of the original structure. Note that the partner waveguide has been most strongly altered in regions where the removed state had an intensity minimum. There, the second derivative of the wave function's absolute value is maximal, resulting in a pronounced feature in the SUSY partner. In the Hermitian limit $Im(\Delta n^{(1)}) \rightarrow 0$, this feature is transformed into a singularity.

10.3. SUSY in structures with spontaneously broken PT-symmetry

In this section we investigate SUSY in systems with spontaneously broken PT symmetry. When the contrast between gain and loss exceeds a certain limit, a given real refractive index profile can no longer maintain the symmetry of the bound states. For our example waveguide profile, an imaginary contrast of $\gamma = 0.2$ places the system well inside this broken-symmetry regime (see Figure 10.3(a)). As it is expected for this type of complex potential, the eigenvalues of the lowest two modes are transformed into a complex conjugate pair with identical real parts $Re\left(\mu_1^{(1)}\right) = Re\left(\mu_2^{(1)}\right)$ and opposite imaginary parts $Im\left(\mu_1^{(1)}\right) = -Im\left(\mu_2^{(1)}\right)$. The corresponding states reside predominantly on the gain (loss) region. Note that the remaining higher order modes retain their PT symmetry, and therefore continue to exhibit an entirely real spectrum.

Following the previously established formalism, SUSY allows us to remove one of the broken-symmetry modes (Figure 10.3(b)). As in the case of unbroken PT symmetry, SUSY preserves the remaining set of eigenvalues. In our example the partner waveguide supports two neutral modes as well as the remaining amplified mode as fundamental state. Removing the latter by means of SUSY restores the symmetry of the underlying structure (Figure 10.3(c)) and yields a waveguide with unbroken PT symmetry that is perfectly phase matched to the two neutral modes of the original system (Figure 10.3(d)).

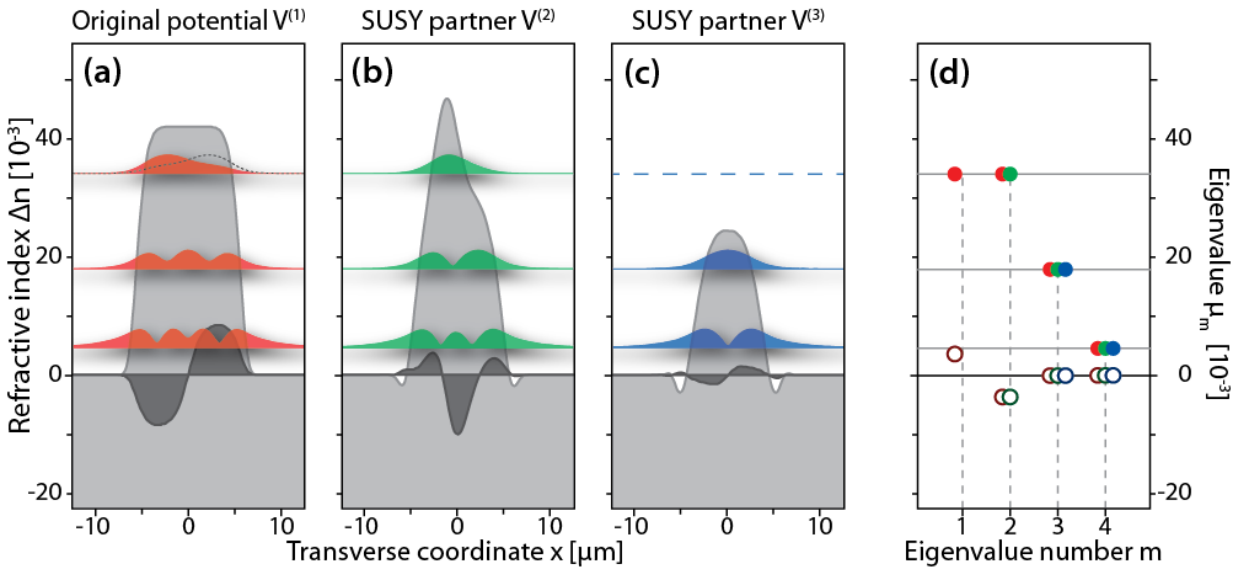

Figure 10.3. (a) Refractive index profile of a multimode waveguide supporting a total of 4 bound states. Here, the imaginary contrast was increased to $\gamma = 0.2$ to induce spontaneous PT symmetry breaking of the two lowest states. Removing the attenuated (b) and the amplified (c) mode by means of SUSY restores PT symmetry to the structure (d).

10.4. One-parameter family of non-PT potentials with real spectra

In this section we will focus our attention on synthesizing complex, non-PT-symmetric potentials that support entirely real-valued spectra. In the context of nonrelativistic SUSY quantum mechanics, it is known that one can establish whole isospectral families of potentials sharing the spectrum of a given "parent" potential. Here we will show that this

approach can be adapted to find optical potentials, which are iso-spectral to a PT-symmetric potential.

Consider again a PT-symmetric potential with at least one guided mode and otherwise arbitrary shape. According to Equation (10.5) (for the partner potential) the superpotential satisfies the well-known Riccati equation $V^{(2)}(X) = \mu_m^{(1)} - W^2 - W'$. A general solution of this equation $\widetilde{W}$ can be written in terms of the particular solution W found in Equation (10.8) as [10]: $\widetilde{W} = W + \frac{1}{v}$ where v satisfies the first order equation $\frac{d}{dX}v = 1 + 2Wv$. By using W given in Eq. (10.8), the solution of this equation can be written as $v(x) = \left(\psi_m^{(1)}(X)\right)^{-2}\left(C + \int_{-\infty}^{X}\left(\psi_m^{(1)}(X')\right)^2 dX'\right)$, resulting in the following parametric family of superpotentials:

$$\widetilde{W} = W + \frac{d}{dX}\ln\left(C + \int_{-\infty}^{X}\left(\psi_m^{(1)}(X')\right)^2 dX'\right) \tag{10.13}$$

and the corresponding isospectral family of complex optical potentials

$$\tilde{V}^{(1)} = V^{(1)} + 2\frac{d^2}{dX^2}\ln\left(C + \int_{-\infty}^{X}\left(\psi_m^{(1)}(X')\right)^2 dX'\right) \tag{10.14}$$

In order to avoid singular behavior, the parameter C can be freely chosen in a range that makes a nonzero denominator. Note that the superpotential corresponding to each value of the parameter C can be used to construct a potential $\tilde{V}^{(2)}$ that is isospectral to the superpartner $V^{(2)}$, and therefore constitutes a valid superpartner of $V^{(1)}$ in its own right.

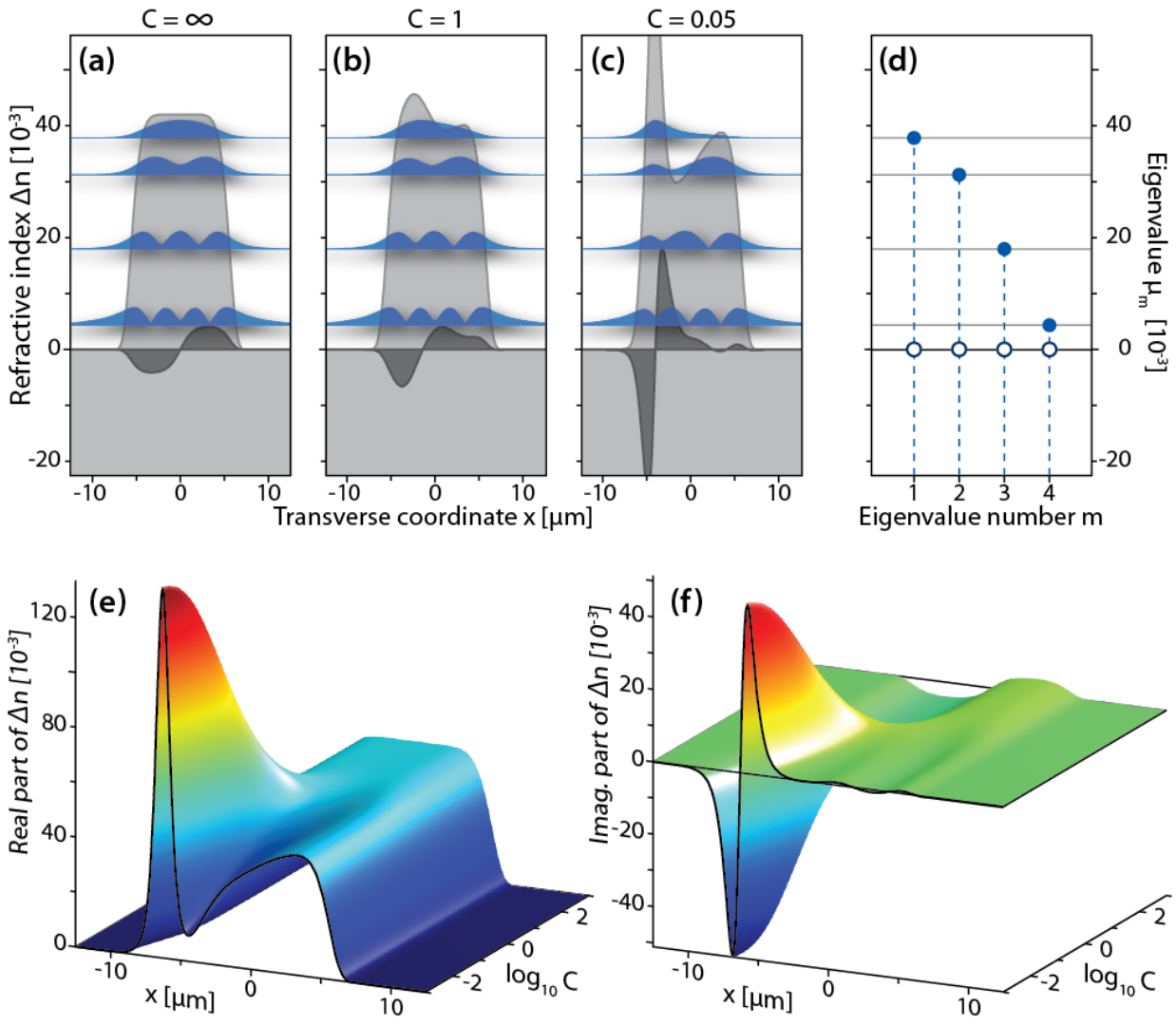

Figure 10.4. (a) Refractive index profile of a PT-symmetric multimode waveguide supporting a total of 4 bound states. For $C \to \infty$, the parametric family converges toward this parent potential. As C approaches 0, the potentials and their guided modes become visibly distorted (b,c). Regardless, all members of the family share the exact same eigenvalue spectrum (d,e). Shape of the real- and imaginary of the isospectral family for continuously varying C.

Obviously, the members of an isospectral family constructed from a PT-symmetric original potential according to Equation (10.14) generally do not retain a PT symmetric shape, i.e. $\tilde{V}^*(-X) \neq \tilde{V}(X)$ (see Figure 10.3(a-c)). Nevertheless, as long as PT symmetry is not spontaneously broken in the parent potential, the identical spectra of all family members will be entirely real-valued (Figure 10.3(d)).

A closer look at the shape of the respective eigenstates reveals the mechanism behind this unexpected behavior. Even though the gain/loss is no longer symmetrically distributed across the waveguide's profile (Figure 10.3(f)), the real part is deformed (Figure 10.3(e)) such that the redistributed mode profiles can maintain a neutral imaginary overlap. To confirm this intuitive explanation, consider again the paraxial equation governing the eigenmodes of a waveguide, and its complex conjugate:

$$\frac{d^2\tilde{\psi}}{\partial X^2} + \tilde{V}(X)\tilde{\psi} = \mu\tilde{\psi} \tag{10.15.a}$$

$$\frac{d^2\tilde{\psi}^*}{\partial X^2} + \tilde{V}^*(X)\tilde{\psi}^* = \mu^*\tilde{\psi}^* \tag{10.15.b}$$

After multiplying these equations by μ and μ^* respectively, their difference yields:

$$\tilde{\psi}^*\frac{d^2\tilde{\psi}}{dX^2} - \tilde{\psi}\frac{d^2\tilde{\psi}^*}{dX^2} + \left(\tilde{V} - \tilde{V}^*\right)\left|\tilde{\psi}\right|^2 = (\mu - \mu^*)\left|\tilde{\psi}\right|^2 \tag{10.16}$$

The first term represents a total differential. With a real eigenvalue $\mu^* = \mu$, we therefore find

$$\frac{d}{dX}\left(\tilde{\psi}^*\frac{d}{dX}\tilde{\psi} - \tilde{\psi}\frac{d}{dX}\tilde{\psi}^*\right) + 2\left|\tilde{\psi}\right|^2 \cdot Im(\tilde{V}) = 0. \tag{10.17}$$

Taking into account that the bound states decay exponentially outside the guiding region and vanish at infinity, integration over the entire X axis yields

$$\int_{-\infty}^{+\infty} Im(\tilde{V}) \cdot \left|\tilde{\psi}\right|^2 dX = 0. \tag{10.18}$$

Moreover, a direct integration over the imaginary part of the potential shows that a transformation according to Equation (10.18) does not introduce any changes to the overall gain/loss of the system. Using the fact that imaginary part of the PT-symmetric parent potential $V^{(1)}$ itself is anti-symmetric, one finds

$$\int_{-\infty}^{+\infty} Im(\tilde{V}) dX = 2Im\left\{\frac{d}{dX}\ln\left(C + \int_{-\infty}^{X}\left(\psi_m(X')\right)^2 dX'\right)\right\}\Big|_{-\infty}^{+\infty} = 0. \tag{10.19}$$

10.5. SUSY and general families of non-Hermitian potentials with real spectra

In this section by considering general relations between superpartners we show that a more general class of non-Hermitian potentials that can have entirely real spectra. As we will see PT-symmetric potentials form only a specific class of such potentials. Let us consider again the general superpartner potentials defined in the previous chapters:

$$V = \alpha - W^2 + W' \tag{10.20.a}$$

$$V_p = \alpha - W^2 - W' \tag{10.20.b}$$

Assuming that Now assume the general complex superpotentials:

$$W = W_R + iW_I \tag{10.21}$$

As a result the two superpartners can be written as:

$$V = \alpha - W_R^2 + W_I^2 + W_R' + i(-2W_R W_I + W_I') \tag{10.22.a}$$

$$V_p = \alpha - W_R^2 + W_I^2 - W_R' + i(-2W_R W_I - W_I') \tag{10.22.b}$$

Assuming that the broken supersymmetry regime, these two complex optical potentials will share the exact same eigenvalue spectra. Now of interest would be to find special cases where one of the two partners becomes real and the other one complex. In that case a complex potential will have a real superpartner and as a result it will have a completely real spectra. Assume a particular superpotential which satisfies the relation:

$$W_I' = 2W_R W_I \tag{10.23}$$

This selection leads to:

$$V = \alpha - W_R^2 + W_I^2 + W_R' \tag{10.24.a}$$

$$V_p = \alpha - W_R^2 + W_I^2 - W_R' - i2W_I' \tag{10.24.b}$$

Obviously the first potential is real therefore the complex superpartner can have real spectra. In summary any complex potential of the form:

$$V = \alpha - \left(\frac{g'}{2g}\right)^2 - \left(\frac{g'}{2g}\right)' + g^2 - i2g' \tag{10.25}$$

where $g(x)$ is a real non-zero function can exhibit entirely real spectra. Note that when $g(x)$ is even, V becomes PT-symmetric. On the other hand in general, the optical potential of Equation (10.25) does not satisfy any type of symmetry.

10.6. References

1. F. Cannata, G. Junker, and J. Trost, "Schrödinger operators with complex potential but real spectrum," Phys. Lett. A. **246**, 219 (1998).

2. A. A. Andrianov, M. V. Ioffe, F. Cannata, and J.-P. Dedonder, "SUSY quantum mechanics with complex superpotentials and real energy spectra," Int. J. Mod. Phys. A **14**, 2675 (1999).

3. B. Bagchi, F. Cannata, and C. Quesne, "PT-symmetric sextic potentials," Phys. Lett. A. **269**, 79 (2000).

4. M. Znojil, F. Cannata, B. Bagchi, and R. Roychoudhury, "Supersymmetry without hermiticity within PT symmetric quantum mechanics," Phys. Lett. B **483**, 284 (2000).

5. P. Dorey, C. Dunning, and R. Tateo, "Supersymmetry and the spontaneous breakdown of PT symmetry," J. Phys. A: Math. Gen. **34**, L391 (2001).

6. F. Cannata, M. Ioffe, R. Roychoudhury, and P. Roy, "A new class of PT-symmetric Hamiltonians with real spectra," Phys. Lett. A **281**, 305 (2001).

7. G. Levai and M. Znojil, "The interplay of supersymmetry and PT symmetry in quantum mechanics: a case study for the Scarf II potential," J. Phys. A: Math. Gen. **35**, 8793 (2002).

8. D. Bermudez and D. J. Fernndez C., "Non-hermitian Hamiltonians and the Painlevé IV equation with real parameters," Phys. Lett. A. **375**, 2974 (2011).

9. M.-A. Miri, M. Heinrich, and D. N. Christodoulides, "Supersymmetry-generated complex optical potentials with real spectra," Phys. Rev. A **87**, 043819 (2013).

10. F. Cooper, A. Khare, and U. Sukhatme, “Supersymmetry and quantum mechanics,” Phys. Rep. **251**, 267385 (1995).

CHAPTER ELEVEN: CONCLUSIONS

In this dissertation we explored two major classes of symmetries, namely PT symmetry and supersymmetry, in the framework of classical optics. Even though both theories are originated and developed in quantum field theories and then quantum mechanics, due to the similarity of the governing equations, such ideas can be directly transferred into optics.

PT-symmetric optical structures by employing balanced regions of gain and loss, in addition to their refractive index profiles, exhibit interesting properties which cannot be obtained in traditional Hermitian structures. Here we proposed a new method for achieving single mode lasing operation in dielectric laser cavities. We also studied the effect of anti-symmetric gain/loss profile in periodic structures and in particular in optical mesh lattices. Furthermore we considered scattering properties of PT symmetric particles and we showed that such entities can controllably deflect the scattered light.

In the second part of this work, guided wave and scattering properties of supersymmetric structures were investigated. Supersymmetry can be utilized as a versatile means for engineering guide mode spectra of optical waveguides thus allowing for a new class of mode filters and mode multiplexers. Along these lines the first experimental demonstration of supersymmetric photonic lattices was reported in femtosecond laser-written array of glass waveguides. Finally we showed that, supersymmetry can also be utilized as a new type of transformation optics.

APPENDIX A: COUPLED MODE THEORY OF PT MICRO-RING RESONATORS

Coupled mode theory has been widely used to describe the directional coupler composed of two straight and uniformly coupled dielectric optical waveguides [1]. For PT-symmetric waveguide coupler when one waveguide involves gain and the other loss, the Hermitian coupled mode analysis can still be used with adding gain and loss coefficients as first order correction terms. Coupled mode analysis has also been widely used to describe coupling between micro-ring resonators [2]. Here we find a relation between the coupled mode parameters of PT micro-ring resonators and that of their corresponding straight waveguides. For the straight PT coupler:

$$\frac{da}{dz} = i\beta_0 a + i\kappa b + ga \tag{A1.a}$$

$$\frac{db}{dz} = i\beta_0 b + i\kappa a - gb \tag{A1.b}$$

On the other hand for two PT micro-ring resonators:

$$\frac{dA}{dt} = -i\omega_0 A + i\mu B + \gamma A \tag{A2.a}$$

$$\frac{dB}{dt} = -i\omega_0 B + i\mu A - \gamma B \tag{A2.b}$$

Evidently the resonance frequencies of each ring is obtained through the propagation constant of the corresponding waveguide as:

$$\beta_0(\omega_0)R \approx m \tag{A3}$$

The coupling coefficients are on the other hand related via:

$$\mu = v_g \kappa \frac{L_{\text{eff}}}{2\pi R} \tag{A4}$$

where v_g represents the group velocity of light inside the mico-ring resonator and L_{eff} shows an effective length to be calculated later. The gain/loss coefficinets can also be related through:

$$\gamma = v_g g. \tag{A5}$$

Equations (A4) and (A5) directly lead to:

$$\frac{\gamma/\mu}{g/\kappa} = \frac{2\pi R}{L_{\text{eff}}} > 1, \tag{A6}$$

As a result in a PT-symmetric arrangement of coupled ring resonator the gain to coupling ration is enhanced by a factor that is proportional to the size of the ring. Therefore PT-symmetry breaking can be observed at lower thresholds in coupled ring resonators compared to coupled waveguides [3].

A1. Effective coupling length

In order to calculate the effective coupling length, consider two coupled passive curved waveguides as depicted in Figure A1.

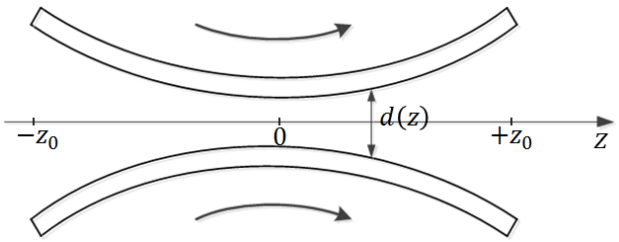

Figure A1. Non-uniform coupling along two curved waveguides

In this case the evolution of light in the two waveguides can be described by coupled mode equations with a z-dependent coupling coefficient:

$$\frac{da}{dz} = i\kappa(z)b, \tag{A7.a}$$

$$\frac{db}{dz} = i\kappa(z)a. \tag{A7.b}$$

After using the following transformation:

$$\eta = \int_{z_0}^{z} \kappa(z')dz', \tag{A8}$$

Equations (A8) can be converted to a constant coupling equation as:

$$\frac{da}{d\eta} = ib, \tag{A9.a}$$

$$\frac{db}{d\eta} = ia. \tag{A9.b}$$

Therefore the solution of the no-uniform coupler of Figure A1 can be written as:

$$a(z) = \ a_0 \cos\left(\int_{-z_0}^{z} \kappa(z')\, dz'\right) \ + \ b_0 \sin\left(\int_{-z_0}^{z} \kappa(z')\, dz'\right), \tag{A10.a}$$

$$b(z) = -ia_0 \sin\left(\int_{-z_0}^{z} \kappa(z')\,dz'\right) - ib_0 \cos\left(\int_{-z_0}^{z} \kappa(z')\,dz'\right). \quad \text{(A10.b)}$$

Comparing this to the solution of the standard coupled mode equations with a constant coupling coefficient, one can deduce that $\kappa L_{\text{eff}} = \int_{-z_0}^{z} \kappa(z')\,dz'$. Therefore the effective coupling length as:

$$L_{\text{eff}} = \frac{1}{\kappa_{\max}} \int_{-z_0}^{+z_0} \kappa(z)\,dz \quad \text{(A11)}$$

On the other hand the coupling coefficient between two waveguides decreases exponentially by increasing the distance between the two guides [2]. Therefore assuming a distance of d between the two guides the coupling constant will be $\kappa(d) = \kappa_{\max} \exp(-pd)$. On the other hand from Figure A1 we have $d(z) = 2\left(R - \sqrt{R^2 - z^2}\right) \approx z^2/R$. Finally, since the coupling coefficient decreases rapidly for after a certain length, we can use $\pm\infty$ for the limits of integral (A11). Therefore the coupling length is obtained as:

$$L_{\text{eff}} = \int_{-\infty}^{+\infty} \exp(-p\,z^2/R)\,dz = \sqrt{\frac{\pi R}{p}}. \quad \text{(A12)}$$

A2. References

1. K. Okamoto, "*Fundamentals of Optical Waveguides*," Academic press (2010).
2. B. E. Little, S. T. Chu, H. A. Haus, J. Foresi, J. P. Laine, "Microring resonator channel dropping filters", J. Lightwave Technol. **15**, 998 (1997).

3. J. Grgić, J. Raunkjær Ott, F. Wang, O. Sigmund, A.-P. Jauho, J. Mørk, and N. A. Mortensen, "Fundamental limitations to gain enhancement in periodic media and waveguides", Phys. Rev. Lett. **108**, 183903 (2012).

APPENDIX B: ASYMPTOTIC BEHAVIOR OF THE SUSY FIBER MODES

Here we show that for an arbitrary cylindrically symmetric potential $V(\eta)$ as described in Chapter 8 solution of the following equation:

$$\left(\frac{d^2}{d\eta^2}+\frac{1}{\eta}\frac{d}{d\eta}-\frac{l^2}{\eta^2}+V(\eta)\right)R=\mu R, \tag{B1}$$

for an azimuthal index l, around the origin ($\eta \to 0$) behaves like η^l. Note that $\eta = 0$ is a regular singular point of this differential equation i.e. one can avoid this singularity by multiplying both sides with η^2:

$$\left(\eta^2\frac{d^2}{d\eta^2}+\eta\frac{d}{d\eta}+(V(\eta)-\mu)\eta^2-l^2\right)R=0. \tag{B2}$$

Now let us consider the solution R as a multiplication of η^t and a power series around $\eta = 0$

$$R=\eta^t\sum_{n=0}^{\infty}a_n\eta^n, \tag{B3}$$

where t and all coefficients should be determined. Note that a_0 is assumed to be nonzero which guarantees that the first term in Equation (B3) is proportional to η^t. We also assume that the potential $V(\eta)$ is a well behaved function around the origin and can be described in a power series representation:

$$V=\sum_{n=0}^{\infty}b_n\eta^n. \tag{B4}$$

By plugging Equation (B3) and Equation (B4) into Equation (B2) and putting the coefficients all the equal ordered term equal to zero, for the zeroth order term we find:

$$[t(t-1)+t-l^2]a_0=0. \tag{B6}$$

Since a_0 is assumed to be nonzero we have:

$$t = \pm|l|. \tag{B7}$$

The negative solution is not acceptable since it leads to singularity at the origin. The positive solution on the hand can be a physical solution for a bound state. Therefore the lowest order term in Eq. (A3) is $\eta^{|l|}$ i.e. for $\eta \to 0$:

$$R(\eta) \sim \eta^{|l|}. \tag{B8}$$

Next, we find the asymptotic behavior of the radial function $R(\eta)$ for its other limit when $\eta \to \infty$. Assume the potential $V(\eta)$ is zero for large values of η. Therefore Eq. (A1) can be rewritten as:

$$\left(\eta^2 \frac{d^2}{d\eta^2} + \eta \frac{d}{d\eta} - (\mu\eta^2 + l^2)\right) R = 0. \tag{B9}$$

This latter equation is nothing more than the modified Bessel equation and the desired solution is the modified Bessel function of the second type. Therefore for $\eta \to \infty$:

$$R(\eta) \sim K_l(\sqrt{\mu}\eta). \tag{B10}$$

On the other by using the asymptotic behavior of the modified Bessel function for $\eta \to \infty$ we have:

$$R(\eta) \sim \frac{1}{\sqrt{\eta}} e^{-\sqrt{\mu}\eta} \tag{B11}$$

B1. References

1. G. B. Arfken and H. J. Weber, "*Mathematical Methods for Physicists*" Elsevier, Boston, (2005).